UNIVERSITY OF BIRMINGHAM

Evaluation of Microwave Microscopy for Dielectric Characterisation

Duncan James Barker

A thesis submitted to the University of Birmingham for the degree of Doctor of Philosophy

School of Electronic, Electrical and Computer Engineering
College of Engineering and Physical Sciences
The University of Birmingham
May 2010

Dedication

To The Most High God

Acknowledgments

I would like to thank my supervisor, Dr T. Jackson, for his consistent support and patience.

I would like to thank Prof. M. Lancaster and Dr F. Huang for offering their experience.

I would like to thank Dr P. Suherman for her help with measurements and support, D. Holdom for her help with sample preparation.

I would also like to thank EPSRC and the University of Birmingham for funding me and providing me with the necessary means to complete my PhD.

Most of all I would like to thank the one God from whom all things come, and to whom, all things return.

Synopsis

The optimisation and operation of a scanning near field microwave microscope (SNMM) is detailed for the first time. The SNMM comprises of a microwave resonant cavity. The sample to be measured is scanned via a near field beneath a sharp tip protruding from within the cavity. Changes in the dielectric properties of the sample cause shifts in the resonance frequency and quality factor of the cavity. The analysis covers design of the resonant cavity, the procedure of measurements of dielectric samples, the effect of the coupling coefficient, the tip to sample contact force and the sources of noise.

For the first time the effects of changes in coupling coefficient during measurements on the shifts in frequency and quality factor were derived from calculations and measurements of several standard samples. The lowest measurable changes in frequency and quality factor in the presence of thermal noise in the system were also calculated and presented for the first time as functions of the coupling coefficient.

A widely used analytical, image charge, model of the SNMM was analysed for the first time in terms of its ability to predict the response of the SNMM to both bulk and thin film dielectrics. For the first time it was shown that the uncertainty in fitting to the model reduces from 10% to 5% when the length of the tip protruding from within the cavity is reduced from 2mm to 1mm. A 5% uncertainty in fitting to the image charge model for the measurement of the relative permittivity of bulk samples is demonstrated.

SNMM measurements of the permittivity of barium strontium titanate thin films at 1.8 GHz and 4.4 GHz are compared with measurements made using co-planar waveguides (CPW) for the first time. The raw data suggest the SNMM has sufficient sensitivity to detect variations in permittivity across the film that the CPWs cannot detect. This result illustrates the advantages of a local probe, like the SNMM, over measurements of macroscopic properties. The average value of permittivity extracted from the data is consistent with that extracted from the co-planar waveguide measurements but the uncertainty bars associated with the extraction are large, of the order of 25 %. It was shown that the most significant contribution to this uncertainty comes from the analytical, image charge model. In conclusion, it was quantitatively demonstrated for the first

time that the widely used image charge model only produces an uncertainty of 5% when measuring bulk dielectrics, but this uncertainty leads to a 25% uncertainty when measuring dielectric thin films.

Contents

Chapter 1 – Introduction

1.1. – Introduction to Scanning Microscopy

In general, microscopy refers to a process where the local properties of samples are imaged or characterised. The word microscope originates from the Greek word *micrós-skopeín* meaning to see small things. The word "scanning" refers to the ability of the microscope system to make localised measurements of small areas sequentially so as to build a picture of a larger area.

The invention of the optical microscope is generally attributed to Zacharius Janssen in 1610 [1]. However, the earliest known work on lenses can be traced back to 700BC, Assyria, and also to ancient Egypt, Greece and Babylon [2].

Today microscopes have advanced not only to utilise many other wavelengths (other than optical), but also to utilise probing particles other than the photon. Most notably are the microscopes which use electrons, such as the scanning tunnelling microscope (STM) [3], transmission electron microscope (TEM) [4] and the scanning electron microscope (SEM) [5]. These have become widely used and essential tools for materials science, physics and chemistry. As well as particles, the forces between them have been utilised to image materials as in the case of the atomic force microscope (AFM) which has become a repeatable and popular measurement system.

Although the above mentioned types of microscopes have achieved extremely high spatial resolution, some able to resolve individual atoms, microscopes utilising photons will always be important to researchers who want to see the response of a material to electromagnetic waves of certain frequencies.

In the past, microscopes using electromagnetic waves inherently involved wave propagation processes to image objects. The spatial resolution of these microscopes was therefore limited by

diffraction [1]. If an object to be imaged can be considered as an array of point sources, then the diffraction limit is the minimum angular separation between two sources which can be distinguished for a given wavelength. The diffraction limit is given by $d = 1.22\lambda/D$, where λ is the wavelength of light used and D is the diameter of the lens.

This has been the major obstacle for these types of microscopes, which researchers have endeavoured to overcome. This limitation was later overcome through the use of the near-field.

1.2. – Development of Near Field Microscopy

Near Field Microscopy is the utilisation of near fields, or evanescent waves (quickly decaying in space), to image samples.

The near field is a class of component waves (or fields) emitted from any electromagnetically oscillating element which decay quickly with distance away from the source element. These are in contrast to component waves which decay slowly with distance from the element, termed far field components. For instance, the far field components of antenna emissions are utilised for communications and radar applications.

In the case of a short dipole antenna (where its length $l<<<\lambda$) the emitted electric and magnetic fields have contain several components which decay at different rates with distance. The near field components decay quickly with distance, r, away from the dipole as $1/r^3$ rather than the $1/r^2$ or $1/r$ characteristics of the far field components. It is the phase relationships of the electric and magnetic fields of propagating waves which allows them to propagate. However, the structure and phase of the electric and magnetic fields in near field waves are such that they represent zero time averaged energy flow (according to the Poynting Theorem [6]) meaning they do not propagate [7]. Therefore, energy is not radiated away by the near field but is instead shuttled back and forth once every half cycle and therefore is reactive [6].

For the short dipole antenna where $l<<<\lambda$, the wave amplitudes of the far field components are proportional to l/λ whereas the amplitude of the near field components are proportional to l only [6]. This means that when $l<<<\lambda$, the far field components will be of much smaller magnitude than the near field components especially when close to the dipole.

Hence, if the near field of a small electrically oscillating element can be used to probe materials, high spatial resolution (due to the small spatial extent of the near field) can be achieved efficiently (little radiated energy) and the diffraction limit overcome to image objects smaller than the operating wavelength.

The first person to suggest the use of the near field to increase the resolution of microscopes was Synge in 1928 [8]. Synge suggested that by illuminating an object with a point source a short distance away, the diffraction limit could be overcome.

However, the first work in demonstrating near field microscopy is attributed to Frait in 1959 [9] and Soohoo in 1962 [10]. Soohoo showed that by placing a sample over a 500μm diameter hole in the end plate of a resonator, a small region of the sample could be characterised individually. This meant that the variation in properties of the sample over its surface could be measured. Although Frait was first, the breaking of the diffraction limit is often attributed to Ash and Nicholls in 1972 [11] who used a similar setup to that of Soohoo.

Later, this type of aperture probe was widely used in Scanning Near-Field Optical Microscopy, (SNOM or NSOM) [12]. The aperture probe constituted a tapered metal tube (filled with quartz in some cases) pulled into a narrow end with a small hole to create the near field. The end of the waveguide was made narrow to achieve greater spatial resolution. However, this meant that this cylindrical waveguide had to be operated below its cut-off wavelength resulting is large signal attenuation [13]. Bethe had reported previously that a linear increase in the spatial resolution would result in a decrease in sensitivity to the tenth power [14].

This obstacle was addressed by the use of a coaxial transmission line as demonstrated by Fee *et al* in 1989 at both optical and microwave wavelengths [15]. The coaxial transmission line easily supports TEM waves, which have an infinite cut-off wavelength [16]. They suggested that a

cross-section at the end of a thin coaxial transmission line be used as a microwave microscope probe. However, the use of the near field at the end of a coaxial probe for local measurements of material properties had been reported over 20 years previously, by Bryant and Gunn in 1965 [17].

After the pioneering work mentioned above the subject of Near-Field Microscopy progressed in the optical [18], terahertz [19] and microwave and RF [20] frequency ranges.

1.3. – Introduction to Scanning Near-Field Microwave Microscopy

The development of dielectric materials is important for enhanced functionality in microwave and RF devices used in industries such as communications, media, defence and astronomy. Hence, advances in dielectric microwave characterization techniques are equally important. Planar and miniature devices may involve materials in the form of thin films (layers less than a micron thick deposited on a substrate). Conventionally, the microwave properties of thin films are assessed through the patterning and analysis of waveguides on the films [21]. In the case of thin films, the scanning near field microwave microscope (SNMM) requires little sample preparation whereas waveguide techniques require patterning processes to fabricate the waveguides on to sample surfaces. The waveguide technique requires careful operation to perform the measurements as compared to the SNMM which is mostly automatic. The waveguide methods yield an average value over the waveguides length, whereas the SNMM (due to its high spatial resolution) can deduce variances in thin film surface permittivity. This can reveal interesting information about the structure of the material and hence its suitability for microwave device applications. This would also enable the improvement of deposition techniques to make more uniform thin films for improved microwave properties.

The SNNM method also provides an alternative to waveguide techniques in the characterisation of bulk materials. For instance, surface resistance of the high temperature superconductor yttrium barium copper oxide (YBCO) has been characterised by forming a part of a waveguide

out of the material to be measured [22]. However, to make measurements using the SNMM, the sample needs only to have a surface.

1.3.1. – Review of Techniques in Scanning Near-Field Microwave Microscopy

Techniques in scanning near-field microwave microscopy have developed to include several different probe types and experimental setups. The probe of the microscope is the essential feature by which the near-field is coupled to a sample. In this section the types of probes are reviewed, concentrating on the most commonly used type.

The different probes which have been developed to utilise the near field can be categorised into several general groups which are shown in figure 1.1.

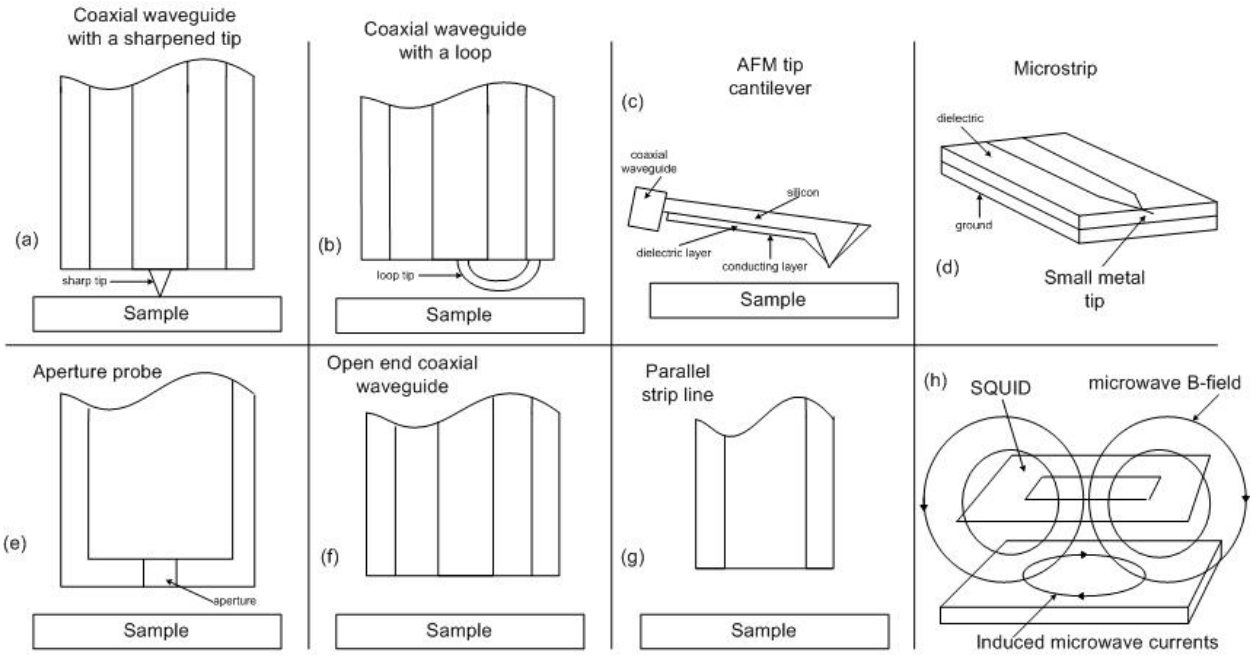

Figure 1.1. The main types of probes which have been used in scanning near field microwave microscopy: (a) Coaxial waveguide where the inner conductor ends in a sharpened tip [23], (b) Coaxial waveguide with a conducting loop for magnetic measurements [24], (c) Modified AFM tip [25], (d) Microstrip [26], (e) Waveguide with aperture [12], (f) Open-ended coaxial waveguide [27], (g) Parallel strip transmission line [28] (h) Superconducting quatum interference device [29].

For each of the examples shown in figure 1.1 the near field is utilised by virtue of the small size of the probe end (whether the probe ends in a tip or the open end of a waveguide) compared to the operating wavelength. The near field then couples with a sample placed in close proximity which causes a change in the impedance of the probe. The change in probe impedance is measured and used to calculate the sample permittivity or permeability via some analytical model, simulation or standard sample calibration routine. In most of the cases in figure 1.1 the probe is made to resonate, or is attached to a high quality factor resonating cavity.

The most commonly used probe type in the literature is the small sharp metal tip connected to the inner conductor of a coaxial resonator shown in figure 1.1a [23, 30, 31, 32]. The open end of the resonator results in an electric field maximum and magnetic field minimum at the tip, making it sensitive and insensitive to sample permittivity and permeability respectively. A near field is created around the tip due to its small size compared to the operational wavelength of the resonator. The electric near field around the tip couples to a dielectric sample when it is brought close to the tip. The real and imaginary parts of the permittivity of the sample alter the resonant frequency and quality factor of the resonator respectively. This setup can be used with one or two port measurements. Although this design is relatively easy to implement, the complicated field distribution around the tip-sample interface is difficult to model. However, work has been done towards an analytical model to describe the response of this type of probe to a dielectric sample using an iterative image charge approach [33], see chapters 3 and 5.

The spatial resolution of this type of tip is dependent of the electric field distribution surrounding the tip and is reported to be proportional to the diameter of the very end of the tip [33]. However, it also depends on the probe-sample distance and sample permittivity, see section 5.10. For instance Steinhauer *et al* showed by simulation that the electric field magnitude falls off exponentially with horizontal distance from the tip such the field strength has fallen by ≈75% after a distance of 2μm to 4μm for a tip diameter of 1.6μm and a homogenous sample of permittivity 2.1 [34]. However, for most samples, which are non-homogeneous, the sample permittivity outside this region can still effect the impedance of the probe significantly [28]. Gao *et al* reported a spatial resolution of 100nm with this type of probe [23]. Although the spatial resolution is proportional to the probe size, it cannot be improved indefinitely. This is due to the fact that, as the probe becomes smaller, an overall smaller electric field is produced to couple to

the sample creating a smaller signal to be measured, see section 5.10. In general, these points about spatial resolution and sensitivity apply to all the probes types shown in figure 1.1, although they may differ slightly depending on the geometry.

This type of probe has been used to measure the properties of a wide range of samples including permittivity of bulk dielectrics [35], tunability in ferroelectric thin films [34, 31], semiconducting devices [36], conductivity in metals [37], and superconductors [38] and also in the measurement of biological samples [39].

Other notable demonstrations of applications of scanning near field microwave microscopy using this type of probe have been the measurement of combinatorial synthesis material libraries [40], the imagining of periodically polarised ferroelectric domains in an yittrium-doped $LiNbO_3$ single crystal [41] and twins in lanthanum aluminate [42].

This type of probe has also been used at low temperatures despite the apparent difficulties in cooling the large apparatus [38], for example to measure the inhomogeneity in superconducting transition temperatures of YBCO samples.

Although this type of probe is limited to measurements of permittivity, it can easily be changed to make the microscope sensitive to permeability. By replacing the tip with a small conducting loop-tip grounded to the outer conductor, a magnetic field maximum and an electric field minimum can be created hence coupling a magnetic near field to the sample. This type of structure is shown in figure 1.1b and has been demonstrated by Lee *et al* [24]. In this work Lee *et al* demonstrated the use of the probe to measure the magnetic properties of paramagnetic and ferromagnetic samples with a 200μm spatial resolution. This type of probe works in the same way (except it is the magnetic analogue) as the probe used for dielectric measurements explained previously.

AFM tips have been modified (shown in figure 1.1c) to act as coaxial probes. This type of probe has been demonstrated in two different operational scenarios. In the first scenario the probe was used as a receiver to detect electric near fields created by the currents in an operating microwave circuit. This AFM and SNMM combination was demonstrated by Van der Weide [43]. In this

work Van der Weide modified the AFM cantilever tip (made from silicon) by coating it on the bottom with a dielectric, then a conducting layer, forming a parallel strip line waveguide. The modified tip was attached to a microwave measurement system via a coaxial wave guide. The device was demonstrated by measurements of a microwave integrated circuit operating at ≈1.3GHz where 30ps waveforms were recorded [43].

In the second scenario of modified AFM tips, microwaves are supplied to the probe so that near fields are emitted at the tip which couple to a sample which changes the impedance of the probe. [25].

Due to the small and complicated geometry of this type of probe, unknown parasitic inductances and capacitances may be a problem when trying to analytically model the tip [25]. However, in principle, any small probe attached to a waveguide or resonator can be used both as a receiver to measure localised sources of electric near fields and as a near field emitter probe.

The obvious advantage of this union between the AFM and the SNMM, is that one could perform simultaneous topographical and permittivity measurements. The spatial resolution of the microwave measurements of this type of probe would be proportional to its physical size but also depend on other factors mentioned previously for the other types of probes.

The micro-strip waveguide shown in figure 1.1d is another example of a waveguide which has been modified to emit a near field for localised dielectric sample measurements. This has been demonstrated by Tabib-Azar *et al* [26]. The near field micro-strip probe operates with one port measurements where the reflection coefficient is monitored as a sample is brought into the near field.

In this work Tabib-Azar *et al* demonstrated the micro-strip with both the sharp tip (for dielectric samples) and conducting loop tip (for magnetic samples) configurations. Also the spatial resolution of the probe was altered by changing probe parameters such as the permittivity of the micro-strip line substrate, the strength of the feed-line to resonator coupling and probe tip geometry. This flexibility in spatial resolution is an advantage of this type of probe. However,

high quality factors (which are important for measurements of loss) are harder to achieve with waveguides rather than cavity resonators.

Figure 1.1e shows an aperture probe similar to the one used in the early work by Soohoo [10].

A simple version of the open ended coaxial /resonator is shown in figure 1.1f. This type of probe has been demonstrated by Cho *et al* in 1996 [27] and then by Steinhauer *et al* in 1997 [44]. These work in the same way as the open ended waveguide with a sharp tip (shown in figure 1.1a). The spatial resolution of this type of probe would be approximately the size of the probe itself, but also depend on other parameters mentioned previously.

Steinhauer *et al* demonstrated the use of this type of probe by measuring the change in probe impedance when approaching aluminium and glass samples followed by fitting the results to simple models of series capacitors and resistances. They reported a sensitivity of 2 parts in 10^6 which is easily achievable with resonator/network analyser measurement systems. This type of probe has found application in the measurement of polar liquids to investigate the effect of microwaves on living organisms (which are mostly liquid) [45]. The flat, open ended waveguide in contact with the flat surface of a liquid is easier to model analytically than the sharp tip in contact with a flat surface.

Figure 1.1g shows a parallel strip line type of near field probe which has been demonstrated by Talanov *et al* [28]. The parallel strip line type probe works in the same way as the other open ended waveguides discussed previously. The probe was manufactured by depositing Al onto two opposite sides of a quartz bar. The end was then trimmed down to 1-10μm using a focused ion beam. Although this type of probe may be more difficult to fabricate than the sharp tip on a coaxial resonator it is claimed that this probe has better spatial resolution despite being physically bigger [28]. This is because the electric field at the end of the probe decays quicker (due to its geometry) with horizontal distance away from the probe than that of the sharp tip at the end of a coaxial waveguide, see section 5.11. This means that most of the electric field energy is concentrated within a volume defined by the diameter of the probe end making it less sensitive to sample permittivity outside this region.

.

The use of a superconducting quantum interference device (SQUID) as shown in figure 1.1h was been reported by Black *et al* [29]. The circulating currents in the SQUID create a magnetic field which induces currents in the nearby sample. The induced currents in the sample induce their own magnetic fields which alter the magnetic field, and hence current, of the SQUID, which can be monitored. Black *et al* used this type of probe for low temperature (77K) measurements of the conductivity of copper and YBCO.

Although the spatial resolution of this type of device (30um) is larger than that of the coaxial resonator with sharp tip design, it has the advantage of being continuously tuneable up to 200GHz.

The idea of using a coaxial probe has been extended to that of using a quadraxial probe [46]. This waveguide consists of four concentric conductors each separated by a layer of Teflon. The authors found through simulation that the electric field decayed more quickly with horizontal distance than in the case of the coaxial probe when the 1^{st} and 3^{rd} conductors of the quadraxial probe were driven with the same magnitude signal but 180^0 out of phase. This is due to the destructive interference of the electric field wave caused by the 180^0 phase shifted signal.

In conclusion, the many types of probes outlined above offer different advantages such as greater spatial resolution, continuous tunability and permeability as well as permittivity measurements. Some applications of the probes have been detailed concentrating on the sharp tip with coaxial resonator probe.

1.3.2. – Probe to Sample Distance Control in Scanning Near Field Microwave Microscopy

The impedance of the probe will depend on factors such as probe-sample geometry, probe-sample distance and any water layer on the sample. These factors must be kept constant to attribute changes in probe impedance to sample properties.

As long as the probe is not damaged through contact to the sample its geometry should remain constant. Water layers on samples can be influenced through atmospheric control. However, the thickness of a water layer on a surface may depend on the material properties of the surface. The various ways to control the tip-sample distance are reviewed here.

The maintenance of a constant probe-sample distance would increase measurement accuracy and allow topographical surface data to be recorded. To maintain constant probe-sample distance, the distance must be simultaneously monitored and controlled through a feedback loop. Monitoring the probe-sample distance can be achieved via several means such as shear force, capacitance, photon tunnelling and electron tunnelling. Each one is explained and discussed here in turn.

In the shear force probe to sample distance control method the probe is made to mechanically oscillate at frequency of resonance. As the oscillating probe then approaches the sample surface it will feel time varying Van der Waals (permanent or induced dipole attraction or repulsion forces) and capillary forces (the forces due a water layer joining two surfaces in close proximity) [47] which dampen the amplitude of oscillation. The amplitude of oscillation of the probe is monitored via a feedback circuit (usually a lock in amplifier or phase lock loop) which monitors and controls the probe to sample distance so as to keep it constant. Shear force method is the most common method of probe-sample distance control for these types of microscopes and has been implemented in several different ways. The shear force method is used most commonly with the sharp tip at the end of a coaxial waveguide type probe shown in figure 1.1a.

Talanov *et al* demonstrated the shear force method in terms of the sharp tip and coaxial resonator. This was done by setting the entire resonator into oscillation (by attaching a mechanical oscillator to it) to produce the necessary probe oscillations [28]. To monitor the amplitude of mechanical oscillations of the probe as it approached the sample surface Talanov *et al* scattered a laser beam off the probe onto a photo detector. The advantage of this system is that there is no interference of the laser beam with the near field microwaves created by the probe.

Shear force has also been implemented on the use of SNOM, as reported by Betzig *et al* [48].

Another method used to achieve shear force probe-sample distance control with a larger resonator is that of attaching a quartz crystal tuning fork to the tip of the probe shown in figure 1.1a. A lock in amplifier is used to supply a signal to the fork and monitor the resulting damping of the amplitude of oscillation on approach to the sample. This implementation was shown by M. S. Kim *et al* [49].

Although an AFM utilises the same forces as those used by the shear force method, it monitors the deflection of a cantilever due to the forces rather than the damping of mechanical oscillations. It is included here due to the successful union of the AFM and the SNMM mentioned above.

The response of the probe and resonator itself has been used to control probe to sample distance, referred to as a capacitance method. It can be achieved if a particular response of the probe proportional to probe-sample distance can be made independent from that which is to be measured.

It has been reported by Duewer *et al* that, the change in resonant frequency of the resonator as it is brought close to a conducting sample is the same for all conducting samples above a certain conductivity and can therefore be used to determine the probe-sample distance for that set of samples [50]. The quality factor is then used to measure the sheet resistance of the sample [50]. However, the definition of high conductivity in this case was not quantified until the later work of Kim *et al* who showed that for any sample with sheet resistance less than approximately 20KΩ/□ (conductivity greater than 50μS) the same resonant frequency shift vs probe-sample distance was recorded [51]. This system is limited to conducting samples and is therefore not as versatile as the shear force method of probe-sample distance control. It also requires all points of the sample lie within the stated range of conductivity.

Electron tunnelling between conducting samples and charged tips (as in the case of the STM) has been implemented to control probe to sample distance in scanning near field microwave microscopy [13]. This requires the application of a bias voltage to the probe and is limited to conducting samples. As long as the application of a bias voltage and tunnelling current to the near field tip does not interfere with the functioning of the probe this system appears feasible.

A process referred to as photon tunnelling has been used to regulate probe to sample distance in the field of SNOM [52]. In this method, the underside of a dielectric sample is illuminated with a 7mW helium-neon laser beam incident at an angle greater than the critical angle such that total internal reflection takes place. This creates a near field on the opposite side of the sample at the sample (higher permittivity) air (lower permittivity) boundary. The changes in the sample topography change the near field which is monitored by the probe. However, it may be difficult to distinguish between changes in the near field due topography and changes due to photon absorption in the dielectric sample.

Various types of probe-sample distance control methods have been discussed. The shear force method remains the most widely used for the sharp tip attached to a coaxial resonator type probe and is the most flexible.

1.4. – Experimental Apparatus

This section describes the experimental setup for the research work reported in this thesis. Only the scanning near field microwave microscope detailed in this section is considered throughout the rest of this thesis and is therefore forthwith simply referred to as the microscope.

Figure 1.2 shows the experimental setup, which is based on an open ended ¼λ coaxial resonator made from copper. The inner conductor ends in a sharp tip. The tip protrudes 1mm to 2mm through a hole in the bottom endplate without making electrical contact to the endplate. Energy is coupled into the coaxial resonator via two conducting loops formed from the inner conductors of RG405 coaxial cables. These enable connection of the cavity to the programmable network analyser (PNA) for two port measurements.

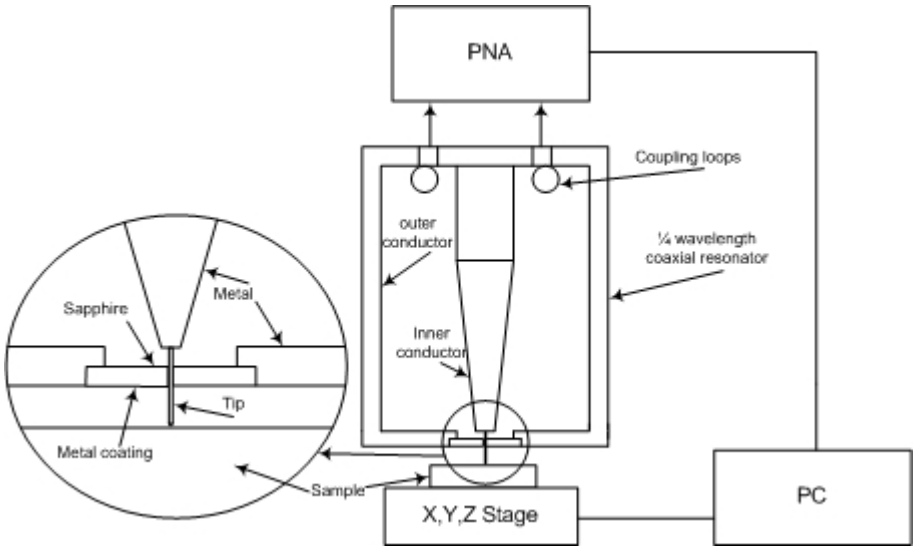

Figure 1.2. Diagram of the ¼λ coaxial open ended resonator and arrangement for the SNMM.

In this setup, changes in resonant frequency and quality factor of the cavity are monitored by the PNA as the sample is brought into contact with the tip. This configuration was patented by, and attributed to, Xiang *et al* [53].

The position of the sample is controlled via a *x,y,z* stage as shown in figure 1.2. The *x,y,z* stage contains mechanical *x,y* and piezoelectric *x,y,z* stages both controlled by a PC. The mechanical stage provides movements in the *x,y* position of the sample from 50mm to 1μm. However for movements of the order of 10's of microns and less, greater accuracy and repeatability can be obtained with the piezoelectric stage. The piezoelectric stage can be used for moving along the *x,y* and *z* axes in the range 100μm to 10nm. The PC controls the sample position during a scan of the sample surface with the appropriate stages. The resonator itself is mounted above the sample stages on a manual mechanical stage providing vertical (*z*) coarse movements of up to 50mm.

Instructions from the PC cause the stages to move the sample to a set position. Then the PNA is instructed to sweep over a prescribed frequency range, locating the resonant frequency and computing the quality factor and *S*-parameters. These values are recorded on the PC. The PC then controls movement of the sample to the next position in the scan and the process repeats. To scan a sample of $1cm^2$ at a sensible spatial resolution takes approximately 24 hours due to the time taken to acquire accurate data at each point.

The tips were made by the present author from tungsten and were soldered into the inner conductor. To form the sharp end of the tip, it was chemically etched (this process is detailed in [54]) using potassium hydroxide to produce a sharp point of approximately 10μm - 30μm diameter. The opposite end was electroplated coated with nickel followed by gold to enable soldering. As the spatial resolution is approximately the same size as the end of the tips, a spatial resolution of 10μm - 30μm is expected.

To avoid an electrical short between the tip and the end wall of the cavity, a 1cm diameter sapphire disc is bonded with silver dag to an opening in the bottom end wall. The tip passes through a 0.5mm diameter hole in the middle of this disc. The tight fit of the tip in the hole prevents flexing of the tip during scanning. In order to reduce radiative losses the bonding face of the sapphire disc is coated with gold.

In general this design offers the resolution of a small near field (due to the small tip) combined with the sensitivity of a high quality factor resonator.

The work of this thesis has quantitatively analysed the widely used image charge model [33] for the measurement of bulk and thin film samples for the first time. This work also quantifies the effect of tip-sample force in terms of this model for the first time. Sources of uncertainty in the model have been identified so that improvements can be made in future work. Also, the work of this thesis has analytically derived the sensitivity of the SNMM and how it can be altered.

1.5. – Structure of Thesis

A review of the probing techniques and methods has been given in chapter 1 along with a description of the experimental apparatus. The behaviour of the electromagnetic fields within the apparatus is derived in chapter 2. Chapter 3 introduces dielectric materials in the context of the SNMM and the work presented in this thesis. Chapter 4 deals with operation and optimisation of the current apparatus. A widely used model of the SNMM which is available in the literature [33] is reviewed critically in Chapter 5 and a quantitative assessment of its application to

investigation of thin films is presented. Chapter 6 summarises the conclusions of the thesis and discusses further work.

Chapter 1 Bibliography

[1] E. Hecht, *Optics*, Addison-Wesley, 4th Edition, New York, 2001.

[2] F. L. Pedrotti, *Introduction to Optics*, . John Wiley and Sons, 3rd Edition, 1932.

[3] G. Binnig, H. Rohrer. "Scanning tunnelling microscopy", *IBM Journal of Research and Development*, vol. 30, no. 4, pp. 355, 1986.

[4] R. F Egerton, *Physical Principles of Electron Microscopy; An Introduction to TEM, SEM, and AEM*, Springer, New York, 2006.

[5] M. Knoll. "Aufladepotentiel und sekundaremisson elektronenbestrahlter korper", *Zeitschrift fur technische physic*. vol. 108, no. 9, 1935.

[6] J. D. Kraus. *Electromagnetics*, McGraw-Hill, 2nd Edition, New-York, 1973.

[7] S. Ramo, J. R. Whinery, T. V. Duzer. *Fields and Waves in Communication Electronics*. John Wiley and Sons. 1st Edition. New-York, 1965.

[8] E. H. Synge, "A suggested method for extending microscopic resolution into the ultra-microscopic region", *Phil. Mag.*, vol. 6, pp. 356 1928.

[9] Z. Frait, *Czech. Journ. Phys.*, vol. 9**,** pp. 403, 1959.

[10] R. F. Soohoo. "A microwave magnetic microscope", *J. Appl. Phys.*, vol. 33, pp. 1276, 1962.

[11] E. A. Ash and G. Nicholls. "Super-resolution aperture scanning microscope", *Nature.* vol. 237, pp. 510, 1972.

[12] U. Dürig, D. W. Pohl and F. Rohner. "Near-field optical-scanning microscopy", *J. Appl. Phys.*, vol 59, pp. 3318, 1986.

[13] B. Knoll, F. Keilmann, A. Kramer, and R. Guckenberger. "Contrast of microwave near-field microscopy", *Appl. Phys. Lett.*, vol. 70, pp. 2667, 1997.

[14] H. A. Bethe, "Theory of Diffraction by Small Holes", *Phys. Rev.*, vol. 66, pp. 163, 1944.

[15] M. Fee, T. Chu and T. W. Hans. "Scanning electomagnetic transmission line microscope with sub-wavelength resolution, *Optics. Comms.* vol. 69, pp. 219, 1989.

[16] N. Marcuvitz. *Waveguide Handbook*. McGraw-Hill, 2nd Edition, New-York, 1951.

[17] C. A. Bryant, J. B. Gunn. “Noncontact technique for the local measurement of semiconductor resistivity,” *Rev. Sci. Instrm.*, vol. 36, pp. 1614, 1965.

[18] E. Betzig and J. K. Trautman, “Near-field optics: microscopy, spectroscopy, and surface modification beyond the diffraction limit”, *Science*, vol. 257, pp. 189, 1992.

[19] G. C. Cho, H.-T. Chen, S. Kraatz, N. Karpowicz and R. Kersting. “Apertureless terahertz near-field microscopy”, *Semicond. Sci. Technol.* vol. 20, pp. 286, 2005.

[20] T. Wei, X. –D. Xiang, W. G. Wallace-Freedman and P. G. Schultz. “Scanning tip microwave near-field microscope”, *Appl. Phys. Lett.*, vol. 68. pp. 3506, 1996.

[21] S. S. Gevorgian, “Basic characteristics of two layered substrate coplanar waveguides”, *Electron. Lett.*, vol 30, pp. 1236, 1994.

[22] P. Woodall, M. J. Lancaster, T. S. M. Maclean, C. E. Gough and N. McN. Alford. Measurments of the surface resistance of $YBa_2Cu_3O_{7-\delta}$ by the use of a coaxial resonator. *IEEE Trans. on Magnetics*, vol 27, pp. 1264, 1991.

[23] C. Gao, T. Wei, F. Duewer, Y. Lu and X.-D. Xiang. “High spatial resolution quantitative microwave impedance microscopy by scanning near-field microscope. *Appl. Phys. Lett.*, vol 71, pp. 1872, 1997.

[24] S.-C. Lee, C. P. Vlahacos, B. J. Feenstra, A. Schwartz, D. E. Steinhauer, F. C. Wellstood and S. Analage. “Magnetic permeability imaging of metals with a scanning near-field microwave microscope”, *Appl. Phys. Lett.*, vol. 77, pp. 4404, 2000.

[25] M. Tabib-Azar and Y. Wang. “Design and fabrication of scanning near-field microwave probes compatible with atomic force microscopy to image embedded nanostructures”, *IEEE Trans. Microwave Theory & Tech.*, vol. 52, pp. 971, 2004.

[26] M. Tabib-Azar, P. S. Pathak, G. Ponchak and S. LeClair. “Nondestructive super-resolution imaging of defects and non-uniformities in metals, semiconductors, dielectrics, composites and plants using evanescent microwaves”, *Rev. Sci. Instrm*. vol. 70, pp. 2783, 1999.

[27] Y. Cho, A. Kirihara and T. Saeki. “Scanning nonlinear dielectric microscope”, *Rev. Sci. Instrum.*, vol. 67, pp. 2297, 1996.

[28] V. V. Talanov, A. Scherz, R. L. Moreland and A. R. Schwartz. “A near field scanned microwave probe for spatially localised electrical metrology”, *Appl. Phys. Lett.*, vol. 88, pp. 134106, 2006.

[29] R. C. Black, F. C. Wellstood, E. Dantsker, A. H. Miklich, D. T. Nemeth, D. Koelle, F. Ludwig and J. Clarke. "Microwave microscopy using a superconducting quantum interference device", *Appl. Phys. Lett.*, vol. 66, pp. 99, 1995.

[30] D. E. Steinhauer, C. P. Vlahacos, F. C. Wellstood, S. M. Anlage, C. Canedy, R. Ramesh, A. Stanishevsky and J. Melngailis. "Imaging of microwave permittivity, tunability, and damage recovery in $BaSrTiO_3$ thin films", *Appl. Phys. Letts.*, vol. 75, pp. 3180, 1999.

[31] S. Hyun, J. H. Lee, S. S. Kim, K. Char, S. J. Park, J. Sok and E. H. Lee. "Anisotropic tuning behaviour in epitaxial $Ba_{0.5}Sr_{0.5}TiO_3$ thin films", *Appl. Phys. Letts.*, vol. 77, pp. 3084, 2000.

[32] R. A. Kleismit, M. K. Kazimierczuk and G. Kozlowski. "Sensitivity and resolution of evanescent microwave microscope", *IEEE Trans. Microwave Theory & Tech.*, vol. 54, pp. 639, 2006.

[33] C. Gao and X.-D. Xiang. "Quantitative microwave near field microscopy of dielectric properties", *Rev. Sci. Instrum.* vol. 69, pp. 3846, 1998.

[34] D. E. Steinhauer, C. P. Vlahacos, F. C. Wellstood, S. M. Anlage, C. Canedy, R. Ramesh, A. Stanishevsky and J. Melngailis. "Quantitative imaging of dielectric permittivity and tunability with a near-field scanning microwave microscope", *Rev. Sci. Instrum.* vol. 71, pp. 2751, 2000.

[35] M. D. Janezic, J. A. Jargon and J. B-Jarvis. "Relative permittivity measurements using the higher order resonant modes of a near field microwave probe," National Institute of Standards and Technology, USA.

[36] R. A. Kleismit, and M. K. Kazimierczuk. "Evanescent microwave microscopy of thermally-damaged charge coupled devices", *IEEE Proc. Elec. Insl. Conf. and Elec. Manu. & Coil Winding*, pp. 485, 2003.

[37] A. Imtiaz, T. Baldwin, H. T. Nembach, T. M. Wallis, and P. Kabos, "Near-field microwave microscope measurements to characterize bulk material properties", *Appl. Phys Lett.*, vol. 90, pp. 243105, 2007.

[38] I. Takeuchi, T. Wei, F. Duewer, Y.K. Yoo and X.-D. Xaing. "Low temperature scanning-tip microwave near field microscopy of $YBa_2Cu_3O_{7-x}$ films", *Appl. Phys. Lett.*, vol. 71, pp. 2026, 1997.

[39] J. Park, S, Hyun, A. Kim, and K. Char, "Observation of biological samples using a scanning microwave microscope", *Ultramicroscopy*, vol. 102, pp. 101, 2005.

[40] C. Gao, B. Hu, I. Takeuchi, and K.-S. Chang. "Quantitative scanning evanecsent microwave microscopy and its applications in the characterization of functional materials libraries", *Meas. Sci. Technol.*, vol. 16. pp. 248, 2004.

[41] Y. Lu, T. Wei, F. Duewer, Y. Lu, N.-B. Ming, P. G. Schultz and X.-D. Xiang, "Nondestructive imaging of dielectric-constant profiles and ferroelectric domains with a scanning-tip microwave near-field microscope", *Sci.*, vol. 276, pp. 2004, 1997.

[42] Q. Zhang and P. J. McGinn. "Imaging of oxide dielectrics by near-field microwave microscopy", *Journ. Euro. Cer. Soc.*, vol. 25, pp. 407, 2005.

[43] D. W. Van der Weide. "Localised picosecond resolution with near-field microwave/scanning-force microscope", *Appl. Phys. Lett.* vol. 70, pp. 677, 1997.

[44] D. E. Steinhauer, C. P. Vlahacos, S. K. Dutta, F. C. Wellstood and S. M. Analage. "Surface resistance imaging with a scanning near field microwave microscope", *Appl. Phys. Lett.*, vol. 71, pp. 1736, 1997.

[45] A. P. Gregory and R. N. Clarke. "A review of RF and Microwave Techniques for Dielectric Measurements on Polar Liquids", *IEEE. Trans. Die. & Elec. Insuln.* vol. 13, pp. 727, 2006.

[46] A. Karbassi, C. a. Paulson, A. B. Kozyrev, M. Banerjee, Y. Wang and D. W. van der Weide. "Quadraxial probe for high resolution near-field scanning RF/microwave microscopy", *Appl. Phys. Letts.* vol. 89, pp. 153113, 2006.

[47] R. Toledo-Crow, P. C. Yang, Y. Chen, and M. Vaez-Iravani, "Near-filed differential scanning optical microscope with atomic force regulation", *Appl. Phys. Lett.* vol. 60, pp. 2957, 1992.

[48] A. Betzig, P.L. Finn, and J. S. Weiner, "Combined shear force and near-field scanning optical microscopy", *Appl. Phys. Lett.* vol. 60, pp. 2484, 1992.

[49] M. S. Kim, S. Kim, J. Kim, K. Lee, B. Freidman, J.-T. Kim, and J. Lee. "Tip-sample distance control for near-field scanning microwave microscopes" *Rev. Sci. Instrum.* vol. 74, pp. 3675, 2003.

[50] F. Duewer, C. Gao, I. Takeuchi, and X.-D. Xiang, "Tip–sample distance feedback control in a scanning evanescent microwave microscope", *Appl. Phys. Lett.*, vol. 74, pp. 2696, 1999.

[51] A. Kim, J. Kim, S. Hyun, S. S. Kim, T. Kim, and K. Char. "Surface following scanning in a scanning microwave microscope", *Rev. Sci. Instrum.*, vol. 74, pp. 3164, 2003.

[52] R. C. Reddick, R. J. Warmack and T. L. Ferrell. "New form of scanning optical microscope", *Phys. Rev. B*, vol. 39, pp. 767, 1988.

[53] X.-D. Xiang, C. Gao. “Scanning evanescent electro-magnetic microscope” US Patent No. 6,173,604, B1. (2001).

[54] J. F. Wolf, P. E. Hillner, R. Bilewicz, P. Kolsch, and J. P. Rabe. “Novel scanning near-field optical microscope (SNOM)/scanning confocal optical microscope based on normal force distance regulation and bent etched fiber tips”, *Rev. Sci. Instrum.* vol. 70, pp. 2751, 1999.

Chapter 2 – Microwave Resonant Cavities

2.1. – Introduction to Microwave Resonant Cavities

Microwave resonant cavities are enclosed spaces designed to contain an oscillating electromagnetic field. This is achieved by manufacturing the dimensions of the cavity equal to whole numbers or fractions of wavelengths of the oscillations one wishes to contain. Therefore the cavity will only resonate when oscillations of the correct frequency are supplied to it.

As in the case of a LRC circuit, at resonance the maximum amount of energy (which is contained within the electric and magnetic fields) is stored because the inductive and capacitive impedances are equal. Therefore at resonance, the output voltage and current are in phase resulting in the largest output.

The combination of maximum energy stored to low loss of resonators makes them extremely sensitive to any perturbations of the fields within them. Any sample inserted within the cavity will perturb the fields according to its permeability, permittivity, shape and volume. Resonators therefore make excellent measurement devices for the characterisation of materials. Due to the high dependence of output power on input frequency resonators also find use as filters [1].

Resonators can also be made out of dielectric materials. Dielectric resonators can come as both cavities and solid pieces. Although the resonating wave is mostly contained within the dielectric, dielectric resonators are usually used within closed metal cavities to reduce any energy lost in the form of radiation. Dielectric resonators have the advantage of low conductivity making them have larger quality factors in general.

In general, several oscillating modes, occurring at different frequencies, are supported in any resonator, depending on the geometry. The modes are categorized as either transverse electric (TE), transverse magnetic (TM) or transverse electromagnetic (TEM) modes [2]. A TE mode is

one in which the electric field is perpendicular to the direction of travel. A TM mode is one in which the magnetic field is perpendicular to the direction of travel. A TEM mode is one where both the electric and magnetic fields are perpendicular to the direction of travel.

In this section the basic definitions of quality factor are given and then extended to the open ended coaxial cavity case. The static fields inside an open ended coaxial structure are derived using Gauss' and Ampere's laws in order to find the capacitance and inductance of the structure for a TEM mode. Finally the modes of a resonating coaxial structure are calculated.

2.2. – Quality Factors of Resonant Cavities

The quality factor is a measure of the efficiency of an oscillating system. The quality factor, Q, is defined as

$$Q = \omega \cdot \frac{Energy\ stored}{Energy\ lost\ \ per\ cycle} = \omega \cdot \frac{U}{P}. \tag{2.1}$$

The quality factor of the resonator itself is often referred to as the unloaded quality factor, Q_0.

Usually, energy is fed into resonators via a wire element inside the cavity. However, the wire element which feeds energy into the cavity can also take energy out. Energy coupled out of the cavity in this way constitutes a loss of energy. A quality factor can then be attributed to this, called the external quality factor, Q_e. The quality factor of the entire system is a sum of the reciprocals of these two quantities and is called the loaded quality factor, Q_L. The loaded quality factor is the quality factor which is measured directly. It is defined as

$$\frac{1}{Q_L} = \frac{1}{Q_0} + \frac{1}{Q_e}. \tag{2.2}$$

Equation (2.2) shows that when $Q_e >>> Q_0$, $Q_L \approx Q_0$. This is an advantageous situation in which to take measurements, and can be affected by the strength of the coupling into the cavity, see section 2.6 and 4.4.

In a cavity resonator, several mechanisms of loss are present. Mechanisms of loss depend on the construction of the cavity, for instance, a dielectric resonator will have a loss associated with the dielectric due to its finite loss tangent. An open-ended resonator will have a loss associated with radiation leakage from the open end. Any conductive components of a resonator such as the cavity walls will have a loss associated with the finite conductivity of the walls. A separate quality factor for each loss mechanism can be defined. The sum of the reciprocals of these quantities makes up the unloaded quality factor,

$$\frac{1}{Q_0} = \frac{1}{Q_R} + \frac{1}{Q_C} + \frac{1}{Q_D}, \tag{2.3}$$

where Q_R, Q_C and Q_D are the radiation, conduction and dielectric quality factors respectively.

The conduction quality factor is given by

$$Q_C = \omega\mu \frac{\int_{cav} |H|^2 \, dV}{\int_{cond} \sigma |E|^2 \, dV} = \frac{\omega\mu}{R_s} \frac{\int_{cav} |H|^2 \, dV}{\int_{cond} |H|^2 \, dS}, \tag{2.4}$$

where the upper integral is over the volume of the entire cavity. The lower integral is simplified from being over the volume of the conductor to being over its surface only. The magnetic and electric field strengths are represented by H and E respectively, ω is the angular frequency of the oscillations and σ is the conductivity of the cavity walls. The surface resistance, R_S, is given by $R_S = \sqrt{\omega\mu / 2\sigma}$ where μ is the permeability of the material filling the volume of the cavity.

The radiation quality factor is given by

$$Q_R = \frac{2\omega}{c} \cdot \frac{\mu \int_{cav} |H|^2 \, dV}{\int_{sphere} |H|^2 \, dS}, \tag{2.5}$$

where c is the speed of light in a vacuum and the lower integral is taken over the surface (far away from the cavity) of a sphere enclosing the element which is radiating.

The dielectric quality factor is given by

$$Q_D = \frac{1}{\tan\delta} \cdot \frac{\mu \int_{cav} |H|^2 \, dV}{\varepsilon \int_{die} |E|^2 \, dV}, \tag{2.6}$$

where $tan\delta$ is the loss tangent of the dielectric within the cavity.

To calculate each quality factor defined above for the cavity shown in figure 1.2 the electric and magnetic fields in the coaxial structure must first be found. The electric and magnetic fields depend on the geometry and mode of the resonator and are approximated for the fundamental TEM mode of a coaxial structure in the following section.

2.3. – Fields of TEM Modes in Coaxial Structures

To find the static electric and magnetic fields of a coaxial structure Gauss' and Ampere's laws are used. The static fields are then extended to the time and space dependent case of the fundamental TEM mode. Firstly, the geometry of a coaxial structure is defined.

Figure 2.1 shows a diagram of a section of an infinitely long (fringing fields can be ignored) coaxial line. In figure 2.1 the inner and outer conductor radii are termed *a* and *b* respectively, and the Gaussian surface is represented as a dashed line. The Gaussian surface is such that the electric field lines exiting the surface are perpendicular to it.

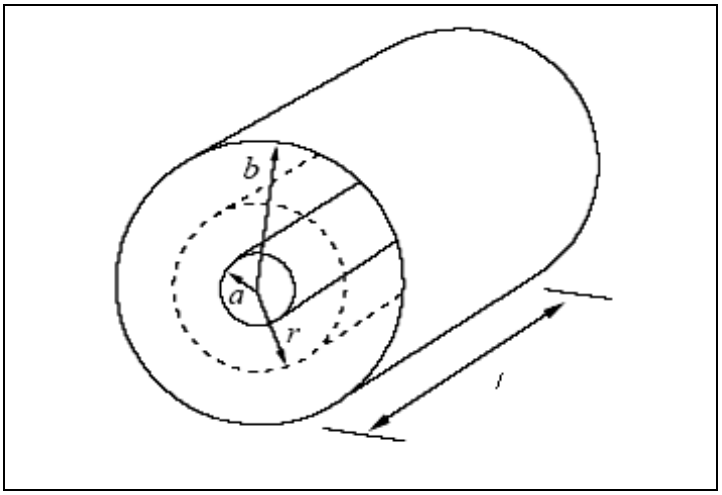

Figure 2.1 A section of an infinitely long coaxial transmission line showing inner and outer conductor radii and a Gaussian surface as a dashed line.

Gauss' law is

$$\int \underline{E} \cdot d\underline{S} = \frac{q}{\varepsilon_0}, \tag{2.7}$$

where q is the charge enclosed by the surface S. When applying equation (2.7) to the coaxial structure it is useful to take advantage of the charge symmetry along the length by defining a charge per unit length as $\lambda = q/l$. Solving equation (2.7) for the coaxial structure results in

$$\underline{E} = \frac{\lambda}{2\pi\varepsilon_0 r} \cdot \underline{\hat{r}}, \tag{2.8}$$

where $\underline{\hat{r}}$ is a unit vector in the r direction according to cylindrical polar coordinates. The infinitely long line is an approximation of the fields inside a closed end cavity. For instance, when the end plates of the cavity are considered there is no longer charge symmetry along the length. For a consideration of these fields see reference [3]. Also, the resonator shown in figure 1.2 has a tapered inner conductor which further distorts the fields from the case considered here.

Integration of the electric field between the inner and outer conductors gives the potential difference between the two as

$$V = \frac{\lambda}{2\pi\varepsilon_0} \cdot \ln(b/a)\,. \tag{2.9}$$

In order to find the static magnetic field inside the coaxial structure shown in figure 2.1 Ampere's law can be used. Ampere's law is

$$\int \underline{H} \cdot d\underline{l} = \underline{I}\,, \tag{2.10}$$

where I is the current passing through a circle of radius r and circumference $2\pi r$. Ampere's law applied to a coaxial structure results in

$$\underline{H} = \frac{I}{2\pi r} \cdot \underline{\hat{\theta}}\,, \tag{2.11}$$

where $\underline{\hat{\theta}}$ is a unit vector in the direction θ according to cylindrical polar coordinates. The static fields derived from Gauss' and Ampere's law only give us the magnitude of the electric and magnetic parts of a TEM standing wave in a resonator. In reality, the fields inside a resonator are space and time dependent.

As in the case of a resonant LRC circuit, the voltage and current, and hence electric and magnetic fields in a TEM mode are $\pi/2$ out of phase in time.

In order to find the correct spatial dependences, the boundary conditions of the structure must be considered. The coaxial structure (figure 1.2) considered in this thesis is open at one end and closed at the other end, (open ended). As an approximation for the purposes of the calculations in this chapter, the structure shown in figure 2.2 is considered. The radii of the inner and outer conductor are fixed at a = 4.6mm and b = 15.2mm respectively. The length, l is 40.1mm.

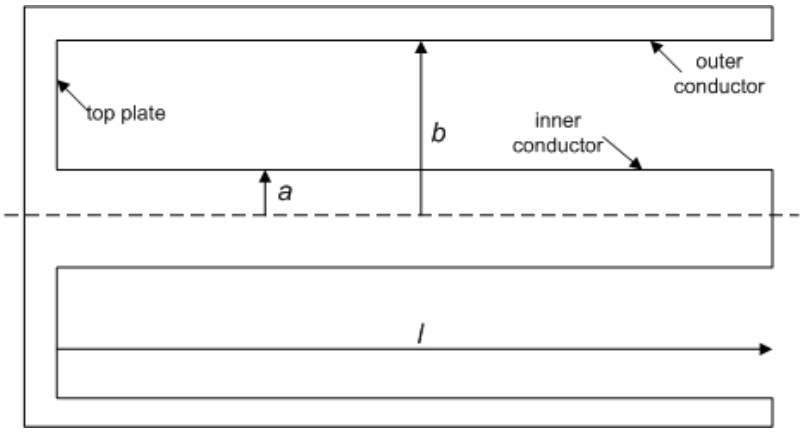

Figure 2.2 A open ended coaxial resonator showing inner and outer conductor radii and length, *l*.

At the open end there will be a voltage (and hence electric field) maximum. At the closed end the electric field is a minimum. The opposite is true for the magnetic field. Therefore the open ended resonator forces the fundamental TEM mode to be *1/4λ*. Therefore the electric and magnetic fields are *π/2* out of phase in space.

Therefore, using equations (2.8), (2.9) and (2.11), and the discussion above, the time and space dependent electric and magnetic fields inside the open ended coaxial structure will have the form

$$\underline{E} = \frac{V}{r}\frac{\hat{\underline{r}}}{\ln(b/a)}\sin(kz)\sin(\omega t) \tag{2.11}$$

and

$$\underline{H} = \frac{I}{2\pi r}\hat{\underline{\theta}}\cos(kz)\cos(\omega t)\,. \tag{2.12}$$

In Equations (2.11) and (2.12), k is the wavenumber, ω is the angular frequency, z is measured along the length of the coaxial resonator, and is zero at the closed end. l is the total length of the resonator.

The method of using the static field equations to derive wave equations of resonant modes is

only valid for TEM modes, where the magnitude of the waves is identical to the size of the static field. In all derivations above, fringing fields were not considered.

In reality, the fringing fields due to the open and closed ends of a coaxial structure distort the field structure such that the assumptions used with Ampere's and Gauss's laws above are no longer valid. For the treatment of a similar structure taking account of fringing fields, see [3]

2.4. – Quality Factor of Resonant TEM Modes in Coaxial Cavities

The quality factor of the 1/4λ open-ended coaxial resonator shown in figure 1.2 can now be estimated from the energy stored and power loss in the structure shown in figure 2.2. For completeness, the resistance of the structure is extracted from the power loss.

The radiation losses from the tip are negligible, due to the fact that the wavelength is much bigger than the size of the tip [4]. Therefore the radiation quality factor is considered infinite.

The dielectric quality factor of the sapphire disc (and hence the resonator) is inversely proportional to the loss tangent of the sapphire, and therefore large due to the small loss tangent of sapphire. The electric field inside the sapphire is small due to the gold coating on both sides meaning the power loss in the sapphire is low compared to the energy stored throughout the entire resonator resulting in a large dielectric quality factor. Hence the dielectric quality factor is assumed infinite and $Q_0 \approx Q_C$. Therefore only the conduction quality factor is considered.

To find the quality factor of the resonator the energy stored is found first, followed by the power dissipated in the structure [5]. Both are found from use of equation (2.12).

The energy stored, *U*, in a TEM mode of an open ended coaxial resonator is given [5] by

$$U = \mu_0 \int_{Vol} \left|\underline{H}\right|^2 \cdot dV = \frac{\mu_0 I^2}{8\pi^2} \int_0^l \int_0^{2\pi} \int_a^b \left(\frac{1}{r}\right)^2 \cdot \sin^2(kz) \cdot r dr d\phi dz \,. \tag{2.13}$$

In equation (2.13) the time dependence has been averaged and cylindrical coordinates have been used. If the cavity length supports an odd integer number of ¼ wavelengths, *n*, then the integration results [5] in

$$U = \frac{\mu_0 I^2 l \ln(b/a)}{8\pi} \tag{2.14}$$

The power loss, P_L, of a TEM mode of an open ended coaxial resonator is given [5] by

$$\begin{aligned} P_L &= \frac{R_s}{2} \int \left|H_{\text{Stand}}\right|^2 ds = \frac{R_s}{2} \int_0^l \int_0^{2\pi} \left(\frac{I}{2\pi r}\right)^2 \cdot \sin^2(kz) \cdot a d\phi dz + \\ &\frac{R_s}{2} \int_0^l \int_0^{2\pi} \left(\frac{I}{2\pi r}\right)^2 \cdot \sin^2(kz) \cdot b d\phi dz + \frac{R_s}{2} \int_0^{2\pi} \int_a^b \left(\frac{I}{2\pi r}\right)^2 r dr d\phi \end{aligned} \tag{2.15}$$

The three integrals on the right hand side of equation (2.15) correspond to the power dissipated in the inner, outer and top conductors respectively of a coaxial resonator closed at one end [5]. Carrying out the integrations results in

$$P_L = \frac{R_s I^2 l}{8\pi} \left[\frac{1}{a} + \frac{1}{b} + \frac{2\ln(b/a)}{l}\right]. \tag{2.16}$$

Note that the actual resonator shown in figure 1.2 has an additional bottom plate conductor. Although the bottom conductor is not shorted to the tip, it is not quite at the end of the wave (see section 4.5) and therefore feels a significant magnetic field and hence constitutes a significant loss. This effect can be accounted for simply by multiplying the last term inside the brackets of equation 2.16 by a factor of two [5]. Applying this factor of two and substituting equations 2.16 and 2.14 into equation 2.1 results [5] in the estimated unloaded quality factor of the 1/4λ open ended coaxial resonator:

$$Q_0 = \frac{\mu_0 \omega \ln(b/a)}{R_s\left[\frac{1}{a}+\frac{1}{b}+\frac{4\ln(b/a)}{l}\right]} \tag{2.17}$$

Substitution of the surface resistance of copper of 3.53mΩ (the surface resistance was calculated at the resonant frequency of the resonator and the conductivity of copper, of 59MSm^{-1}) and the dimensions of the cavity stated above into equation (2.17) results in a calculated, unloaded quality factor of 4206. This result is discussed in section 4.2 in the context of the measured and simulated unloaded quality factors.

The resistance of the cavity can also be extracted from equation (2.16) by putting $P_L = I^2R$. In which case the resistance is

$$R = \frac{R_s l}{8\pi}\left[\frac{1}{a}+\frac{1}{b}+\frac{2\ln(b/a)}{l}\right]. \tag{2.18}$$

2.5. – Modes of an Open-Ended Coaxial Cavity

This section describes analytical equations to find the resonant frequencies of the TE, TM and TEM modes in an open ended coaxial resonator.

The resonant frequency of the TEM mode is simply given by $f_0 = 1/2\pi\sqrt{LC}$, where the inductance, L and the capacitance, C can be derived using the static solutions from Ampere's and Guass' laws as shown above.

The wavelength of resonance of TE and TM modes in the guide, λ_g, can be described [2] by

$$\lambda_g = \frac{\lambda}{\sqrt{1-\left(\frac{\lambda}{\lambda_c}\right)^2}}, \tag{2.18}$$

where λ is the free space wavelength and λ_c is the cut-off wavelength of the mode. The cut-off wavelengths of the TE and TM modes can be found by solving Bessel-Neumann combination equations [2]. For the TM_{mn} modes (where *m=0,1,2,3…* and *n=1,2,3…*), the cut-off wavelength is given by

$$\lambda_{cTM} \approx \frac{2(b-a)}{n}, \tag{2.19}$$

where and *b* and *a* are the radii of the inner and outer conductors of the coaxial waveguide, as shown in figure 1.2.

For the TE_{m1} modes, the cut-off wavelength is given [2] by

$$\lambda_{cTE} \approx \frac{\pi(b+a)}{x} \text{ for } x = 1,2,3\ldots \tag{2.20}$$

However, for the TE_{mn} modes the cut-off wavelength is given [2] by

$$\lambda_{cTE} \approx \frac{2(b-a)}{(y-1)} \text{ for } y = 2,3,4\ldots \tag{2.21}$$

The cut-off wavelengths for all TE and TM modes can be substituted into equation (2.18), which can then be solved for the free space wavelength. The free space wavelength can be substituted into the equation $c = \lambda f$ to find the free space frequency which is identical to the resonant frequency for that mode. To solve equation (2.18) for the free space wavelength, the wavelength in the waveguide must be known for each mode.

The wavelength in the guide is found by applying the boundary conditions of an open ended coaxial resonator to the particular mode. However, even though the cavity is open-ended the TE modes still exhibit an electric field minimum at the open end (see section 4.5). Therefore, specific boundary conditions must be applied to each mode.

The field patterns inside a section of coaxial line are shown [2] in figures 2.3a and 2.3b for the first TM and TE modes respectively.

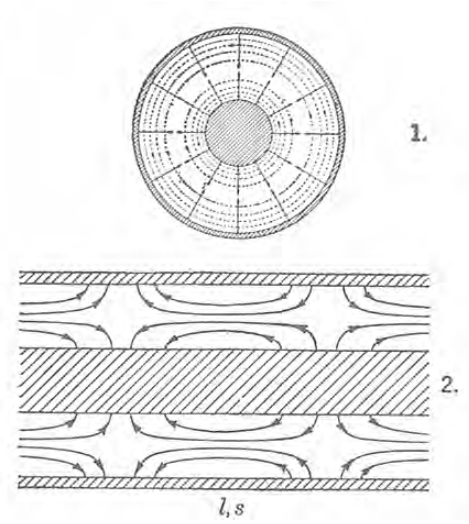

Figure 2.3a Drawing taken from [2] showing the magnetic field lines through a cross section labelled, 1, and the electric field lines along the length labeled, 2, for the TM_{011} mode.

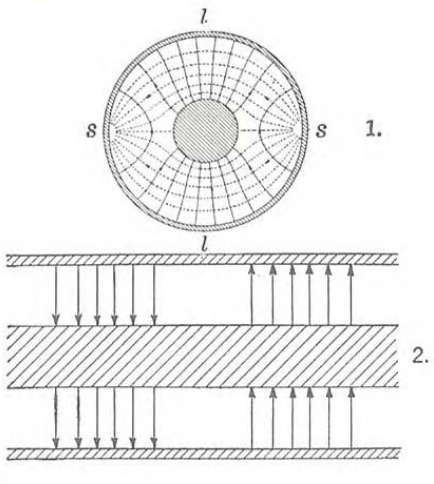

Figure 2.3b Drawing taken from [2] showing the magnetic field lines through a cross section labelled, 1, and the electric field lines along the length labeled, 2, for the TE_{111} mode.

The analytical values of the resonant frequencies of the modes were solved and the results are shown in section 4.5 where they are compared to network analyser measurements and the results of simulations.

2.6. – Coupling to Resonators

Coupling is the mechanism by which energy is fed into and extracted from the resonator. It is achieved by terminating the inner conductor of the co-axial wires from the PNA in an open circuit or a loop to ground, inside the resonator.

The coupling coefficient, β, is defined [6] as the ratio of the unloaded and external quality factors.

$$\beta_1 = \frac{Q_0}{Q_{e1}} \qquad \beta_2 = \frac{Q_0}{Q_{e2}}, \tag{2.22}$$

where β_1 and β_2 are the coupling coefficients associated with port 1 and 2 of two port measurements respectively. For symmetrical coupling ($\beta_1 = \beta_2$), substitution of the definitions of the unloaded and external quality factors into equation (2.22) results in

$$\beta = \frac{P_e}{P_0} = \frac{P_{out}}{P_0}, \tag{2.23}$$

where P_0 is the total power dissipated in the resonator (this is energy converted to heat and in the present case includes losses from the cavity walls and any sample present). P_e is the power lost through the coupling ports, or power coupled out of the resonator through the ports. P_e does not represent energy dissipated as heat but simply power coupled out of the resonator. For two port measurements, the external quality factor can be shown to be

$$Q_e = \omega \cdot \frac{U}{\beta P_0}. \tag{2.24}$$

P_e, and hence β, are determined by the length of wire or diameter and orientation of the loop used to achieve the coupling. It is assumed that the coupling wire itself presents small Ohmic

losses and hence does not alter P_0 significantly. This is valid provided that the coupling wire is free from surface dirt and that a loop involves little solder, both of which can be quite lossy. The amount of power coupled out of the resonator, P_e, will also depend on the strength, frequency and structure of the fields in the vicinity of the coupling loop which will depend on the mode. Therefore each resonant mode will have a different coupling coefficient.

For two port measurements with identical coupling, equation (2.2) becomes

$$\frac{1}{Q_L} = \frac{1}{Q_0} + \frac{2}{Q_e}. \tag{2.25}$$

Substitution of equation (2.23) into equation (2.25) results in

$$Q_L = \frac{Q_0}{1+2\beta}. \tag{2.26}$$

Equation 2.26 shows that when the coupling coefficient, β, is small $Q_L \approx Q_0$ which is analogous to $Q_e >>> Q_0$.

The coupling coefficient can be found directly from measurements of the S parameters. For two port measurements, β can be found from

$$S_{21}(f_r) = \frac{2\beta}{1+2\beta}, \tag{2.27}$$

where $S_{21}(f_r)$, the transmission coefficient at the resonant frequency, is the ratio of the output to the input voltage amplitudes.

Similarly the reflection coefficient at the resonant frequency is given by

$$S_{11}(f_r) = \frac{1}{1+2\beta} \tag{2.28}$$

Equation (2.27) is plotted in figure 2.4.

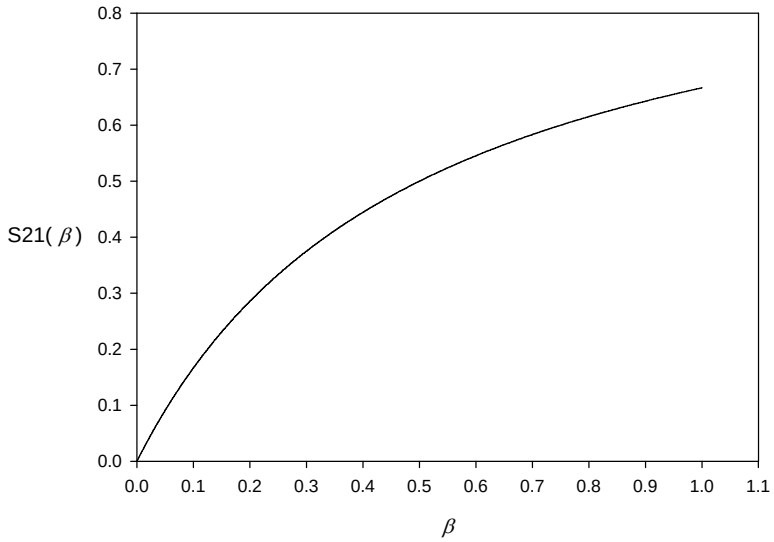

Figure 2.4 The transmission coefficient at resonance plotted as a function of the coupling coefficient.

Figure 2.4 shows the transmission coefficient at resonance plotted as a function of the coupling coefficient. This shows that the output power of a two port system can be increased by increasing the strength of coupling. It also indicates that the addition of a lossy sample to the system (changing in P_0) will create a larger change in S_{21} due to changes in β if a small value of β is utilised initially.

The coupling regulates the power lost from the resonator through the coupling ports. The upper limit of large coupling would be like a short circuit, whereas extremely small coupling will cause the resonator to appear as an open circuit to the PNA.

Chapter 2 Bibliography

[1] G. Matthaei, L. Young and E. M. T. Jones, *Microwave Filters, Impedance-Matching Networks, and Coupling Structures*, Artech House Books, USA, 1980.

[2] N. Marcuvitz. *Waveguide Handbook*. McGraw-Hill, 2nd Edition, New-York, 1951.

[3] J. D. Kraus. *Electromagnetics*, McGraw-Hill, 2nd Edition, New-York, 1973.

[4] S. Ramo, J. R. Whinery, T. V. Duzer. *Fields and Waves in Communication Electronics*. John Wiley and Sons. 1st Edition. New-York, 1965.

[5] M. J. Lancaster, *Passive Microwave Device Applications of High Temperature Superconductors*. Cambridge University Press. UK, 1997.

[6] D. M. Pozar. *Microwave Engineering*, John Wiley and Sons, 3rd Edition, New York, 1998.

Chapter 3 – Scanning Near-Field Microwave Microscopy in the Context of Dielectric Materials Research

3.1. – Introduction to Dielectric Materials

This chapter briefly discusses ferroelectric materials and combinatorial synthesis and the related use of the SNMM. The chapter concludes with an introduction to an analytical image charge model widely used in the literature, but first an introduction to dielectric materials is given.

In general, a dielectric material can be defined as a material with low conductivity due to the large energy gap between the valence band and the conduction band. Dielectrics are used within many electrical components due to their insulating properties. They are commonly used in capacitors to store energy in the form of electric fields. Studying the electrical properties of dielectrics invariably involves the application of electric fields to the material. The dielectric is then characterised by its response to the applied field.

When an electric field is applied to the dielectric, the material can become polarised. The amount of polarisation, $\underline{P}$, depends not only on the applied electric field, $\underline{E}$, but also on the dipolar properties of the structures within the material such as atoms, molecules and grains.

If the dielectric is isotropic ($\underline{P}$ is in the same direction as $\underline{E}$), homogenous ($\underline{E}$ results in the same amount of $\underline{P}$ throughout the material) and linear (there is a linear relationship between $\underline{E}$ and $\underline{P}$) the applied electric field and polarisation are related by

$$\underline{P} = \chi_e \varepsilon_0 \underline{E}\,, \tag{3.1}$$

where χe is called the electric susceptibility. The permittivity of the dielectric can be defined as

$$\varepsilon = 1 + \chi_e . \tag{3.2}$$

However, the permittivity is complex, and defined as

$$\varepsilon = \varepsilon' - i\varepsilon'' , \tag{3.3}$$

where ε' and ε'' are the real and imaginary parts of ε respectively. Substitution of equation (3.3) into equation (3.1) results in

$$\underline{P} = \varepsilon_0(\varepsilon - 1)\underline{E} = \varepsilon_0\varepsilon'\underline{E} - \varepsilon_0\underline{E} - i\varepsilon_0\varepsilon''\underline{E} = \underline{D} - \varepsilon_0(1 + i\varepsilon'')\underline{E} , \tag{3.4}$$

where *D* is the dielectric displacement. It can be seen that the permittivity describes the response of a dielectric material to an applied electric field. In equation (3.4) use has been made of the relationship

$$\varepsilon' = \varepsilon_0\varepsilon_r , \tag{3.5}$$

where ε_r is the relative permittivity.

The total loss of the dielectric is expressed through the parameter ε''. The loss is usually defined through the loss tangent which is defined as the ratio of imaginary to real parts of the measured response [1].

$$\tan\delta = \frac{\varepsilon''}{\varepsilon'} . \tag{3.6}$$

In principle, both free charge carriers and dielectric behaviour can contribute to the loss in which case

$$\tan\delta = \frac{\omega\varepsilon'' + \sigma}{\omega\varepsilon'}, \tag{3.7}$$

where σ is the conductivity associated with the free carriers. Since most measurements cannot distinguish between loss mechanisms and since most dielectric obey $\sigma << \omega\varepsilon''$, equation (3.6) will be used in this thesis.

3.2. – Ferroelectric Materials

Ferroelectric materials are characterised by the fact that they exhibit a spontaneous electric polarisation which can be reversed by the application of a sufficiently large electric field [2]. This is the electric analogue to the behaviour of ferromagnetic materials, hence the name.

Ferroelectric behaviour is occurs below the Curie temperature [3], which depends on the ferroelectric material. Near the Curie temperature, the permittivity is a strong, non-linear function of applied electric field. Above the Curie temperature the ferroelectrics behave as normal dielectrics.

Some ferroelectric materials such as Barium Strontium Titanate (BST) are commonly used for microwave devices, such as filters and attenuators. These devices are sometimes required to be made small (miniaturisation) and tuneable (have a variable frequency response). The miniaturisation of devices often requires dielectric thin films. However, in general a dielectric thin film has a much smaller permittivity than the bulk of the same material, due to differences in structural quality. Nevertheless, BST thin films have a large enough permittivity with sufficient sensitivity to electric field bias for realising tunable microwave devices.

The SNMM can be used as a sensitive characterisation tool to find grain boundaries, domains and variations in permittivity within both thin film and bulk ferroelectric and dielectric samples. This may lead to the improvement of the microwave characteristics of the films such as reduced losses, favourable to device applications. The SNMM can also be used to characterise the

tunability of ferroelectrics, as mentioned in chapter 1. To demonstrate the applicability of the SNMM to this area of research, thin films of BST were chosen to be characterised by the SNMM. These measurements are detailed in the last chapter of this thesis.

3.3. – Combinatorial Materials Research

Combinatorial synthesis refers to advancements in materials science in which many different variants of a material is produced on a single sample, also known as a "material library" [4].

Material libraries may be made through thin film deposition or ink jet delivery techniques [5]. To create a variation in the deposited material properties, shadow masks or in-situ moving masks can used to vary the amount of material deposited from several targets across the substrate surface [5]. In this way, a gradient of material composition, and hence properties, is created along the substrate surface.

The advantage of combinatorial synthesis is that many material compositions can be generated and characterised on one sample. However, this advantage is only worthwhile if a characterisation device capable of high throughput, high spatial resolution and accurate quantitative measurements is available. Scanning near-field microscopes fulfil this requirement. In fact, this combinatorial synthesis helped fuel interest in high through-put characterisation techniques such as the SNMM [4].

3.4. – Calibration of the SNMM using the Image Charge Model to Enable Quantitative Dielectric Measurements

For quantitative measurements of dielectrics the SNMM must first be calibrated. To calibrate the SNMM, resonant frequency and quality factor shifts due to a sample must be converted to measurements of relative permittivity and loss tangent respectively.

This can be done with analytical models and/or, standard samples. In any case, the resonant frequency and quality factor shifts due to samples of known relative permittivity and loss tangent must be measured. Then a function can be determined which relates frequency shift to relative permittivity and quality factor to loss tangent. For calibration, analytical models have an advantage over simple polynomial fitting in that it is sometimes possible to extend the models to special cases of samples such as thin films.

Various analytical models have been used to describe the SNMM response. In general, these include lumped element models [6, 7] and the image charge model [8]. Numerical finite element methods have also been applied to the SNMM in order to predict the response to both bulk and thin film samples [9, 10]. Modelling has been applied to both the full (resonator and tip) [11] and simplified (tip only) [9, 10] cases.

The image charge model remains the most widely used analytical model, as it not only describes the response to bulk samples (when the dimensions of the sample are much bigger than all the dimensions of the tip) but also the response to thin films on a substrate and experimental parameters such as the tip to sample distance [8]. It also provides a physical picture of the tip-sample interaction.

This model describes the frequency and quality factor shift of the ¼λ open ended coaxial resonator when a dielectric sample is brought close to the tip. The model approximates the tip above a dielectric sample as a charged sphere above an infinitely large dielectric material. The tip is modelled as a sphere because the electric field at the surface of a charged object is proportional to its radius of curvature. As the end of the tip has a much smaller radius of curvature than the rest of the tip, and is much closer to the sample, the electric field from the rest of the tip is assumed to have a negligible coupling into the sample compared to the end of the tip. The sample thickness is assumed to be much larger than the sphere/tip radius. However, measurements detailed in chapter 5 show that the size of the rest of the tip is also important.

The model also assumes the sphere to be statically charged which is valid due to the non-propagating nature of the near field [12]. The field around the tip may be considered as a near field only due to the tips small size compared to the operational wavelength of the resonator.

The model then utilises iterative image charges in the tip and dielectric to calculate the electric field around the tip and in the dielectric. According to the model, the electric field from the charged sphere polarizes the dipoles in the dielectric sample, the field from these dipoles then causes a redistribution of charges in the sphere in order to keep an equipotential surface on the sphere. This redistribution then in turn causes another redistribution of dipoles in the dielectric, and so on. Therefore the effect is modelled as an infinite series of image charges.

Therefore, the electric fields around the tip and in the sample can be calculated from the model and fields inside the cavity are calculated using methods detailed in chapter 2. Cavity perturbation theory is then applied to find the shift in resonant frequency and quality factor due to the presence of a sample [1, 13]. The fields inside resonator cavity are assumed not to change significantly. The model [8] uses a material perturbation approach [1] only, on the grounds that the volume of the sample in which the fields change is very small. Cavity perturbation theory also assumes that the introduction of a sample is a small perturbation so that the energy stored is constant. However, measurements show that the energy stored inside the cavity changes by up to 30% on approach to a sample.

The frequency and quality factor shifts predicted by the model when the tip is in contact with a bulk dielectric sample are given by the equations

$$\frac{\Delta f_r}{f_r} = \frac{f_r - f'}{f_r} = A \cdot \left[\frac{\ln(1 - w(\varepsilon))}{w(\varepsilon)} + 1 \right] = A \cdot H(\varepsilon) \tag{3.8}$$

and

$$\Delta\left(\frac{1}{Q_0}\right) = \Delta\left(\frac{1}{Q_0} - \frac{1}{Q_0'}\right) = -\frac{\Delta f_r}{f_r} \cdot \left[B + \tan\delta\right], \tag{3.9}$$

where $w(\varepsilon)=(\varepsilon_r - 1)/(\varepsilon_r + 1)$. Here, f' and Q_0' are the resonant frequency and unloaded quality factors when no sample is present. A and B are calibration constants which must be found from fitting equations (3.8) and (3.9) to measurements of standard samples.

To find the calibration constant *A*, measurement results of $\Delta f_r/f_r$ can be plotted against $H(\varepsilon) = \ln[1 - w(\varepsilon)/w(\varepsilon)] + 1$ to produce a straight line of gradient *A*. Similarly the calibration constant, *B*, can be found by plotting $\Delta(1/Q_0)/\Delta f/f$ vs $\tan\delta$ in which case, *B*, is the value of the y intercept of a straight line with a gradient of one.

In [8] the calibration constant, *A* is estimated from

$$A \approx \frac{16 R_0 \ln(b/a)}{\lambda}, \tag{3.10}$$

where R_0 is the radius of the end of the tip and λ is the wavelength. The presence of λ shows that *A* may differ for different resonant modes of the resonator. This effect is demonstrated in chapter 5.

The image charge model [8] also describes the response of the resonator as the tip to sample distance is varied. In this case equation (3.8) is altered [8] to become

$$\frac{\Delta f_r}{f_r} = \frac{f_r - f'}{f_r} = A \cdot \sum_{n=1}^{\infty} \frac{w(\varepsilon) \cdot t_n}{u_n + u_1}, \tag{3.11}$$

where u_n is defined by

$$u_n = 1 + \frac{g}{R_0} - \frac{1}{1 + u + u_{n-1}} \tag{3.12}$$

and

$$u_1 = 1 + \frac{g}{R_0}. \tag{3.13}$$

Here, *g* is the gap between the tip and the sample and R_0 is the radius of the end of the tip. t_n is given in [8] by

$$t_n = \frac{t_{n-1} \cdot w(\varepsilon)}{1 + u + u_{n-1}} \ , \ t_1 = 1 . \tag{3.14}$$

The image charge model [8] predicts the response of the SNMM to a dielectric thin film on a substrate via equations (3.15) and (3.17) from reference [8]:

$$\left(\frac{\Delta f_r}{f_r}\right)_{TF} = -A\sum_{n=1}^{\infty}\sum_{m=0}^{\infty} b_{eff}^{n-1} b_{20}^{m} b_{21}^{m} \left[\frac{b_{20}}{n+1+2mn\dfrac{g}{R_0}} - \frac{b_{21}}{n+1+2(m+1)n\dfrac{g}{R_0}}\right], \tag{3.15}$$

where

$$b_{eff} = b_{20} + \left(b_{10} - b_{20}\right)\exp\left[-0.18\frac{g}{R_0\left(1-b_{20}\right)}\right]. \tag{3.16}$$

In equations (3.15) and (3.16) $b_{20} = (\varepsilon_r - 1)/(\varepsilon_r + 1)$, $b_{10} = (\varepsilon_1 - 1)/(\varepsilon_1 + 1)$, $b_{21} = (\varepsilon_r - \varepsilon_1)/(\varepsilon_r + \varepsilon_1)$, ε_r and ε_1 are the relative permittivity of the film and substrate respectively, $a = d/R_0$, d is the thickness of the thin film and R_0 is the radius of the tip.

Because the extent of the near field around the tip in air is approximately the diameter of the tip [8], any samples measured must be ~100 times thicker than the tip diameter to be considered bulk and hence applicable to the image charge model [8].

The shift in quality factor due to a thin film on a substrate was shown [8] to be

$$\Delta\left(\frac{1}{Q}\right)_{TF} = A\sum_{n=1}^{\infty}\sum_{m=0}^{\infty} b_{eff}^{n-1} b_{20}^{m} b_{21}^{m} \left[\begin{array}{l}\dfrac{\tan\delta_2}{n+1+2mn\dfrac{g}{R_0}} - \dfrac{\tan\delta_2}{n+1+2(m+1)n\dfrac{g}{R_0}} \\ + \dfrac{2\varepsilon_1\varepsilon_2\tan\delta_1}{(\varepsilon_r+\varepsilon_1)(\varepsilon_r+\varepsilon_0)(n+1+2(m+1)na)}\end{array}\right] - B\frac{\Delta f}{f_0} \tag{3.17}$$

In equation (3.17) $tan\delta_1$ and $tan\delta_2$ are the loss tangents of the substrate and film respectively.

Chapter 3 Bibliography

[1] D. M. Pozar. *Microwave Engineering*, John Wiley and Sons, 3rd Edition, New York, 1998.

[2] F. Jona and G. Shirane. *Ferroelectric Crystals*, Dover Publications, New York, 1993.

[3] C. Kittel. *Introduction to Solid State Physics*, John Wiley and Sons, 7th Edition. USA, 1996.

[4] C. Gao, B. Hu, I. Takeuchi, and K.-S. Chang. "Quantitative scanning evanecsent microwave microscopy and its applications in the characterization of functional materials libraries", *Meas. Sci. Technol.* vol. 16. pp. 248, 2004.

[5] M. Ohring. *Materials Science of Thin Films, Deposition and Structure*. Academic Press. 2nd Edition, London, 2002.

[6] R. A. Kleismit, M. K. Kazimierczuk, and G. Kozlowski, "Sensitivity and resolution of evanescent microwave microscope, *IEEE. Trans. microw. Theory tech*, vol. 54, pp. 639, 2006.

[7] A. Tselev and S. M. Anlage, "Broadband dielectric microwave microscopy on micron length scales", *Rev. Sci. Instrum*. vol. 78, pp. 044701, 2007.

[8] C. Gao, and X.-D. Xiang, "Quantitative microwave near-field microscopy of dielectric properties", *Rev. Sci. Instrum.*, vol. 69, pp. 3846, 1998.

[9] J. H. Lee, S. Hyun, and K. Char, "Quantitative analysis of scanning microwave microscopy on dielectric thin film by finite element calculation", *Rev. Sci. Instrum.*, vol. 72, pp. 1425, 2001.

[10] D. E. Steinhauer, C. P. Vlahacos, F. C. Wellstood, and S. M. Anlage, "Quantitative imaging of dielelctric permittivity and tunability with a near filed scanning microwave microscope," *Rev. Sci. Instrum.*, vol. 71, pp. 2751, 2000.

[11] Y. C. Chen, Y.-S. Hsieh, H.-F. Cheng, and I.-N. Lin, "Study of microwave dielectric properties of perovskite thin films by near-field microscopy", *J. Electro. Ceram.* , vol. 13, pp. 261, 2004.

[12] S. Ramo, J. R. Whinery, T. V. Duzer. *Fields and Waves in Communication Electronics*. John Wiley and Sons. 1st Edition. New-York, 1965.

[13] R. A. Waldron. “Perturbation theory of resonant cavities”, *Proc. IEE*, vol. 107C, pp. 272, 1960.

Chapter 4 – Optimization and Operation of the SNMM

4.1 – Introduction

It is important that any system designed for characterisation is reliable, quantitative, robust and yields repeatable data. Also, any system which is designed to fulfil a specific role should be optimised for that role.

In the case of the SNMM, the system should have the qualities of high spatial resolution, sensitivity and accuracy, and be versatile. The SNMM is versatile in the different samples it can measure due to the fact that the probing field is outside the cavity and little sample preparation is required. The SNMM has the potential to fulfil the other qualities mentioned above due to the fact that it uses a small near field (good spatial resolution) attached to a resonating cavity (enabling sensitive measurements).

Every resonator used for measurements should be optimised in terms of the material intended to be measured. This requires some prior knowledge of the material properties of the sample. This is also important if cavity perturbation theory is to be used, as some samples (depending on the measurement system) may make the approximations of the theory invalid.

When making measurements using resonators a high quality factor is often desirable. Extremely lossy samples may decrease the quality factor so much that the signal to noise ratio is not good enough for measurements. In these cases, increasing the coupling strength may provide a solution.

This chapter describes the investigations into the correct optimisation and operation of the SNMM for measuring dielectrics.

4.2 – Quality Factor and Design of the Cavity

The unloaded quality factor of an open ended coaxial cavity is determined partly by the dimensions of the cavity. The quality factor of an open ended coaxial cavity was derived in section 2.4 as

$$Q_0 = \frac{\mu_0 \omega \ln(b/a)}{R_s\left[\frac{1}{a}+\frac{1}{b}+\frac{4\ln(b/a)}{l}\right]}. \qquad (2.17)$$

Equation (2.17) is plotted in figure 4.1 as a function of the ratio of the outer to inner conductor radii , *b/a*, for several different lengths of cavity. The outer radius, *b*, was kept at a constant value of 17mm while *a* was increased from 1mm to 10mm. Equation (2.17) was solved for cavity lengths of 40mm, 50mm and 60mm, which correspond to fundamental mode resonant frequencies of 1.875GHz, 1.5GHz, and 1.25GHz respectively. The surface resistance, R_s, being a function of frequency, was changed accordingly for the different lengths.

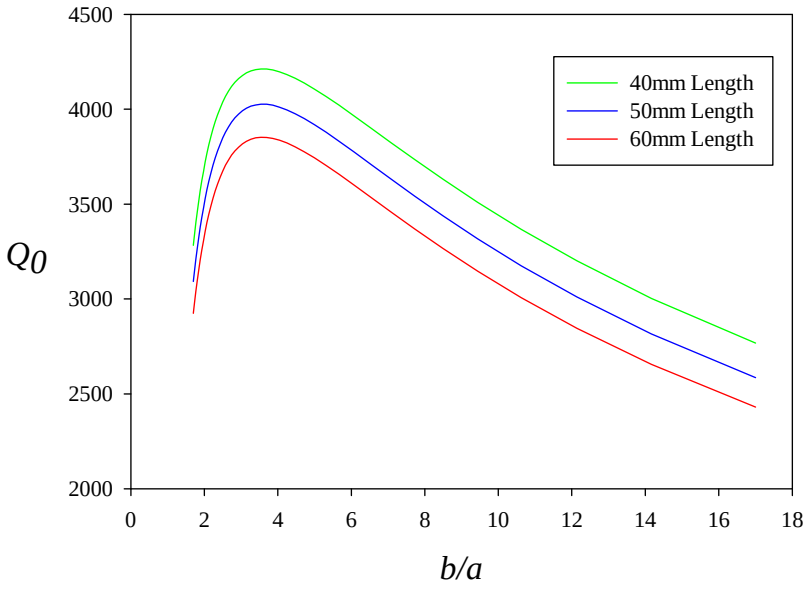

Figure 4.1 The unloaded *Q*-factor of a coaxial cavity as a function of the ratio of the outer to inner conductor radii , *b/a*. The graph shows the quality factor for cavities of lengths 40mm, 50mm and 60mm.

It can be seen from figure 4.1 that the quality factor of the cavity reaches a maximum when the ratio, *b/a* is equal to 3.7 for any length of cavity. When *b/a* = 3.7, the characteristic impedance of

the cavity is 75Ω. If the cavity were filled with a dielectric of permittivity equal to that used in coaxial transmission lines, the maximum quality factor would occur at an impedance of 50 Ω.

Figure 4.1 also shows that a cavity of smaller length (higher resonant frequency) results in a larger quality factor. From equation (2.17) one would expect a larger cavity length to result in a larger quality factor. However, it is the decrease in resonant frequency due to the increase in cavity length which is responsible for the smaller quality factor.

The calculated maximum values of the unloaded quality factors are ~4000. However, the measured values are ~1200. There are several differences between the real cavity and the model used in this calculation which may be responsible for this discrepancy. The real cavity has a tapered inner conductor ending in a tungsten tip. This may result in large losses due to the increased current density at this point as compared to the model. Also, the real cavity contains a coupling mechanism containing solder, which is lossy. The real cavity also contains a dielectric near the tip which may contribute extra losses. Even though low loss dielectric is used here, the large electric field may make the losses significant.

Future work to improve the resonator could be to determine the main source of loss in the resonator and take steps to improve it.

4.3. – Taking Measurements of known Dielectric Samples and Data Processing Techniques

Accurate measurements, with calculations of uncertainties, must be included in results of SNMM measurements for its verification as a reliable dielectric characterisation tool. Erroneous conclusions due to improper measurement technique and analysis must be avoided in the evaluation of this, and other, new measurement techniques.

This section describes the measurement method used to ensure accurate results by taking into account signal leakage. Some precautions taken before measuring calibration samples are detailed. Finally a brief description of the automation of measurements is given.

4.3.1 – Fitting Data to a Model to Account for Signal Leakage

When measuring resonant frequency and *Q* it is common practice to take the resonant frequency as that at which the largest value of $|S_{21}|$ occurs and to use the -3dB points to calculate the quality factor. This is referred to an “amplitude only method”.

The -3dB points method is an approximation and only applicable when *Q* is large [1]. It is based on an equivalent circuit in which only one resonance can occur. However, resonators may support more than one mode at the same frequency which may be hidden in an amplitude only representation.

The amplitude only method also relies on the resonance curve exhibiting the well known Lorentzian shape. However, one often encounters asymmetrical resonance curves which can lead to uncertainties (especially in *Q* measurement) when using the -3dB point method [2]. An asymmetrical resonance curve is an indication that an amplitude only measurement is insufficient.

Experimental examples of asymmetrical resonance curves are shown in figure 4.2, in which $|S_{21}|$ is plotted as a function of frequency across the fundamental resonant mode of the resonator. Figure 4.2 shows a resonance curve on the right which is clearly asymmetrical. While the resonance curve on the left of figure 4.2 may not appear asymmetrical at first glance, there can be large measurement uncertainties in *Q* if the phase is not taken into account in this case.

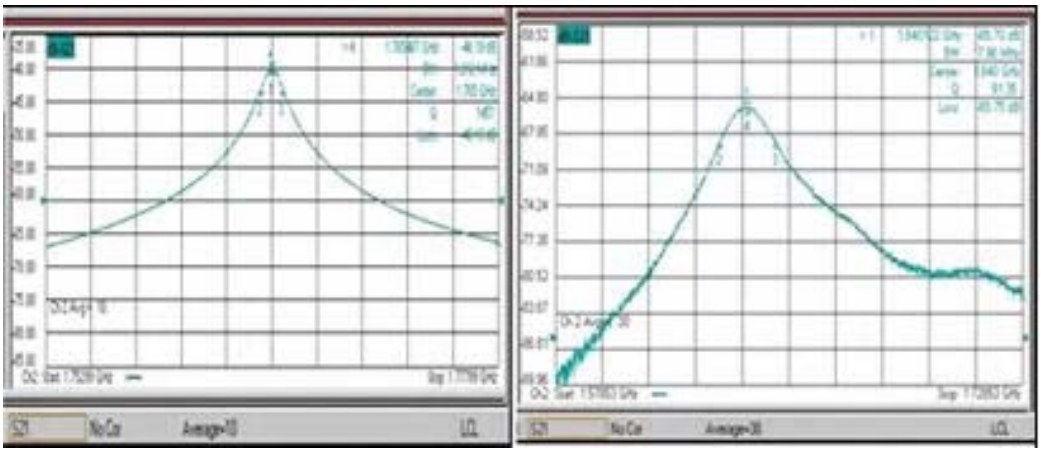

Figure 4.2 Examples of asymmetrical resonance curves

Asymmetrical resonance curves can be caused by over-coupling, degenerate or overlapping modes or signal leakage [2]. Over-coupling and degenerate or overlapping modes should generally be avoided whilst taking measurements. However, signal leakage can be accounted for by a full complex analysis of the transmission coefficient (for two port measurements).

Signal leakage is the leakage of signals directly from one port to the other without those waves resonating within the resonator. Figure 4.3 shows a drawing depicting signal leakage.

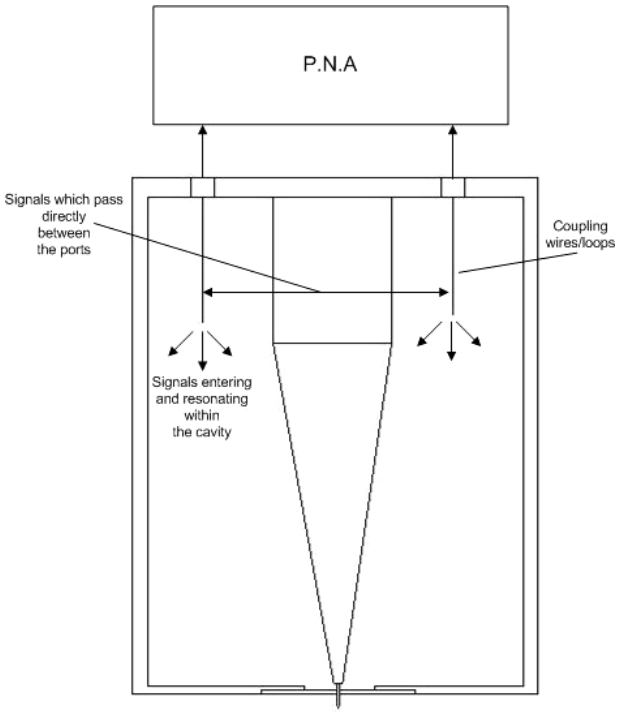

Figure 4.3 Drawing to depict signal leakage between coupling ports

The effect of signal leakage can be accounted for by using the following modified equation for the complex transmission coefficient [2]

$$S_{21} = L + \frac{S_{21}(f_r)\cdot e^{-2j\delta}}{1 + jQ_L\Delta} \tag{4.1}$$

where $L = L' + jL''$ is the complex leakage vector, $\Delta = (f^2 - f_0^2)/f^2$ and δ is a phase factor which accounts for phase changes due the to transmission lines and ports. In most resonators, and also in the present case, the coupling loops cause a phase change to the signal which is practically impossible to calibrate away because the coupling wires are inside the resonator itself. The phase factor δ can account for this.

Equations which describe a lumped element *LRC* resonant circuit show that the real and imaginary parts of the transmission coefficient at the resonant frequency $(\Delta = 0)$, are maximum and zero respectively. However, this is not the case for the resonator detailed in this thesis. This is illustrated in figure 4.4 which shows measurements of the magnitude, real and imaginary parts of S_{21} for the resonator.

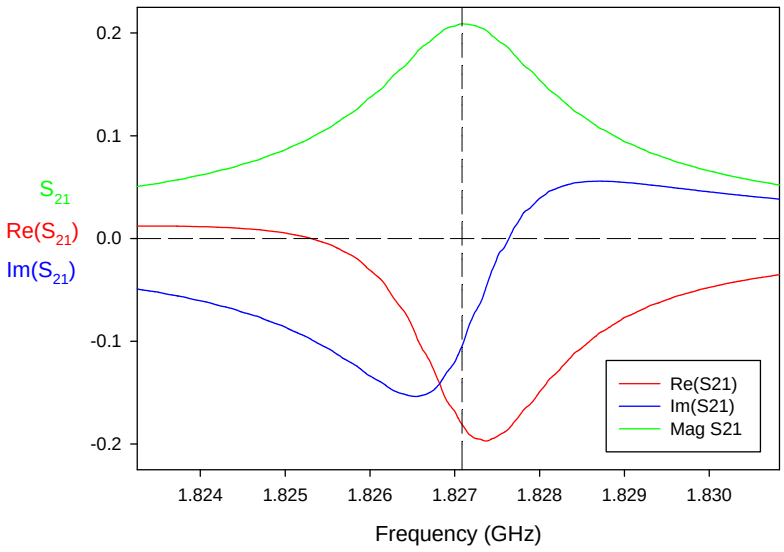

Figure 4.4 Graph showing magnitude of S_{21} and the real, imaginary and parts as a function of frequency.

Equation (4.1) can be split into its real and imaginary parts by multiplying the top and bottom of the denominator by the complex conjugate of the denominator. This results in equations (4.2) and (4.3).

$$\mathrm{Re}(S_{21}) = L' + \frac{S_{21}(f_r)\cos(2\delta) - Q_L \Delta S_{21}(f_r)\sin(2\delta)}{(1+Q_L\Delta)^2} \tag{4.2}$$

$$\mathrm{Im}(S_{21}) = L'' + \frac{-Q_L \Delta S_{21}(f_r)\cos(2\delta) - S_{21}(f_r)\sin(2\delta)}{(1+Q_L\Delta)^2} \tag{4.3}$$

The leakage vector, *L*, is usually small in practice. Therefore, at the resonant frequency $Re(S_{21})$ will reduce to $\approx S_{21}(f_r)\cos(2\delta)$ and the $Im(S_{21})$ to $\approx -S_{21}(f_r)\sin(2\delta)$. Since the magnitude is the square root of the sum of the squares, and $(\cos^2 2\delta + \sin^2 2\delta)=1$, the magnitude will always reduce to $S_{21}(f_r)$ no matter the value of the uncalibrated phase shift, δ. This means, in principle, the resonant frequency (as measured by the magnitude) is unaffected by the uncalibrated phase shift. However, a magnitude only measurement of the resonant frequency using markers can lead to significant uncertainties if the curve is extremely asymmetrical.

A finite leakage vector, *L*, will alter the measurement of the resonant frequency. The leakage vector is a function of the frequency. However, it is assumed to be constant because only small changes in frequency are required to measure the *Q*, when the *Q* is high. The phase, δ, is also a function of frequency but is assumed constant over the small frequency band used for the measurement.

Measurements of the complex transmission coefficient can be fitted to equation (4.1) so that the correct resonant frequency and quality factor can be extracted. To do this measurements of the $Im(S_{21})$ are plotted against the $Re(S_{21})$ to form an imperfect circle. A typical example is shown in figure 4.5.

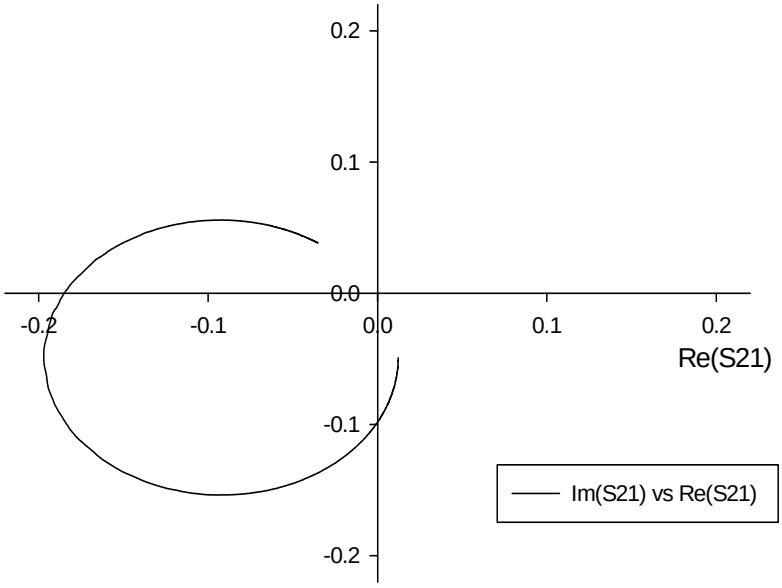

Figure 4.5. Graph showing *Im(S_{21})* vs *Re(S_{21})* from a typical measurement. The imperfect circle indicates that the resonance curve is asymmetrical.

The origin of the circle is given by the complex leakage vector, while the diameter is given by the magnitude, $S_{21}(f_r)$. The phase shift, δ, determines the orientation of the circle about the origin. Q_L and f_r determine how much of the circle is traced out (this also depends on how many measurement points are being used). The points nearer the origin are furthest away from the resonant frequency. It can be seen that this method is more accurate because it uses all the data rather than just three frequency points, as in the -3dB method.

Another circle is then plotted on the same axis using estimated values of Q_L, f_r, Δ, δ *and* $S_{21}(f_r)$. The estimated values of these parameters are then changed automatically by a least squares fitting program written in Excel until the sum of the differences between the measurement values and the estimated values is zero.

During the minimisation of functions in least squares fitting more weight will be given to values where the function to be minimised is largest. This means those points would dominate the minimisation process [3]. In the case of asymmetrical resonance curves, this can be avoided by simply using fewer points centred around the resonant frequency. This is because the asymmetry becomes more apparent further away from the resonant frequency as can be seen in figure 4.2.

In the present system, mechanical noise (see section 4.6.3) can be a problem if the tip is not held in contact with the sample strongly enough, in which case it can "bounce" in and out of contact making the response oscillate between two values. In this case, an average must not be used as the difference between the in and out of contact values are so large. Alternatively, the fitting routine must be modified or used manually to fit to the in-contact data points.

It should be noted that the effects described above may be stronger when taking measurements at low levels of S_{21}. This includes very lossy samples or low Q resonators.

4.3.2 – Precautions and Considerations when Measuring Dielectric Samples

Calibration of measurement devices is important for accurate measurements. When dielectric standards are used in the calibration, the standards must have traceable measurement data as a function of frequency, including uncertainties.

In order to evaluate the SNMM as a measurement device, dielectric standards were needed including measurement data of those standards at the frequencies intended for use.

The dielectric standard samples used were neodymium gallate ($NdGaO_3$), yttria-stabilized zirconia (YSZ) and magnesium oxide (MgO) 10mm by 10mm by 0.5mm substrates and standard samples of peek and macor obtained from the UK National Physical Laboratory (NPL). The peek and macor samples were approximately $10mm^3$.

The complex permittivity of the YSZ, MgO and $NdGaO_3$ substrates was measured using a split post resonator [4] at 12GHz at NPL.

The resonant frequencies of the first three TEM modes ($^1/_4\lambda$, $^3/_4\lambda$ and $^5/_4\lambda$) of the coaxial resonator used in this thesis occur at ≈1.8GHz, ≈4.3GHz and ≈7.7GHz. To check that the measurements of permittivity of the YSZ, $NdGaO_3$ and MgO substrates using the split post

resonator at 12GHz were valid for the desired frequencies used in this thesis, Lynch's formula was used [5].

Lynch's formula allows the calculation of the change in relative permittivity for a given change in frequency and is given as

$$\frac{\varepsilon_1 - \varepsilon_2}{\varepsilon_1} \approx m \tan(\delta) \log_{10}\left(\frac{f_2}{f_1}\right). \tag{4.4}$$

where ε_1 and ε_2 are the relative permittivities at frequencies 1 and 2 respectively (f_1 and f_2). m is a constant which can range from 1.0 to 2.3, however a value of $m=1.5$ holds for most situations [5]. This equation is used with the assumption that $\tan(\delta)$ does not change significantly over the frequency range being considered, which is valid as long as the loss of the material is due to dielectric relaxation and not any resonance effects [2].

Equation (4.4) was plotted as a function of frequency using the relative permittivity measured (ε_1) at 12GHz (f_1), and is shown in figure 4.6.

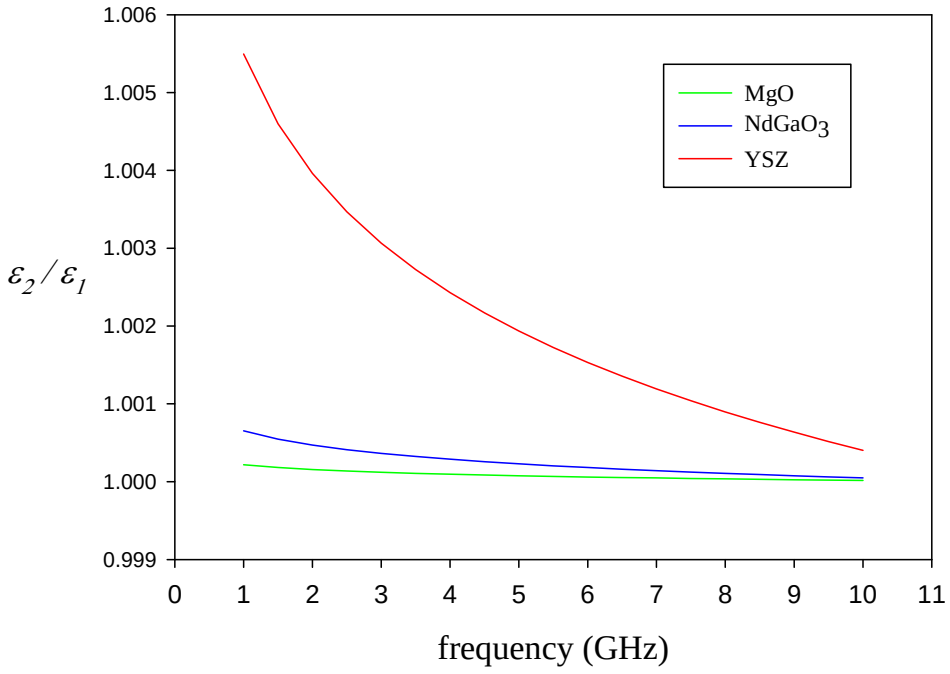

Figure 4.6 Percentage change in relative permittivity calculated using Lynch's formula for YSZ, MgO and $NdGaO_3$ samples.

Figure 4.6 shows the change in relative permittivity according to the Lynch formula for YSZ, $NdGaO_3$ and MgO samples. The permittivity measurements were normalised so that zero change occurs at 12GHz. The change in permittivity from 10GHz to 1GHz is less than 0.01% for the NdGaO3 and MgO samples. This change is much smaller than the measurement uncertainty obtained from the spit post resonator. For the YSZ substrate, figure 4.6 from 10GHz to 1GHz shows a change of ≈0.05%. This corresponds to a change of 0.0141 (for ε_r = 28.139) whereas the uncertainty from the split post resonator measurement was 0.106. Therefore, the larger uncertainty was used.

For future work, this study should be performed over a wider range of frequencies.

For the Peek and Macor samples, complex permittivity measurement data was obtained from [6] and [7] respectively.

The values of relative permittivity, loss tangent and associated uncertainties for the calibration samples are summarised in table 4.6.

	Relative permittivity, ε_r	Uncertainty in ε_r	Loss tangent, $tan\delta$	Uncertainty in $tan\delta$
Peek	3.175	0.040	$2.735 \cdot 10^{-3}$	$0.05 \cdot 10^{-3}$
Macor	6.0	0.1	$6.7 \cdot 10^{-3}$	$0.3 \cdot 10^{-3}$
MgO	9.782	0.034	$0.134 \cdot 10^{-3}$	$0.02 \cdot 10^{-3}$
$NdGaO_3$	21.599	0.263	$0.404 \cdot 10^{-3}$	$0.039 \cdot 10^{-3}$
YSZ	28.139	0.106	$3.39 \cdot 10^{-3}$	$0.1253 \cdot 10^{-3}$

Table 4.6 table summarising relative permittivity and loss tangent data used for the calibration samples.

Another precaution, which must be taken when measuring dielectric samples, is to make sure the sample itself is not excited into a resonant mode. The geometrical resonant frequencies of the standard samples were found through simulation using CST microwave design studio. Diagrams of the simulation models for each of the calibration samples are shown in figure 4.7.

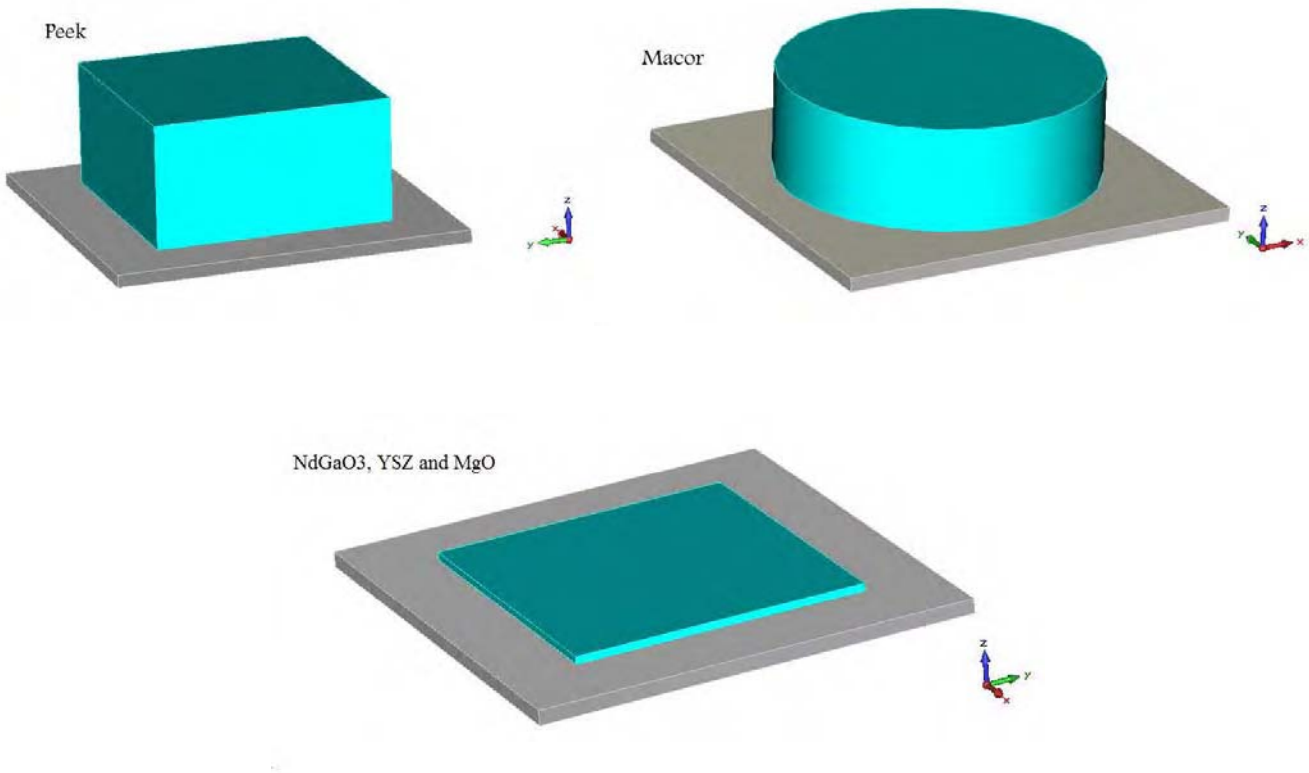

Figure 4.7. Diagrams showing the CST simulation models used to determine the resonant frequencies of each sample as dielectric resonators.

Each simulation consists of the sample on top of a grounded conductor. The simulation results are shown in figure 4.8. Figure 4.8 shows the frequencies of the resonant modes of the samples along with the range of frequencies used for the first three TEM modes of the coaxial resonator.

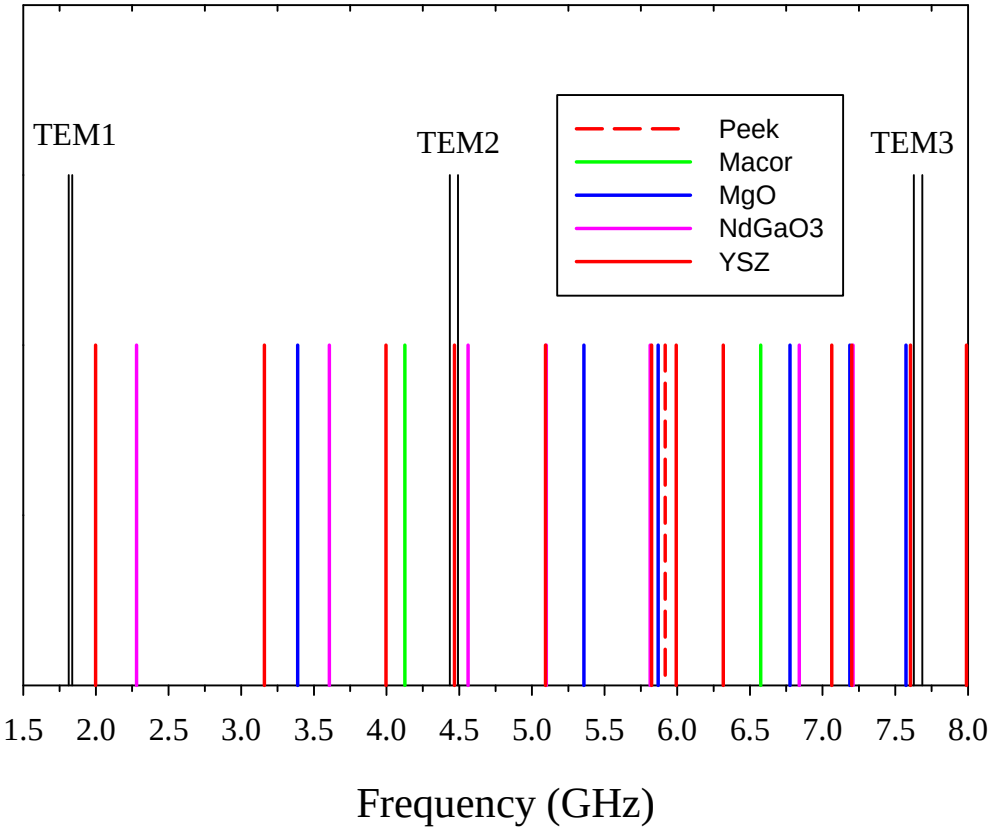

Figure 4.8. Graph showing the resonant modes of the dielectric calibration samples. The range of frequencies used for the first three TEM cavity modes are represented by two black lines.

Figure 4.8 shows some interference from modes within the YSZ and $NdGaO_3$ samples with the TEM $3/4\lambda$ mode. It also shows possible interference from modes within the YSZ and MgO samples with the TEM $5/4\lambda$ mode. Therefore, the measurement results involving these samples at the mentioned modes are judged in the light of figure 4.8.

4.3.3 – Automated measurements

A program was written using Labview software to control the Agilent E8236 PNA for taking automated measurements. This section describes some of the features of the program.

The program written in Labview had two main functions which were; a single tip-sample distance point measurement function and a sample approach function.

The single point measurement function records the real and imaginary parts of the transmission coefficient at each frequency point within a sweep. This is done for the first three TEM modes of the coaxial resonator. Approximate frequencies of the TEM modes and large initial frequency sweep band widths are supplied by the user. When the program starts it will use the marker functions of the PNA to find and zoom into the modes. The program measures the quality factor of the mode using the markers and chooses a bandwidth for the frequency sweep which is 3 times the bandwidth of the mode at the -3dB points. The program then engages the averaging of the PNA, waits until the averaging is finished and records the real and imaginary parts of the transmission coefficient at each frequency of the sweep. The program then finds the next mode and repeats the process.

The sample approach function is the same as the single point measurement function except the process is repeated for different tip to sample distances controlled by the piezo-cube. The program automatically records more data points at small tip-sample distances where the response of the resonator is changing more quickly with height above the sample. In this way, the response of various modes of the resonator can be characterised as a function of tip to sample distance.

4.4 – Coupling Energy into the Cavity

It has already been suggested in section 2.6 that the strength of the coupling to the resonator can effect the sensitivity of measurements of S_{21}, and hence loss. In the case of measurements of extremely lossy samples this can be used to make the resonator less sensitive to losses so that an adequate signal to noise ratio can be maintained.

It was the purpose of the work presented in this section to determine the effect of the coupling strength (or coupling coefficient, β) on measurements. The mechanisms by which energy is coupled into the resonator are described. The effect that the coupling strength has on the sensitivity to frequency and quality factor shifts is then derived. Finally the optimum coupling coefficient is derived when the Johnson noise in the system is taken into account.

4.4.1 – Mechanisms of Coupling Energy into the Cavity

The mechanism by which energy is coupled into the cavity can have an effect on the strength of coupling to each mode. Two different types of coupling mechanism are described here and their advantages and disadvantages are briefly discussed.

The first type of mechanism used was coupling wires (electric field coupling). Coupling wires were made by stripping back the outer conductor of the coaxial transmission lines which supplied power to the resonator to reveal the inner conductor. This was then placed through a hole in the cavity to reside within the resonator.

The second type used was coupling loops (magnetic field coupling). Coupling loops were made by stripping back the outer conductor of the coaxial transmission lines and bending the inner conductor into a loop which was soldered to the outer conductor.

In both cases the length of the coupling device in the cavity could be adjusted from outside the cavity. In general, the further in the cavity the coupling device was extended, the stronger the coupling which was produced. Diagrams of the two coupling mechanisms are shown in figure 4.9.

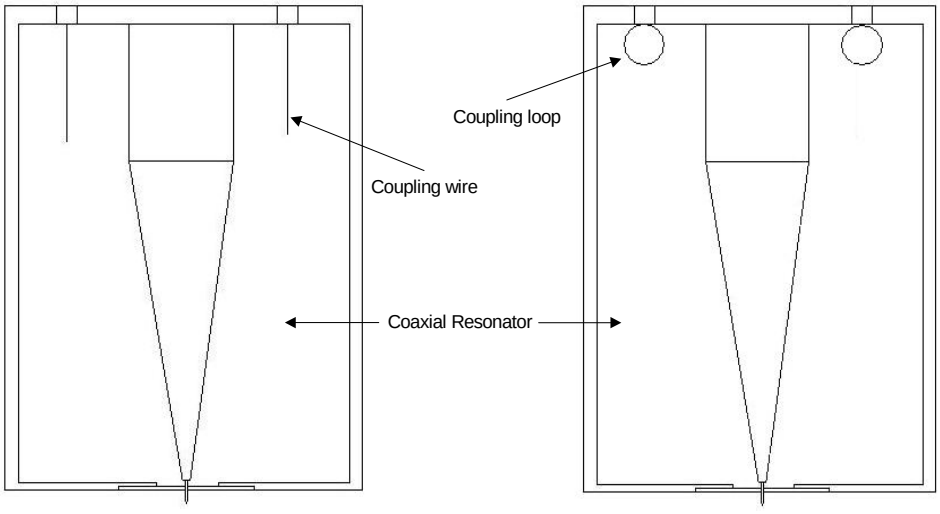

Figure 4.9. Diagram showing the two mechanisms of coupling used. Coupling loops are shown on the right and coupling wires are depicted on the left.

Coupling loops provide large coupling for modes which have a circular magnetic fields such as the TEM modes and some TM modes due to the similar orientation of the magnetic fields. The coupling loops couple to these modes so strongly that little flexibility in changing the coupling strength remains by moving the loops further in or out of the resonator.

The electric field produced by coupling wires does not couple strongly to many modes of interest. However an advantage of the coupling wires over the coupling loops is that they offer a broader range of coupling strengths. The coupling wires are also better for exciting the TM modes which may be of interest in future work. However many other unwanted modes are also excited as detailed in section 4.5.

In conclusion, for the TEM modes, coupling loops provide stronger coupling and a smaller loaded quality factors whilst the coupling wires provide smaller coupling and larger loaded quality factors. Coupling wires also provide more flexibility to change the coupling strength. Therefore, as smaller coupling is generally desired, coupling wires are preferred. However, degenerate modes must be avoided.

4.4.2 – Optimum Coupling Coefficient and Sensitivity Due to Coupling Coefficient

The optimal coupling coefficient to minimise phase noise in oscillators was derived to be $Q_L/Q_0 = 2/3$ ($\beta = 0.25$) by Everard [8], although this depends on the circuit design. This value of 2/3 was used for the case of the SNMM by Xiang *et al* [9] to determine the minimum measurable change in frequency shift in the presence of Johnson noise [10] in the system. However, as the coupling coefficient will change as a lossy sample is coupled to the cavity, a constant value cannot be used. Instead, an analysis of the sensitivity of the SNMM must include the coupling strength as a variable, which is done and presented in this section for the first time.

As the sensitivity of the system can be changed by altering the coupling coefficient, an optimum value is implied. However, the optimum value is obviously dependent on what sample is to be measured.

Therefore in the following derivation, three samples of MgO, $NdGaO_3$ and YSZ were considered. The coupling strength does not alter the sensitivity of the frequency shift to measurements of ε_r, but does alter the frequency shift due to changes in loss.

The coupling coefficient can be changed by a change in the overall loss of the system (this includes cavity and sample losses) during a measurement. It can be changed prior to a measurement by moving the wires/loops in or out of the cavity, and/or changing their size.

In terms of an equivalent LRC circuit model for the coupled resonator [11], β is given as

$$\beta = \frac{n^2 Z_0}{R}, \tag{4.5}$$

where n is the effective number of turns of a transformer modelling the coupling between the coupling wire/loop and the cavity's inductance/capacitance, Z_0 is the impedance of the input transmission line (50Ω) and R is the resistance of the system (due to sample and cavity losses). Sensitivity to losses cannot be plotted as a function of β because β itself is a function of losses. Therefore, this derivation is concerned with the position and size of the coupling mechanism, and hence, n, to determine the effect of coupling on the sensitivity.

The derivation was begun by considering the power incident at the input port of the resonator, P_i, as

$$P_i = P_0 + P_{ref} + P_{out}, \tag{4.6}$$

where P_{ref} is the power reflected from the input port, P_0 is the power dissipated in the resonator and P_{out} is the output power of the resonator. Equation (4.6) was then written in terms of scattering parameters as

$$P_i = P_0 + P_i\left|S_{11}{}^2\right| + P_i\left|S_{21}{}^2\right|. \tag{4.7}$$

If P_0 is written as V_0^2 / Z, where V_0 is the voltage drop across the resonator, and Z is the impedance of the resonator and the substitution is made, it results is

$$\frac{V_0^2}{Z} = P_i \cdot \left[1 - \left|S_{11}{}^2\right| - \left|S_{21}{}^2\right|\right]. \tag{4.8}$$

Substituting equations for S_{21} and S_{11} in terms of β given in equations (2.27) and (2.28) results in

$$\frac{V_0^2}{Z} = P_i \cdot \left[\frac{4\beta}{(1+2\beta)^2}\right]. \tag{4.9}$$

At the resonant frequency, $Z = R$, the resistance of the cavity. Also, the voltage can be expressed in terms of the capacitance and energy stored using the equation $U = ½\ CV_0^2$, where U is the energy stored and C is the capacitance. Making these substitutions gives

$$\frac{2U}{CR} = P_i \cdot \left[\frac{4\beta}{(1+2\beta)^2}\right]. \tag{4.10}$$

Making a substitution for C using $\omega^2 = 1/LC$ at resonance, where L is the inductance of the cavity and solving for ω gives

$$\omega = \sqrt{\frac{P_i R}{2LU} \cdot \left[\frac{4\beta}{(1+2\beta)^2}\right]}. \tag{4.11}$$

Now the change in ω, $\Delta\omega$, (due to a sample approach or scan) can be written as

$$\Delta\omega = \sqrt{\frac{P_i \Delta R_0}{2L\Delta U} \cdot \left[\frac{4\Delta\beta}{(1+2\Delta\beta)^2}\right]} \tag{4.12}$$

where ΔU, ΔR and $\Delta\beta$ are the changes in stored energy, resistance and coupling coefficient due to a sample approach or change in sample properties. Equation (4.12) was derived assuming that, as a dielectric sample is approached, the inductance of the resonator/sample system does not change significantly and so is not valid if the sample is a conductor or semi-conductor. Equation (4.12) gives the frequency shift due to loss changes only as it was derived from a power loss term, P_0. The function $4\Delta\beta/(1+2\Delta\beta)^2$ in equation (4.12) is small when β is small, which will create a smaller frequency shift due to losses. Since for most samples, $\varepsilon' >> \varepsilon''$, the measured frequency shift is dominated by a capacitance change of the system. However, to see the effect of the coupling coefficient on frequency shifts due to losses this is neglected temporarily.

Changes in sample loss will change R, β and $U = ½\ CV_0^2$ through a voltage change. There will be a change in the energy stored because the change in β causes a change in the reflection coefficient causing less energy to enter the cavity.

To derive the loaded quality factor shifts, equation (4.13) can be rearranged to give equation (4.14) [11].

$$U = \frac{2Q_L P_i S_{21}}{\omega} \tag{4.13}$$

$$Q_L = \frac{\omega U}{2P_i S_{21}} \tag{4.14}$$

Substituting equation (2.27) into equation (4.14) and using the symbol Δ to denote changes gives the change in quality factor due to a sample in terms of the changes in the coupling coefficient.

$$\Delta Q_L = \frac{\Delta\omega\Delta U(1+2\Delta\beta)}{4P_i\Delta\beta} \tag{4.15}$$

As the coupling coefficient, β, can be altered by either changing the coupling wire/loop size/position or by increasing the loss of the overall system, equations (4.12) and (4.15) describe the change in frequency and quality factor due to a change in the coupling mechanism or a

change in the loss of the system. To find the effect of changing the coupling wire/loop position/size only, equation (4.5) is substituted into equations (4.12) and (4.15) to give equations (4.16) and (4.17).

$$\Delta\omega = \sqrt{\frac{P_i \Delta R^2}{2L\Delta U} \cdot \left[\frac{4n^2 Z_0}{(\Delta R + 2n^2 Z_0)^2} \right]} \tag{4.16}$$

$$\Delta Q_L = \frac{\Delta\omega \Delta U (\Delta R + 2n^2 Z_0)}{4P_i n^2 Z_0} \tag{4.17}$$

Now the effects of extra losses and changing the coupling have been separated, their individual effects of the frequency shift and quality factor can be seen in equations (4.16) and (4.17). Equations (4.16) and (4.17) are now in terms of ΔR and n, which are not directly measurable quantities. However, if only directly measurable quantities are used in the derivation, the effects mentioned above are inseparable.

To plot equations (4.16) and (4.17), measurement values of ΔR were used for the samples mentioned above. A linear function of ΔU with β, which was derived from measurements, was substituted into equations (4.16) and (4.17) for ΔU. The incident power, P_i, was taken as 1mW. The inductance, L was calculated analytically from Ampere's law using the model described in chapter 2 to be $L = 1.078 \cdot 10^{-8}$H. This may be a source of uncertainty as the cavity is more complex than the simple model used to calculate the inductance. However, whether this potential uncertainty is significant or not must be left as further work.

Equations (4.16) and (4.17) are plotted in figure 4.10 as a function of the effective number of turns, n, which is a measure of the coupling strength.

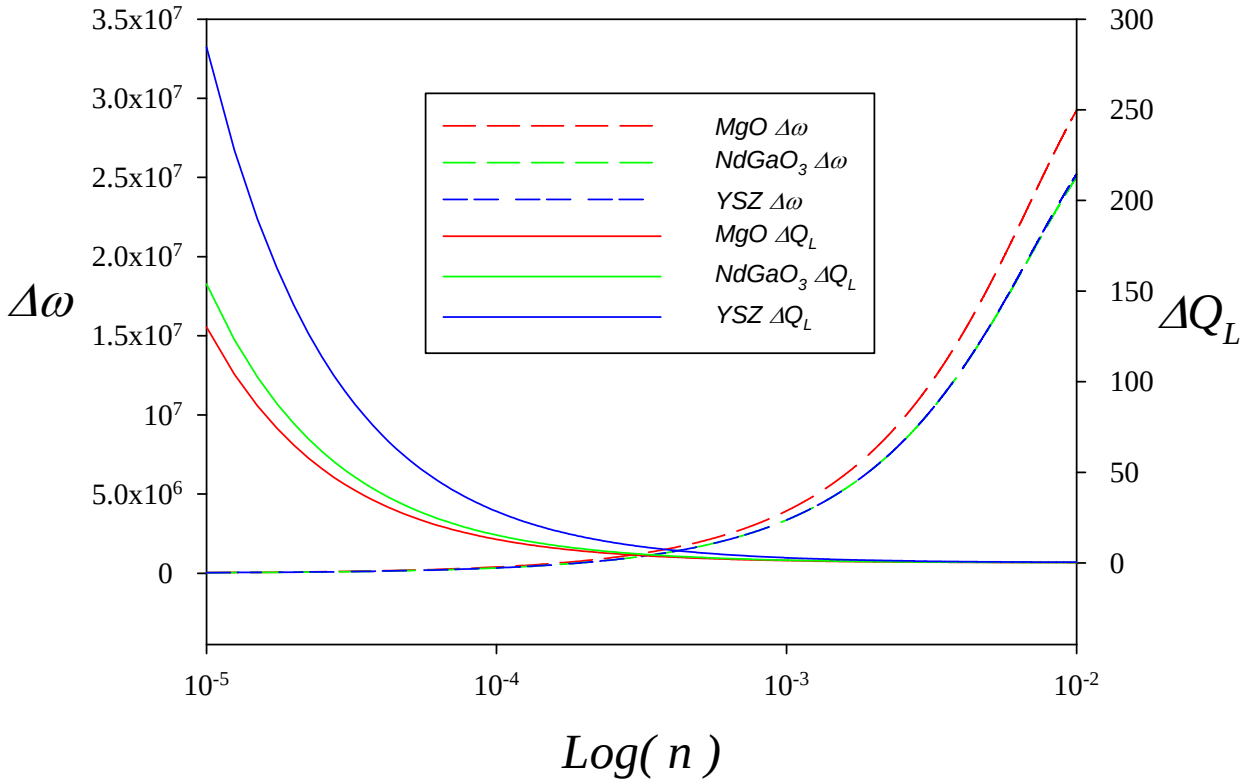

Figure 4.10. Graph showing resonant frequency and quality factor shifts of the resonator due to changes in sample loss as a function of the effective number of turns, *n*, and hence coupling strength.

Figure 4.10 shows that small coupling strength will make the resonator more sensitive to sample loss as implied by equation (2.27), whereas a large coupling strength will increase the sensitivity of the frequency shift to losses. More importantly, figure 4.10 shows that a small coupling strength makes frequency shifts insensitive to sample loss so that frequency shifts may be made due to sample ε_r only.

Hence, if a larger coupling strength is used, resulting in a smaller loaded quality factor, resonant frequency shifts due to sample losses will be difficult to separate from those due to sample ε_r.

It can be seen from figure 4.10 that an optimum coupling strength is different for each sample. However, it is clear that the coupling strength should be made as small as possible within the limits of the signal to noise ratio, and any changes in loss, and hence output power, which can be anticipated.

The derivation above is general and applies to any resonant system used for material measurements which can be modelled as an LRC circuit.

Although time did not allow, a future study could be made to compare the results shown in figure 4.10 with measurements. This should be done for each mode separately. Coupling wires should be used to achieve greater flexibility and small coupling. Also, the cavity can be re-designed to make sure degenerate modes less significant.

4.4.3. – Smallest Measurable Shifts in terms of Coupling Coefficient and Noise Analysis

In the previous section the effect of the coupling strength on the relative changes in frequency and quality factor due to sample changes were derived. It was explained in the previous section that a small coupling strength is advantageous. However, as the coupling strength is decreased the signal to noise ratio will also decrease. Therefore, given a certain noise level in a system, there must be a lower limit to the size of the coupling coefficient which can be used before a signal becomes undetectable. In this section that value of coupling coefficient is derived, together with the smallest, noise-limited, measurable changes in frequency and quality factor, in terms of the coupling coefficient. This will quantify the uncertainty in measurements of frequency and quality factor due to noise.

This minimum sensitivity of the SNMM has been calculated previously by Gao *el al* [9]. However, this was only done for a single value of the coupling coefficient. In this section the noise limited sensitivity of the SNMM is derived as a function of the coupling coefficient for the first time.

The coupling mechanism can couple both noise and signal power into the cavity. This is taken into account in the following derivation.

In general the resonant frequency of a resonator is found by finding the frequency at which maximum output power occurs. Therefore, the smallest measurable change in frequency is limited by the smallest measurable change in output power.

The difference in output power, P_{Δ}, between the resonant frequency, f_r, and an adjacent frequency off resonance, f, is

$$P_{\Delta} = P_{out}(f_r) - P_{out}(f), \tag{4.18}$$

where $P_{out}(f_r)$ and $P_{out}(f)$ are the output powers at f_r and f respectively.

Equation (4.18) can be expressed in terms of the transmission coefficient, S_{21}.

$$P_{\Delta} = P_i\left(\left|S_{21}^2(f_r)\right| - \left|S_{21}^2(f)\right|\right) \tag{4.19}$$

Using equation (2.27) and the definition of $S_{21}(f)$ given in [11], equation (4.19) can be written as

$$P_{\Delta} = \frac{P_i 4\beta^2}{(1+2\beta)^2}\left[\frac{\Delta Q_L'^2\delta^2}{(1+\Delta Q_L'^2\delta^2)}\right]. \tag{4.20}$$

The factor $4\beta^2/(1+2\beta^2)$ was taken out of the brackets, meaning that β is assumed to remain constant over the frequency range from f_r to f. This is valid as long as $f_r - f$ is small. The change in the loaded quality due to the change in the frequency is denoted by $\Delta Q'_L$, and

$$\delta = \frac{f^2 - f_r^2}{f^2} \approx 2\frac{f - f_r}{f_r}. \tag{4.21}$$

Substitution of equation (4.21) into equation (4.20) and solving for the small change in f, $\Delta f = f - f_r$, gives

$$f - f_r = \Delta f \approx \frac{f_r}{2}\sqrt{\frac{P_\Delta (1+2\beta)^2}{\Delta Q_L'^2 (P_i 4\beta^2 - P_\Delta (1+2\beta)^2)}}\,. \tag{4.22}$$

The definition of the unloaded quality factor can be used in conjunction with equation (2.25) to derive an equation for the change in loaded quality factor due to the change in the frequency.

$$\Delta Q_L' = \frac{2\pi \Delta f \Delta U}{P_0 + 2P_\Delta} \tag{4.23}$$

where ΔU is the change in stored energy which accompanies a change in the frequency away from the resonant frequency. From equations (4.7), (2.27) and (2.28), P_0 can be shown to be

$$P_0 = \frac{P_i 4\beta}{(1+2\beta)^2}\,. \tag{4.24}$$

This can be substituted into equation (4.23) to give

$$\Delta Q_L' = \frac{2\pi \Delta f \Delta U (1+2\beta)^2}{4P_i\beta + 2P_\Delta (1+2\beta)^2}\,. \tag{4.25}$$

When equation (4.25) is substituted into equation (4.22) it results in

$$\Delta f \approx \sqrt{\frac{f_r \left[4P_i\beta + 2P_\Delta (1+2\beta)^2\right]}{4\pi \Delta U (1+2\beta)}}\sqrt{\frac{P_\Delta}{P_i 4\beta^2 - P_\Delta (1+2\beta)^2}} \tag{4.26}$$

The minimum value of Δf and $\Delta Q'_L$ will occur when P_Δ is the smallest it can be before it becomes undetectable. This will occur when the noise power in the system P_n is equal to P_Δ.

It can be shown [12] that the power of Johnson noise signals in a matched system in thermal equilibrium is given by

$$P_n = kTB\left(1 - \frac{P_{out}}{P_0 + P_{out}}\right). \tag{4.27}$$

In equation (4.27) k is the Boltzman constant, T is the temperature and B is the bandwidth of the measurement. The bandwidth can be reduced with the in built digital filters of the PNA which here are assumed to be ideal.

Substituting equation 2.23 into equation (4.27) results in

$$P_n = kTB\left(\frac{1}{1+\beta}\right) \tag{4.28}$$

The noise power, P_n, can now be equated with P_Δ in equations (4.26) and (4.25) to find the smallest measurable changes in frequency and quality factor respectively. Making these substitutions, along with $P_{out} = \frac{P_i 4\beta^2}{(1+2\beta)^2}$, results in equations (4.29) and (4.30).

$$\Delta f \approx \sqrt{\frac{f_r\left[4P_i\beta + 2kBT(1+2\beta)^2(1+\beta)^{-1}\right]}{4\pi\Delta U(1+2\beta)}}\sqrt{\frac{kBT}{(1+\beta)P_i 4\beta^2 - kBT(1+2\beta)^2}} \tag{4.29}$$

$$\Delta Q_L' = \frac{2\pi\Delta f\Delta U(1+2\beta)^2}{4P_i\beta + 2kBT(1+2\beta)^2(1+\beta)^{-1}} \tag{4.30}$$

In the following estimations the values P_i = 1mW, T = 300K, B = 3kHz and f_r = 1.8GHz were used. The change in energy stored, ΔU, was calculated for a frequency shift off resonance of $f - f_r$. Equations (4.29) and (4.30) were plotted as a function of the coupling coefficient using Mathcad and are shown in figures 4.11a and 4.11b respectively.

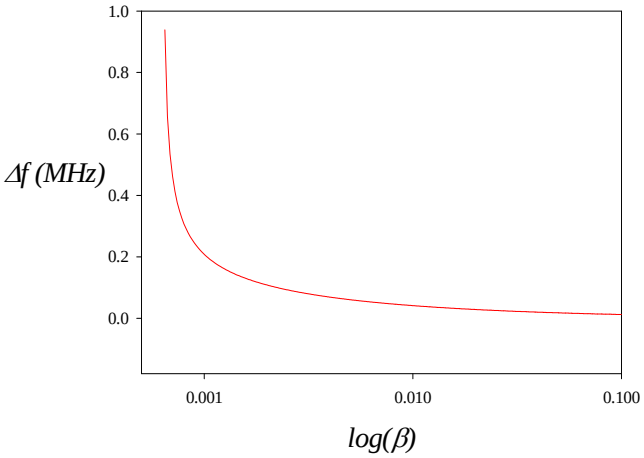

Figure 4.11a shows the smallest measurable change in resonant frequency of the resonator limited by thermal noise in the system as a function of the coupling coefficient.

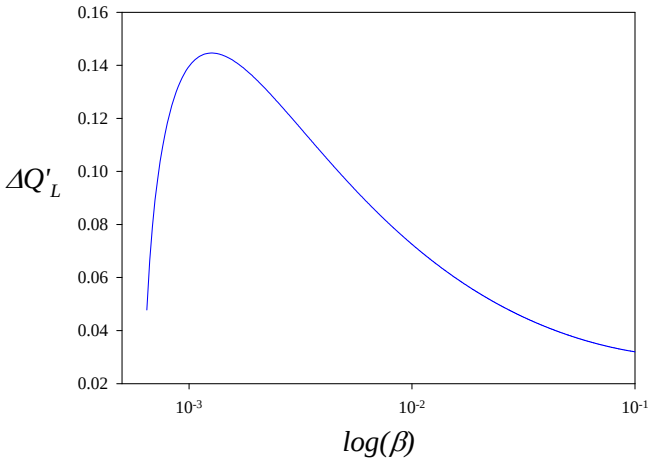

Figure 4.11b shows the smallest measurable change in the loaded quality factor of the resonator limited by thermal noise in the system as a function of the coupling coefficient.

Figures 4.11a and 4.11b show that the smallest measurable changes in frequency and quality factor decrease as the coupling coefficient increases. This is because a larger signal to noise ratio is created with larger coupling.

The coupling wires/loops couple both signal and noise power into the cavity. This is gives rise to the peak in smallest measurable changes in quality factor for extremely low values of coupling coefficient.

The smallest calculated measurable changes in frequency and Q shown in figures 4.11a and 4.11b (for a typical value of coupling $\beta = 0.08$) are 14kHz and $33.5 \cdot 10^{-3}$ respectively. However, vibrations in the measurement system limit the smallest measurable changes in frequency and Q to ~50kHz and ≈5 respectively. When averaging in the PNA is used these values can be reduced to ~10kHz and ≈1. These values correspond to no sample coupled to the resonator.

Although the above derivation was based on an equation for the noise power in a matched network it is applicable to the case of an unmatched network. This is because thermally excited voltage and current waves are independent of impedance matching effects. If this were not true thermally excited voltage waves in circuits would create potential differences in the circuit, and hence work, which would violate the 2nd law of thermodynamics.

4.5. – Modes of the ¼λ Coaxial Open-Ended Resonator

In resonating cavities all modes within the desired frequency range of use must be identified to ensure the correct mode is being used. Also care must be taken to ensure that no extraneous modes are close enough to the mode of interest so as to interfere with that mode when the cavity is loaded with a sample or when the coupling is changed.

This section describes how the modes of the 1/4 λ open ended coaxial cavity were identified by comparing PNA measurements with simulations performed using CST microwave design studio and analytically deduced mode frequencies.

Measurements (using the PNA) were taken of $|S_{21}|$ from 10MHz to 15GHz for different lengths of coupling wires protruding into the cavity. Figure 4.12 shows the experimental setup. This was done to test if the resonant frequency of any modes changed as the coupling wire length was increased.

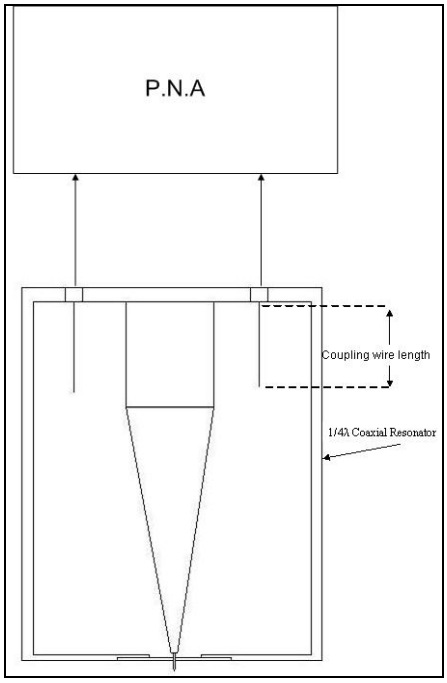

Figure 4.12 Drawing of the experimental setup used to measure the resonant frequencies of modes within the resonator for different lengths of coupling wire.

The frequencies of the resonant modes were compared with those from simulation results using CST Microwave Design Studio. The eigenmode solver was used to find the resonant frequencies from 10MHz to 12GHz. The eigenmode solver does not simulate waves being fed into the cavity in a time or frequency domain, but rather solves for the resonating modes of the cavity only. The simulation model is shown in figure 4.13.

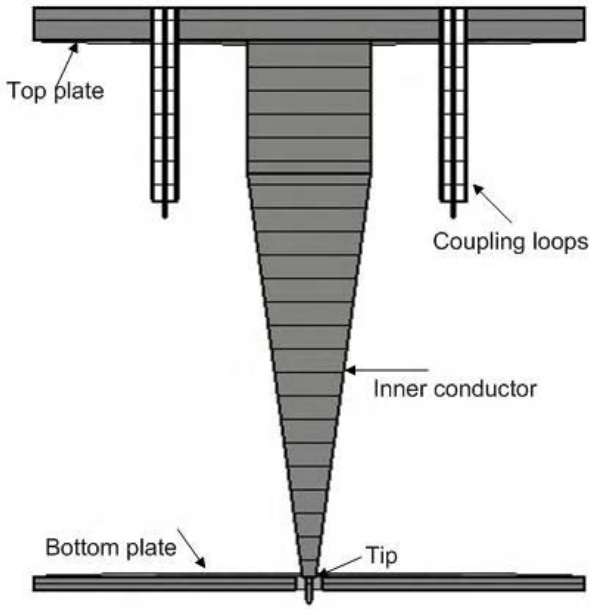

Figure 4.13 Diagram of simulation model used in CST microwave design studio to find the resonant frequency of modes from 0Hz to 12GHz.

Analytical expressions taken from Marcuvitz [13], were used to find the frequencies of the modes from 0 – 12GHz as detailed in section 2.5. The geometry used to calculate the modes is shown in figure 2.2.

Figure 4.14 shows a diagram of the PNA trace from 10MHz to 15GHz for coupling wire lengths of 0mm to 12mm. An arbitrary y-axis was utilised in figure 4.14 so that the traces could be placed on top of one another. This was done to illustrate graphically, that certain peaks do not move.

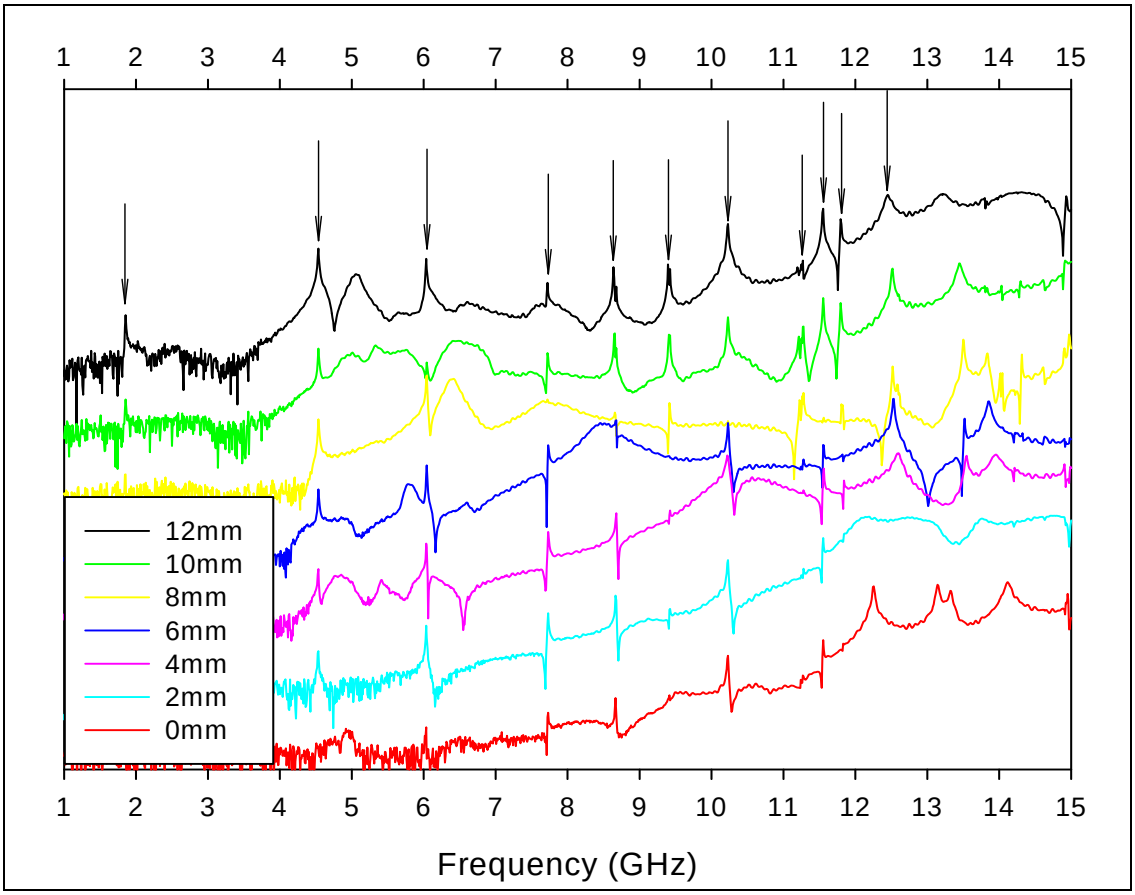

Figure 4.14 Diagram of the several PNA traces of $|S_{21}|$ from 10MHz to 15GHz for several different coupling wire lengths from 0mm to 12mm. The y-axis is arbitrary to allow graphical comparison of the traces.

The arrows in Figure 4.14 show the peaks that did not move in frequency as the coupling wire lengths were increased. Therefore, these modes were resonating within the cavity structure itself rather than around the coupling wires. The coupling wires protruding down into the cavity in between the inner and outer conductor can emulate a coaxial structure enabling modes to resonate along the coupling wire length (coupling wire modes), instead of the cavity length (cavity modes). Hence modes which changed in frequency appreciably as the coupling wires moved into the cavity were coupling wire modes. In this way the cavity modes were differentiated and separated from coupling wire modes (which must be done before measurements can be taken) whilst measuring and cataloguing their frequency.

The use of coupling loops instead of wires would hide the appearance of coupling wire modes in the PNA trace due to the strong excitation of the TEM modes, but their effect may still be substantial during measurements.

In general, more modes are supported by resonators at higher frequencies due to the low wavelength being able to fit many times into the structure. For this reason the identification of modes above 12GHz in cavity under question was not attempted, see figure 4.14.

It should be noted that, in figure 4.14 even though some peaks are not excited for small lengths of coupling wire, their frequencies are still independent of coupling wire length. Therefore these must be cavity modes.

The TEM modes of the cavity were identified by matching the frequencies and field patterns from CST with those calculated and shown in Marcovitz [13].

Figures 4.15a and 4.15b show the electric and magnetic fields of the TEM 1/4 λ mode. The arrows show the direction of the field while the size and colour of the arrows indicates the strength of the field, red being the strongest and green the lowest. The colour and field strength scale has been left off the diagrams as it is misleading due the fixed input power of the simulation. It can be seen from figures 4.15 that the electric and magnetic fields inside the resonator are 90° out of phase in space. The peak amplitudes of the electric and magnetic fields are also out of phase in time.

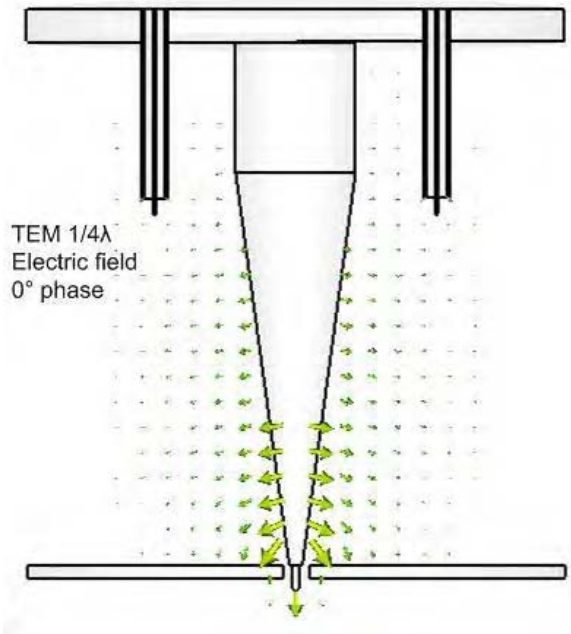

Figure 4.15a CST microwave studio simulation showing electric field for the TEM ¼ λ mode.

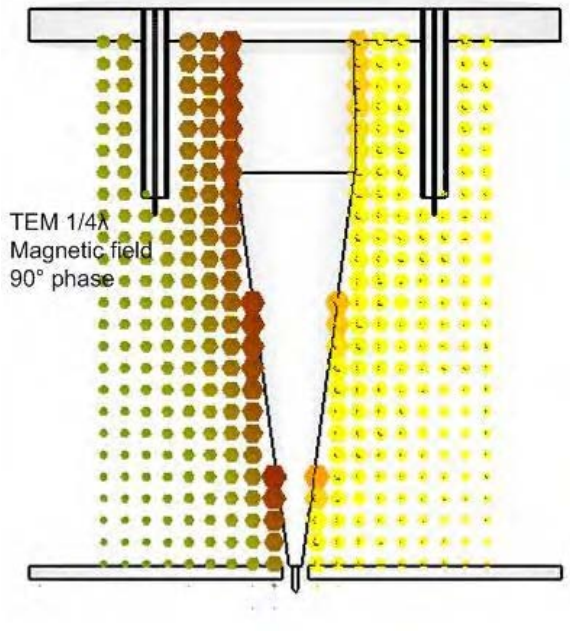

Figure 4.15b CST microwave studio simulation showing magnetic field for the TEM ¼ λ mode.

It can seen from figure 4.15a that an electric field maximum and minimum occur at the open end and closed end respectively. It is also clear from figure 4.15b that a magnetic field maximum occurs at the closed end. At first glance it appears a magnetic field minimum does not occur at the open end as shown in figure 4.15b. However, it must be noted that the open end of the resonator is the very end of the tip and not simply the inner face of the bottom plate. The structure therefore acts a quasi-open ended resonator in that the "closed part" of the open end (the bottom plate) has a non-zero magnetic field strength whereas the "open ended" part of the open end (the small gap where the tip protrudes through the end plate) has a magnetic field minimum.

It can be said that figure 4.15a depicts a quasi-TEM mode because the electric field is bent into the longitudinal direction (a TM mode) by the presence of the end plate. Similarly, the spatial distribution of the wave is not a perfect sinusoid but takes a more distorted form (the wave is "squashed" toward the end). This is due to a combination of the quasi-open end and the tapering of the inner conductor. This is further illustrated in the TEM 3/4λ mode shown in figure 4.16 and 4.16b. The figure also shows the distortion of the positions of the antinodes from exact 1/4, 1/2 and 3/4 length ratios due to the taper and endplate.

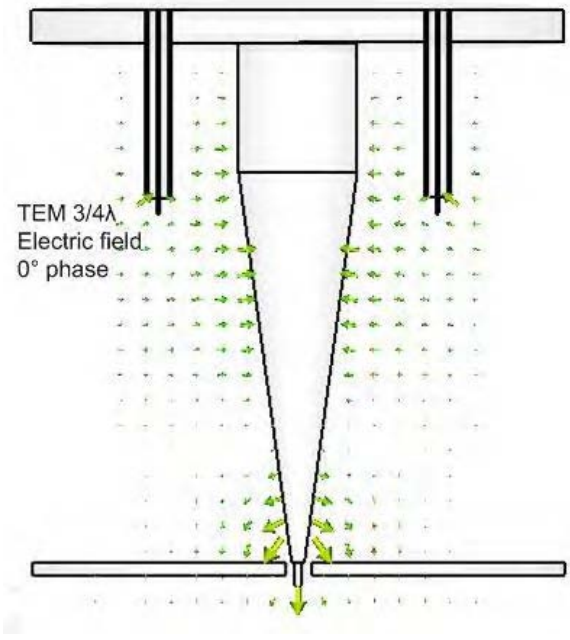

Figure 4.16a CST microwave studio simulation showing electric field for the TEM 3/4 λ mode.

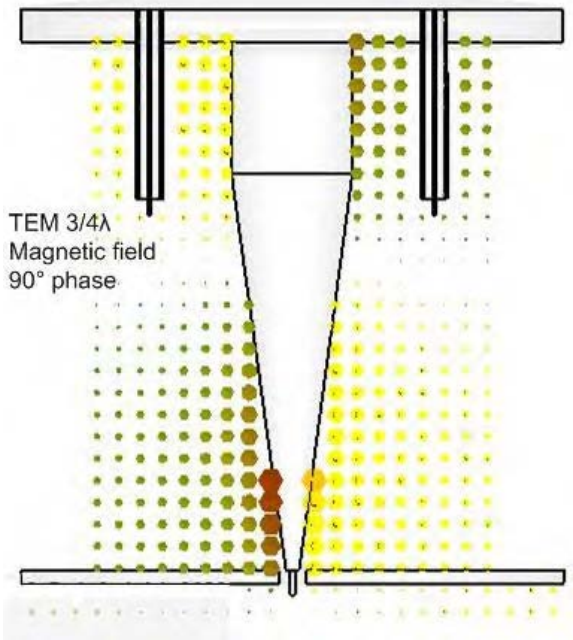

Figure 4.16b CST microwave studio simulation showing magnetic field for the TEM 3/4 λ mode.

Figures 4.17a and 4.17b show the electric and magnetic field patterns for the TE111 mode calculated in CST.

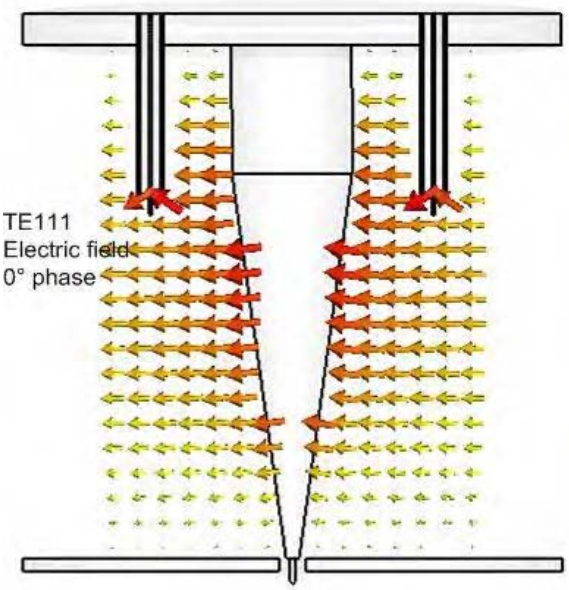

Figure 4.17a CST microwave studio simulation showing electric field for the TE111 mode.

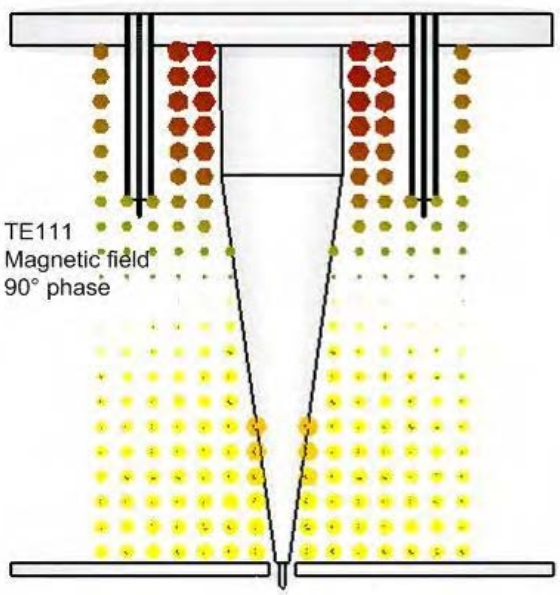

Figure 4.17b CST microwave studio simulation showing magnetic field for the TE111 mode.

It can be seen from figure 4.17a that the TE111 mode is a $1/2\lambda$ mode. Therefore, even though one end is open and the other closed, there is still an electric field minimum at both ends. This shows that boundary conditions are mode dependent and that the TE modes are useless for the characterisation of dielectric materials.

Figure 4.18 shows the electric and magnetic fields for the TM011 mode where an electric field maximum is present at the end of the tip. The TM modes can therefore be used to characterise dielectric samples. It is left to future work to analyse the response of these modes.

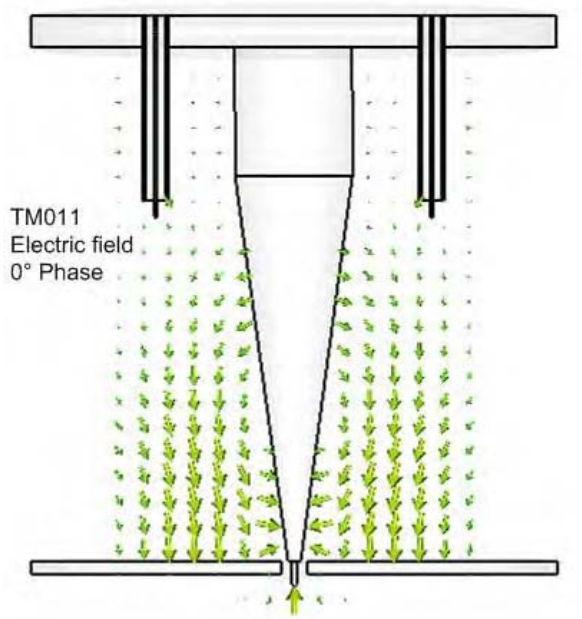

Figure 4.18a CST microwave studio simulation showing electric field for the TM011 mode.

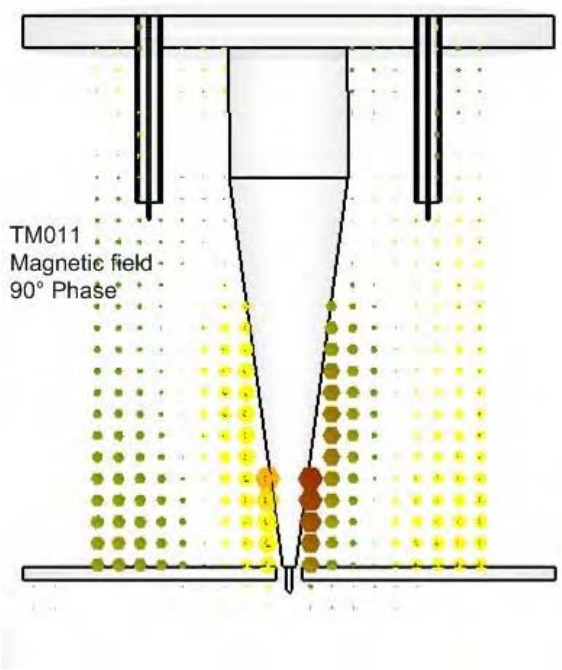

Figure 4.18b CST microwave studio simulation showing magnetic field for the TM011 mode.

After each mode was identified, their frequencies were plotted on a graph of $|S_{21}|$ vs frequency for the resonator as shown in figure 4.19. Figure 4.19 shows the results of the PNA sweep, the CST simulations and the calculated values of frequency of modes.

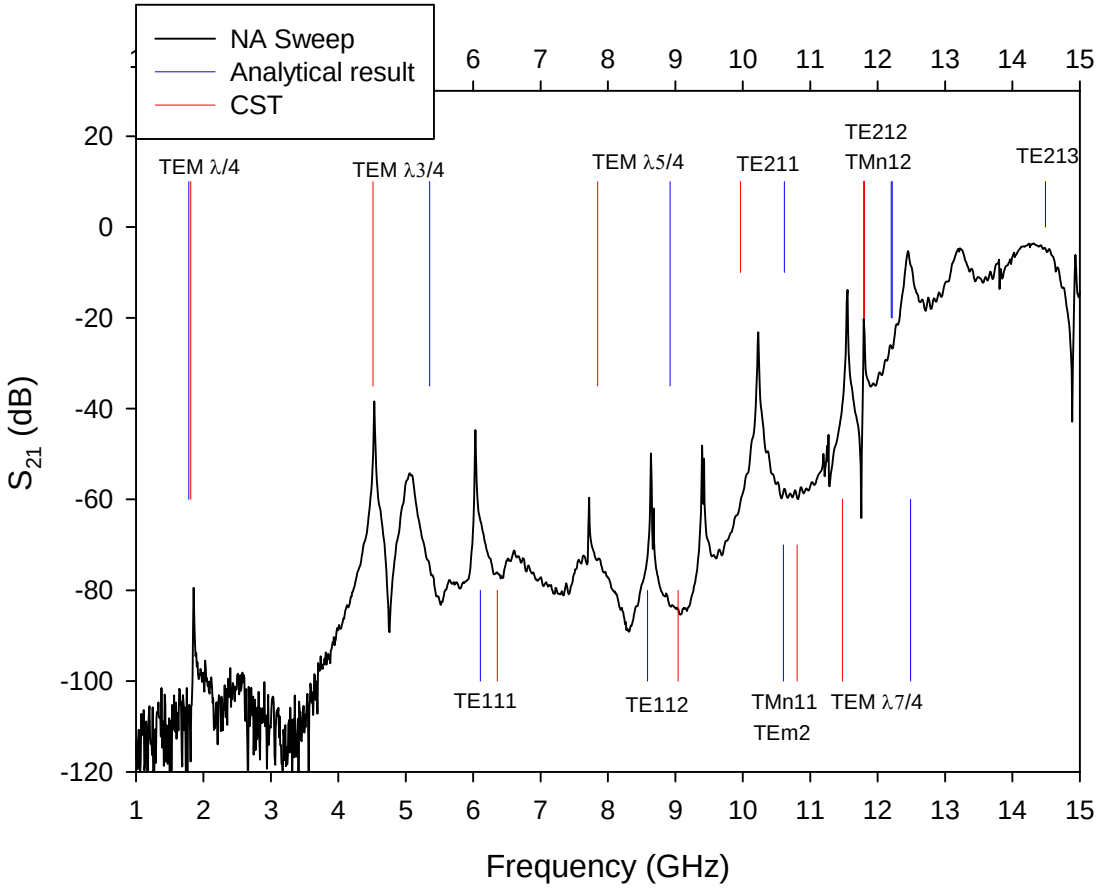

Figure 4.19 Graph showing the resonant modes of the cavity from a PNA sweep from 1GHz to 15GHz. Also marked on the graph are the analytically derived frequencies of various modes (blue) and those from CST (red).

In figure 4.19, it can be seen that there is good agreement between the simulation and experimental results for most of the TEM modes. In this case the largest difference seems to be at the higher order modes of TEM 5/4λ and 7/4λ. This could be that the length of the resonator was simulated incorrectly. A small simulation uncertainty in the length may have a greater effect on higher order modes because of the way the wavelength is forced to fit into the resonator. The same reason could be responsible for the difference between the simulated and experimental results for the TM and TE modes.

For the difference between the analytical and experimental results, the presence of the end plate and tapered inner conductor is likely responsible. For the TEM modes, the presence of an end plate would reduce the resonant frequency due to an extra capacitance. This is consistent as the analytical results for the TEM 3λ/4, 5λ/4 and 7λ/4 modes are all too high.

In conclusion one can identify with some certainty the resonant frequency of TEM modes up to 12GHz. However, only an indication of the resonant frequencies of the TE and TM modes up to 12GHz for the cavity in question can be gained by the process described above.

Further work could include measuring approach curves to distinguish between TE and TM modes.

4.6. – Sources of Noise in the Measurement System and Environmental Effects

Local environmental effects can significantly affect measurements when small length scales and sensitive measurements are involved. Therefore the SNMM, fulfilling both these criteria, requires the temperature, humidity and vibration of the local environment to be controlled when taking measurements.

The laboratory in which the SNMM was used had little temperature or humidity control. Therefore, temperature and humidity often changed while measurements were being taken. This section is concerned with the error associated with that change.

Surrounding air velocity was not considered in this study as no means of measurement existed. However, this may have effected measurements if, for instance, small pieces of metal became attached to the tip and could easily be disturbed due to air flow.

This section also discusses the effect of electrical and mechanical noise of the measurement taking process and results.

4.6.1. – Temperature

To observe the effect of temperature of the resonator, the resonant frequency and unloaded quality factor, f_r and Q_0, were measured for different room temperatures while no sample was present. The results are shown in figure 4.20.

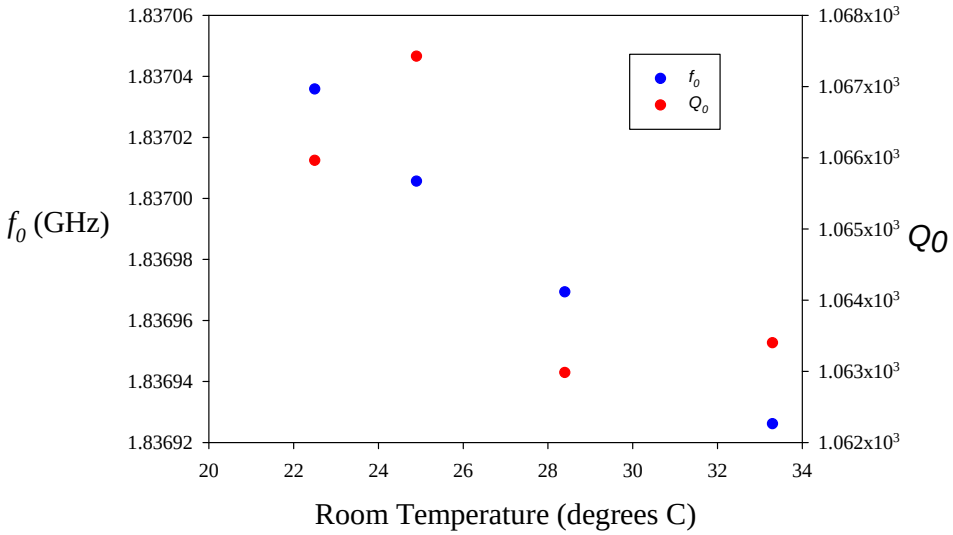

Figure 4.20 Measurements of the resonant frequency of the resonator at different room temperatures.

Figure 4.20 shows a decrease in the resonant frequency as the room temperature is increased. This is expected due to the expansion of the resonators length (the length expands, the wavelength goes up and the frequency goes down).

The equation $\Delta f/f = \Delta l/l = \alpha \Delta T$ can be used to predict the change in resonant frequency for a given change in temperature, where $\Delta f/f$ is the change is frequency over the original frequency, $\Delta l/l$ is the change is length over the original length, α is the linear thermal expansion coefficient for copper ($16.5 \cdot 10^{-6}$ K^{-1}) and ΔT is the change in temperature. Using this equation, the change in frequency from a ten degree change in temperature is 254.6 kHz. However, the observed change in frequency for the same temperature change is ≈109.7 kHz. This discrepancy could be due to the resonator being made of different parts and having different thermal expansion coefficients. However, the main reason for this error is likely that the resonator was at a different temperature than the rest of the room. From the measured frequency shift over a ten degree temperature

change, it can be concluded that if a frequency shift resolution of 10kHz or less than is desired, a room temperature stability of 1 degrees Celsius or less is required.

Figure 4.20 shows no clear, systematic change in Q_0 with temperature. The changes in Q_0 are comparable to the limit in precision of the measurement.

4.6.2 – Humidity

Humidity may affect the resonant frequency, for example if a small water layer was to form over the inner surfaces of the resonator, changing its capacitance. However, this change is expected to be small. Humidity may have a more significant effect when measuring samples as a water layer could be present over the sample surface. This would have a significant effect on the resonant frequency shifts when measuring samples as the tip would be immersed in water which has a relative permittivity of ~80 at GHz frequencies. As the humidity level was difficult to control, measurements on humidly related effects were not made.

If the SNMM were in an environmentally controlled lab the effect of a water layer on different samples could be quantified. To do this, sources of noise (see following section) must be first reduced, then the frequency shift due to each sample could be measured at different humidity levels. However, care must be taken during this process not to alter the tip in any way. This may be impossible for contact mode.

A non-contact operation mode (as discussed in chapter 1) could be used to do this experiment. In this case a tip oscillation is damped by a water layer on the sample surface and hence used to measure a given tip-sample distance equal to the thickness of the water layer. If a correlation between frequency shift and humidity levels were then to be detected using this method, it would indicate a water layer on the sample surface of changing thickness with humidity. This experiment would also show the reliability of non-contact measurements. During such experiments care must be taken to measure the same point on a sample every time because the SNMM is sensitive enough to detect differences in surface permittivity of samples normally

considered homogenous such as microwave substrates. Once this effect has been quantified for different sample materials, the image charge model [9] could be altered to account for this. As the model can account for the effect of a thin film on a substrate, the water layer could be considered as a thin film in the analytical model.

All of this is suggested as future work.

4.6.3 – Electrical and Mechanical Noise

Electrical and mechanical noise in the measurement system hampered measurement taking in some circumstances. The effect of electrical noise could be reduced by the use of the in-built filters of the PNA. The I.F. bandwidth setting can be used to control these filters which filter out unwanted frequencies at each measurement frequency. If another measurement system was used such as a phase lock loop or lock in amplifier, electric noise would become more significant.

Mechanical noise, or vibration, in the measurement system resulted in an oscillation of the tip-sample distance, and hence frequency shift. This effect was a strong function of the average tip-sample distance and sample permittivity. The noise could be damped by pressing the tip onto the sample surface. However, a stronger vibrational noise, or larger permittivity, this would require a larger tip-sample force creating unwanted bending in the tip.

The mechanical noise came from two sources which were building vibration and electrical noise in the positioning system converted to mechanical noise through the piezo cube. The effect of mechanical noise due to electrical noise in the cube positioning system could not be reduced other than using averaging on the PNA Mechanical noise due building vibration was a major problem for samples of relative permittivity above 20 and was due to mechanisms in the building such as heating or air conditioning. This was despite mounting the system on a vibration isolation table. Therefore measurements were performed at night when these systems were off and building noise was at a minimum.

In conclusion, the SNMM needs to be treated the same as any sensitive measurement system such as an AFM and be placed in low vibration location with a controlled environment.

4.7. – Contact and Non-contact Operating Modes

Most types of scanning microscopes can be used in different operating modes. For instance, the AFM can be used in "contact", or a "tapping" mode. Similarly, the SNMM can be used in either a contact or a non-contact mode. In contact mode the tip is held in contact with the sample surface at a constant force, whereas in non-contact mode the tip is held at a fixed distance above the surface of the sample whilst measurements are taken. For non-contact mode, one of the tip-sample distance control methods outlined in chapter 1 must be implemented.

At this stage in the development of the SNMM, the best operating mode for the SNMM is the one which offers the best repeatability.

In this section, the advantages and disadvantages of both operating modes are discussed in terms of their practicality and repeatability. Firstly contact mode is discussed and its effects on measurements are shown.

Contact mode requires that the force between the tip and sample be monitored and kept constant as the tip is scanned over the topographical changes of the sample surface. To do this, a load cell (connected to the PC) was used to measure the force. Within the Labview control program, a feedback loop was setup to control the force during measurement via the z position of the nano-cube stage.

The main disadvantage of contact mode is that any contact between the tip and the sample permanently deforms the tip. The smallest force which could be measured and hence maintained using the load cell was approximately $1 \cdot 10^{-4}$N. It is assumed that as long as the contact force is kept at $\approx 1 \cdot 10^{-4}$N, the tip would not change significantly for subsequent contacts after the initial contact. A freshly made tip would be ~15μm radius at the very end. After contact with a sample

to a force of $1 \cdot 10^{-4}$N, the tip would bend and curl over to an effective diameter of ~30μm. This curling over of the tip end results in an effective shortening of the resonator. This decrease in resonator length would result in an increase in resonant frequency of ~250kHz.

The changing of the tip radius would also change the response of the resonator to a sample. According to the image charge model [9], the change in sample response would be such that with a 15μm radius tip, a sample of YSZ (ε_r = 28.14) would give the same frequency shift as a sample of MgO (ε_r = 9.78) with a tip of ~30μm. These two cases correspond to a frequency shift of ~10MHz. Therefore, although the resonant frequency is increased by a bending of the tip, the decrease in resonant frequency due to the presence of a sample is much larger.

Once the tip is pressed on to the sample with a force greater than the one previously used, a recalibration is necessary. To quantify this recalibration, measurements of $\Delta f_r/f_r$ for two tip-sample forces of 0.1mN and 50mN were taken on MgO and YSZ samples. Measurements were taken using the TEM $\lambda/4$ mode at ≈1.8GHz.

The frequency shifts are plotted against the function, $H(\varepsilon)$, from equation (3.8). A straight line was plotted through the points, including the origin, whose gradient is then the calibration constant, A. This was repeated for the two forces. The results are shown in figure 4.21.

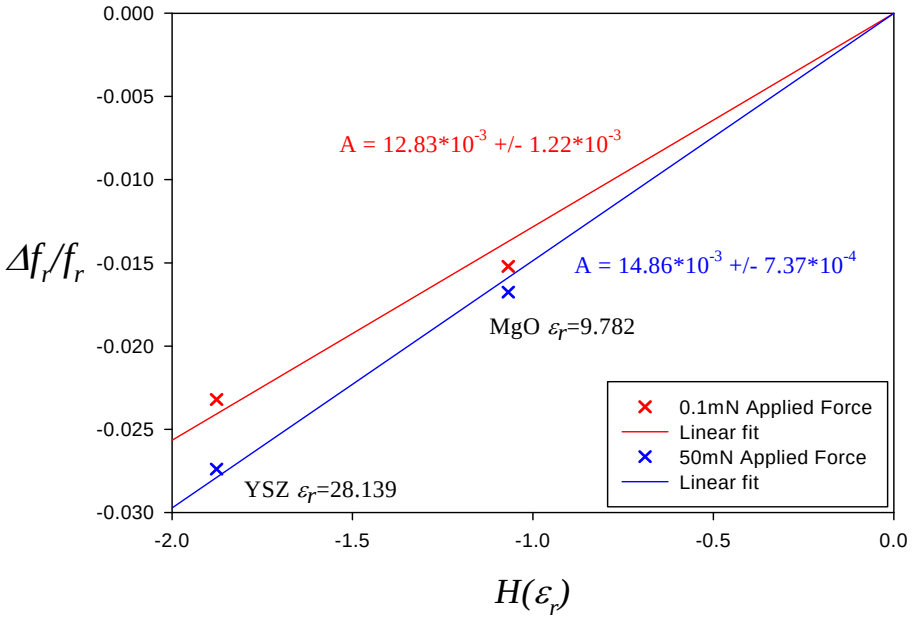

Fig. 4.21 Graph of $\Delta f_r/f_r$ vs $H(\varepsilon)$ plotted using equation (3.8) for tip-sample forces of 0.1mN and 50mN.

In each case, the uncertainty in the value of A was computed by taking the predicted values of $\Delta f_r/f_r$ (by using the constant A) and computing the standard deviation between them and the actual measured values of $\Delta f_r/f_r$.

Figure 4.21 shows that the larger the applied force the greater the frequency shifts and hence gradient, A. The larger gradient produced by a larger tip-sample force is likely due to an increased effective tip radius due to bending. This effect is equivalent to an increased capacitance between the tip and sample creating a larger frequency shift. For the YSZ sample the frequency changed by 1.01MHz when the force was increased from 0.1mN to 50mN. However, for MgO it changed by 2.88MHz. This was because the MgO was measured first, creating a permanent deformation of the tip.

The data in figure 4.21 above shows that the assumption that the tip does not change, after an initial contact, as long as no greater force is applied is correct. This is indicated by the fact that the two contact force measurements show approximately the same percentage uncertainty.

Once more samples became available, more measurements were made to determine if one sample could be mistaken for another. The tip was brought into contact with MgO, YSZ, Sapphire (Al_2O_3) and $LaAlO_3$ samples. For each sample, the frequency shift was measured as the contact force was increased from zero to ≈50mN. The order in which the samples were measured was MgO, YSZ, Sapphire and then $LaAlO_3$. The order is significant because the most bending of the tip occurs during the initial measurement.

Figure 4.22 shows the resonant frequency of the resonator vs. the applied tip to sample force for the aforementioned samples. Figure 4.22 shows that for any applied force from zero to 50mN the SNMM can always distinguish between MgO, YSZ, Sapphire and $LaAlO_3$. This is partly due to the fact that the largest deformation took place whilst the first sample (MgO) was being measured. After this the tip did not deform significantly further.

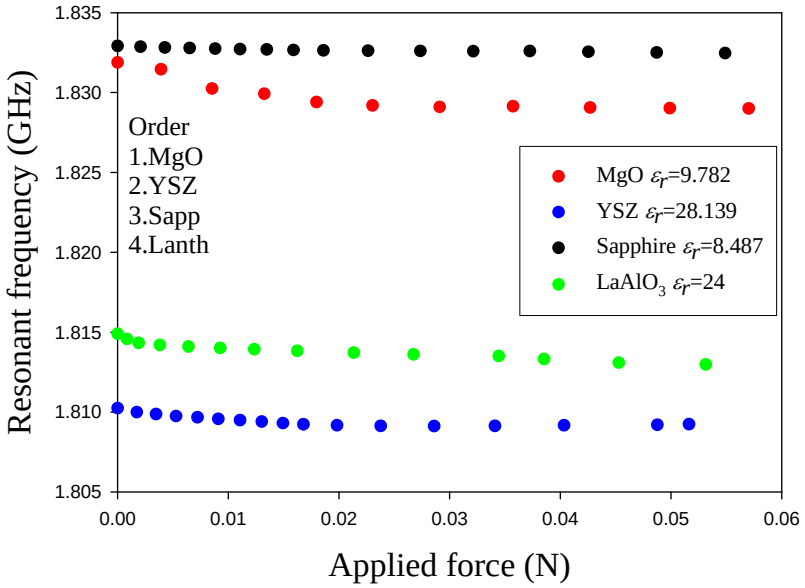

Fig. 4.22 Graph of f_0 vs applied force for samples of MgO, YSZ, Al_2O_3 and $LaAlO_3$. The order in which the measurements were made is shown on the graph.

Figure 4.23 shows the change in resonant frequency of the resonator as the force was increased.

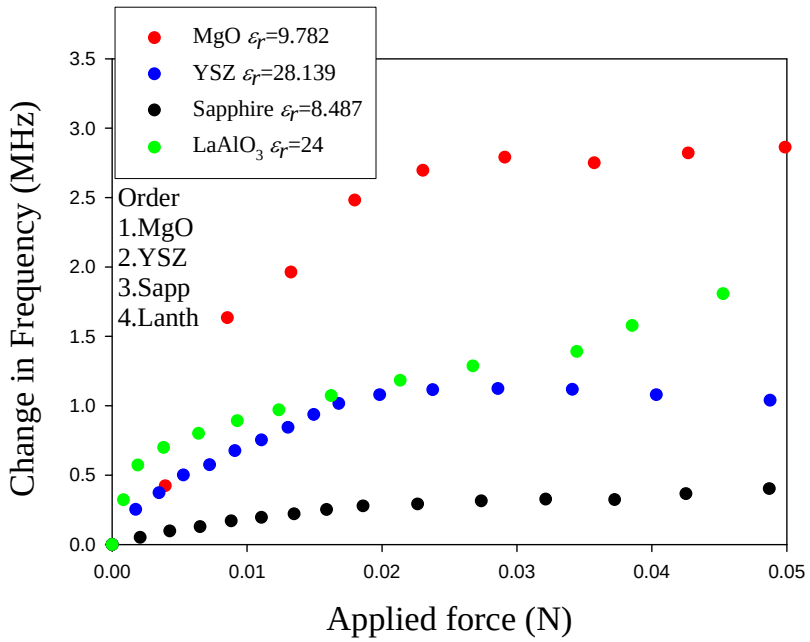

Fig. 4.23 Graph showing change in f_0 vs applied force for samples of MgO, YSZ, Sapphire and $LalO_3$. The order in which the measurements were made is shown on the graph.

It can be seen from figure 4.23 that a large change in frequency occurred for the first sample which was measured. A subsequent measurement of a sample of similar permittivity (Sapphire) yielded a much smaller change indicating inelastic deformation of the tip had occurred.

However, it is apparent that the tip was still changing when a contact force was applied to the last sample, $LaAlO_3$. This indicates some elastic deformation of the tip was also occurring.

A practical difficulty is that of the manual approach to the surface. One never knows exactly how far one is from the sample surface and hence if one moves closer with too much of a large step, it is possible to make contact with sample surface with a force larger than $\approx 1 \cdot 10^{-4}$N. This is a major disadvantage of not having a tip-sample distance control method. Future work should extend the Labview control program to make an automated tip to sample approach, as in the case of the AFM. This program would help protect the tip and could also be used in the future when non-contact mode is implemented.

Non-contact mode can be implemented in several ways which were detailed in chapter 1. The practical advantages and disadvantages depend on the method used, however, all may suffer from a water layer of unknown thickness on the sample surface. In general, the advantage of non-contact mode is that it eliminates most of the problems of tip deformation from contact mode. Some implementations of non-contact mode involve connecting a crystal tuning fork to the tip (see chapter 1). Such a large object in the vicinity of the tip, and the extra length of the tip that is required, may invalidate the approximations of the image charge model (see section 3.4).

Another disadvantage of non-contact mode is that the tip-sample distance must be controlled with increasing accuracy for increasing permittivity. This is because a sample of larger permittivity will cause a larger frequency shift for a given change in tip-sample distance. For instance, according to the image charge model a change in the tip to sample distance from 0μm to 0.5μm would cause a frequency shift of 2.8MHz above an MgO sample, whereas it would create a 6.5MHz shift above a sample of YSZ.

In conclusion, due to the relatively large electric field at the tip of the SNMM it is extremely sensitive to any change in the environment around the tip or the tip itself. The tip must always be

kept the same so that changes in the resonant frequency of the resonator can be attributed to changes in a sample underneath the tip, rather than the tip itself.

It is not possible to determine the uncertainty in permittivity measurements that would result from a given error in applied tip-sample force as any force would result in some inelastic deformation of the tip requiring a recalibration.

4.8. – Measurement reproducibility

Measurement reproducibility is an important attribute for a quantitative measurement system. Factors which could affect the measurement reproducibility of the system have already been discussed, such as different water layers on samples, local temperature variations and vibrational noise.

In addition, care must be taken to ensure the coupling does not change between measurements. This can be done by using a secure mechanism and not touching it between measurements.

In any study of measurement reproducibility a non-contact mode must be implemented as tip bending cannot be avoided in contact mode.

Chapter 4 Bibliography

[1] D. M. Pozar. *Microwave Engineering*, John Wiley and Sons, 3rd Edition, New York, 1998.

[2] National Physical laboratory, *A Guide to the Characterisation of Dielectric Materials at RF and Microwave Frequencies*, The Institute of Measurement and Control, 2003.

[3] L.G. Parratt, "Probability and Experimental Errors in Science", *Soc. Indus. App. Math.* vol. 4, pp. 163, 1962.

[4] T. Nishikawa, K. Wakino, H. Tanaka, and Y. Ishikawa, "Precise measurment method for complex permitiviity of microwave substrate," *CPEM '88 Digest.*, pp. 155, 1988.

[5] A. C. Lynch. “Relationship between permittivity and loss tangent. *Proc. IEE*, vol. 118, pp. 244, 1971.

[6] Y. Guan and Y. Nikawa, “Measurement of temperature dependent complex permittivity for materials using cylindrical resonator under microwave irradiation, *Elec. Comms. Jap.,* vol. J89-C, pp. 1032, 2007.

[7] G. P. Pells, R. Heidinger, A. Ibarra-Sanchez, H. Ohno and R. H. Goulding, “An intercomparison of techniques for measuring dielectric permittivity and loss over a wide frequency range”, *Journ. Nuc. Mat.* vol. 194, pp. 535, 1992.

[8] J. K. A. Everard, “A review of low noise oscillators, theory and design”, *IEEE Int. Freq. Contrl. Symp.*, pp.909, 1997.

[9] C. Gao, and X.-D. Xiang, “Quantitative microwave near-field microscopy of dielectric properties”, *Rev. Sci. Instrum.*, vol. 69, pp. 3846, 1998.

[10] H. Nyquist, “Thermal Agitation of Electric Charge in Conductors”, *Phys. Rev.* vol. 32, pp. 110, 1928.

[11] M. J. Lancaster, *Passive Microwave Device Applications of High Temperature Superconductors*. Cambridge University Press. UK, 1997.

[12] P. F. Panter, *Communication System Design*, McGraw-Hill, New York, 1972.

[13] N. Marcuvitz. *Waveguide Handbook*. McGraw-Hill, 2nd Edition, New-York, 1951.

Chapter 5 – Quantitative Dielectric Characterisation

5.1. – Introduction

Quantitative measurement results are essential to the advancement of science. To acquire quantitative results, calibrations of measurement instruments are necessary. Therefore, quantitative analysis of calibration routines and measurement instruments is also necessary in order for those routines and instruments to be validated as reliable. Uncertainties in calibration routines may be carried over into final results and therefore must be quantified in any system in order to define the validity of results. This also allows for sources of uncertainty to be identified and improvements to be made to measurement techniques. It is important for the validation of the SNMM as a reliable dielectric characterisation tool that any sources of uncertainty in the measurement process be identified and quantified.

As the image charge model is the most widely used analytical model for calibration of the SNMM it is quantitatively evaluated for the first time in this section in terms of how well it fits to experimental results. Therefore, the work detailed in this section seeks to quantify uncertainties imposed on final results from the calibration using the image charge model, when applied to both bulk and thin film dielectric samples. This is done by first evaluating the model for the prediction of bulk sample response, the effects of tip length and thin film response.

5.2. – Evaluation of Image Charge Model for Bulk Samples

This section describes and discusses the measurements taken on standard bulk dielectric samples to evaluate the effect of different tip lengths in terms of the image charge model. This work was also used to calibrate the SNMM. The image charge model is evaluated in terms of the uncertainties in the calibration constants which quantifies how well the model can fit to the measurement data.

In approximating the tip as a sphere the image charge model deems the most important length scale to be the radius of the end of the tip (the sphere) and therefore neglects any coupling of the tip shaft to the sample. This approximation is tested here through measurements on samples of known relative permittivity using different length tips. This type of study has not been reported previously.

The validity of calibration of measurements of the real part of permittivity using the image charge model has been independently verified numerically [1] but the uncertainties propagating through the model have not been analysed previously.

Problems with the calibration of measurements of loss tangent using the image charge model have been highlighted by various researchers [1, 2, 3, 4]. In each reference the inability to fit loss measurements to the response predicted by the image charge model [5] is attributed to resonator conductor losses. These become significant for large permittivity samples, which require extra charge redistributed to the tip for it to maintain its equipotential surface.

5.2.1. – Image Charge Model Calibration of Frequency shifts and the Effect of Tip Length

The experimental setup used was that shown in figure 1.2. The standard samples used for the calibration were the MgO, $NdGaO_3$, YSZ, peek and macor samples described in section 4.3.2.

The tip of the resonator was brought into contact with each sample with a force of 0.1mN and the resonant frequency and quality factor shifts were calculated (using the method described in section 4.3.1) and recorded. This was repeated for the TEM $\lambda/4$, TEM $3\lambda/4$ and TEM $5\lambda/4$ resonant modes. Each measurement was repeated three times in order to generate uncertainty bars.

The process was completed for a tip length of 2mm. The tip was then shortened to 1mm and the measurements repeated. The tip length is the length of the tip which protrudes beyond the end-plate of the resonator.

The uncertainties in the values of *A* were calculated using the method described in section 4.7.

Figures 5.1a, 5.1b and 5.1c show $\Delta f_r/f_r$ vs $H(\varepsilon_r)$ for the first three TEM modes with the computed values of *A* and their uncertainties taken using a 2mm tip. Also shown in figures 5.1a, 5.1b and 5.1c are the unloaded resonant frequency of the mode and the resonant frequency at which each sample was measured.

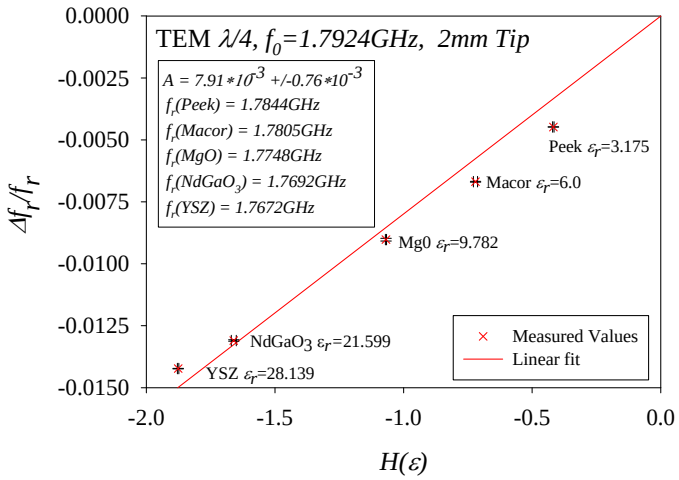

Fig. 5.1a Graph of $\Delta f_r/f_r$ vs $H(\varepsilon_r)$ showing the calibration constant, *A*, for the TEM λ/4 mode using a 2mm tip. The graph also shows the unloaded resonant frequency of the mode and the resonant frequency at which each sample was measured.

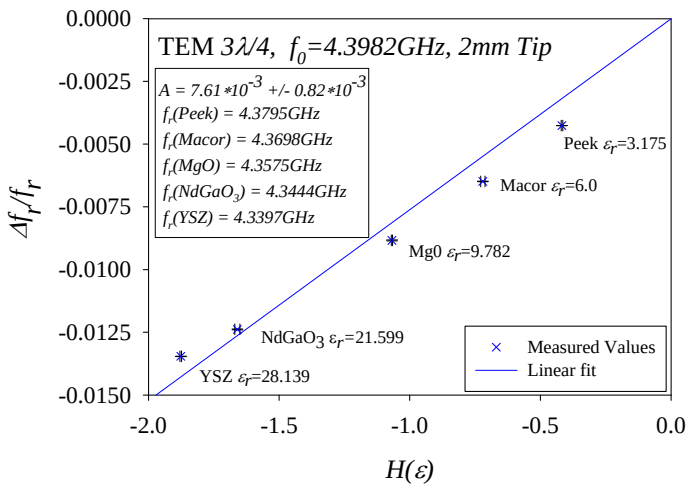

Fig. 5.1b Graph of $\Delta f_r/f_r$ vs $H(\varepsilon_r)$ showing the calibration constant, *A*, for the TEM 3λ/4 mode using a 2mm tip. The graph also shows the unloaded resonant frequency of the mode and the resonant frequency at which each sample was measured.

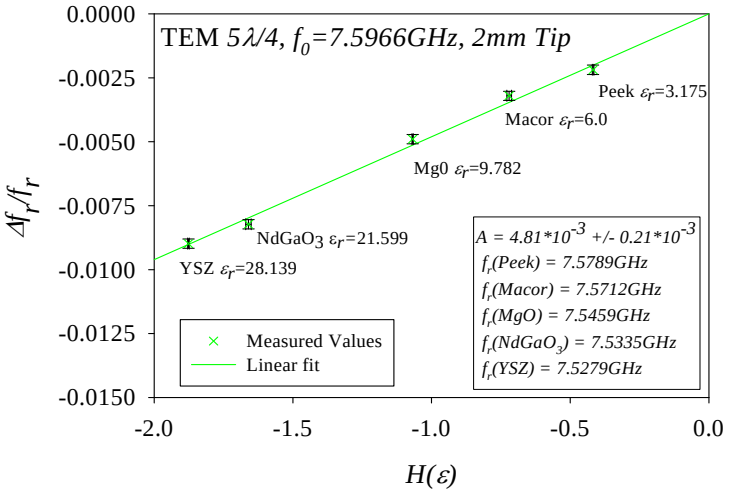

Fig. 5.1c Graph of $\Delta f_r/f_r$ vs $H(\varepsilon_r)$ showing the calibration constant, A, for theTEM 5λ/4 mode using a 2mm tip. The graph also shows the unloaded resonant frequency of the mode and the resonant frequency at which each sample was measured.

Figures 5.2a, 5.2b and 5.2c show $\Delta f_r/f_r$ vs $H(\varepsilon_r)$ for the first three TEM modes with the computed values of A and their uncertainties taken using a 1mm tip. Figures 5.2a, 5.2b and 5.2c also show the unloaded resonant frequency of the mode and the resonant frequency at which each sample was measured.

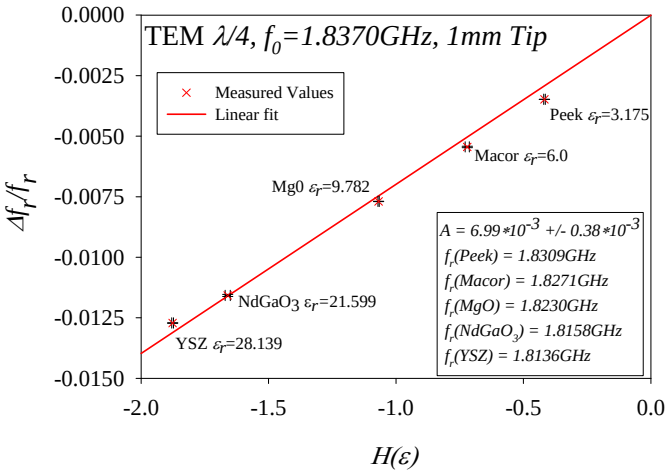

Fig. 5.2a Graph of $\Delta f_r/f_r$ vs $H(\varepsilon_r)$ showing the calibration constant, A, for the TEM λ/4 mode using a 1mm tip. The graph also shows the unloaded resonant frequency of the mode and the resonant frequency at which each sample was measured.

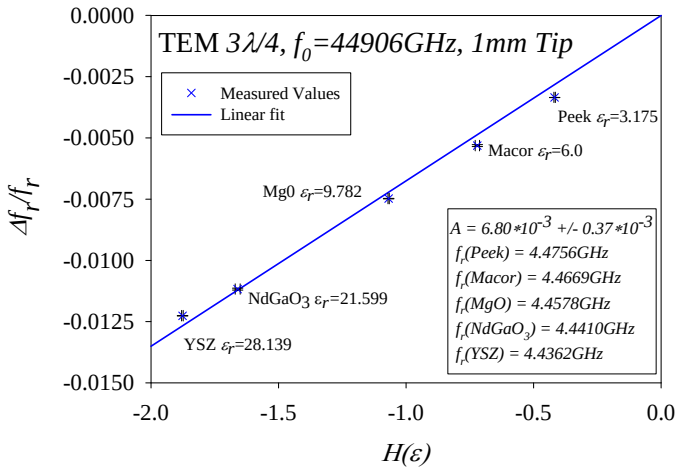

Fig. 5.2b Graph of $\Delta f_r/f_r$ vs $H(\varepsilon_r)$ showing the calibration constant, A, for the TEM 3λ/4 mode using a 1mm tip. The graph also shows the unloaded resonant frequency of the mode and the resonant frequency at which each sample was measured.

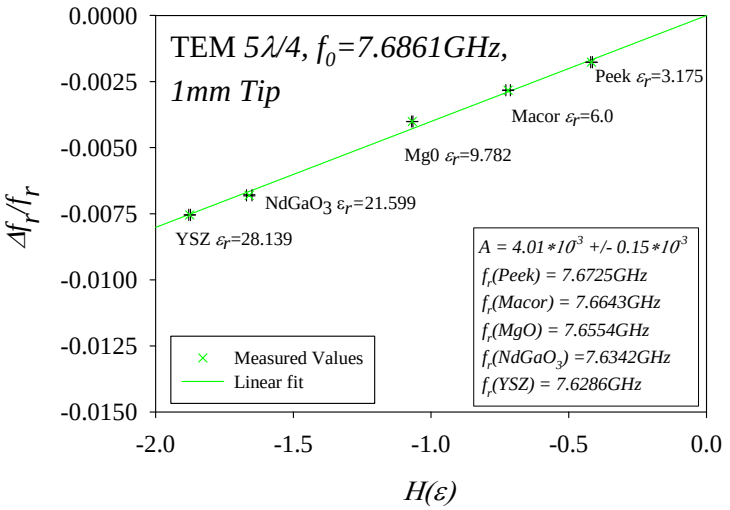

Fig. 5.2c Graph of $\Delta f_r/f_r$ vs $H(\varepsilon_r)$ showing the calibration constant, A, for the TEM 5λ/4 mode using a 1mm tip. The graph also shows the unloaded resonant frequency of the mode and the resonant frequency at which each sample was measured.

It can be seen from comparing the results in figures 5.1a to 5.1c with figures 5.2a to 5.2c that the quality of the linear fit to the data improves as the tip length is reduced. Thus the uncertainty in the calibration constant, A, reduces as the tip length is reduced. For the TEM λ/4 and 3λ/4 modes, the uncertainty in A is approximately 10% for the 2mm tip and 5% for the 1mm tip. However, for the TEM 5λ/4 mode, the uncertainty reduces from approximately 5% for the 2mm tip to 2.5% for the 1mm tip. Reducing the tip length below 1mm was not accomplished due to the difficulty in cutting a tungsten wire for the tip to less than 1mm accuracy.

This reduction in uncertainties when fitting to the image charge model can be attributed to the fact that as the tip shortens it reduces more to the approximation of the model of a charged sphere for the tip. However, in the original publications [5] and the literature since then [2] it was assumed this approximation held if only the radius of the end of the tip was much less than the sample thickness. Figures 5.1a to 5.2c show that in order to obtain a good fit to the model, the tip length must also be considered.

The tip used had an approximately 15μm radius end whilst the thickness of the $NdGaO_3$ and YSZ samples was 500μm. Therefore the tip radius was only approximately thirty times smaller than these sample thicknesses rather than much smaller (usually, much smaller would mean at least a hundred times smaller). This requirement is to ensure the tip does not couple significantly to

anything which is under the sample, or "see through" the sample. However, this depends on the sample. The electric field from the tip would penetrate deeper into a sample of low permittivity than it would for a high permittivity sample.

To ensure the tip did not couple significantly to anything under the sample, extra pieces of macor were placed under each of the samples used in the above experiment and the frequency shifts compared to those shown in figures 5.1a to 5.2c. No difference outside the size of the uncertainty bars of the frequency shifts was seen. Therefore the tip did not couple significantly to anything under the samples and the uncertainty in the fit of the model to the results in figures 5.1 and 5.2 is not due to this effect.

The figures 5.1a, 5.1b, 5.2a and 5.2b also show that the low ε_r samples fall below the straight line fit whilst the high ε_r samples fall above the line. This appears to be evidence of a systematic uncertainty in the image charge model when the tip is "long".

Although A is termed and treated as a constant in reference [2], its definition in the same paper appears with wavelength dependence as shown in equation 3.10. To determine if this frequency dependence was responsible for the deviation of the data from the model seen in figures 5.1a, 5.1b, 5.2a and 5.2b, two separate calibration constants were determined for the Peek and YSZ samples using the definition of A (equation 3.10), which differed by 3%. However, if two values of the calibration constant for these samples were found using equation 3.8 (using measured values of $\Delta f_r/f_r$ and $H(\varepsilon_r)$) then the values of A differed by 20%. Therefore, although, the curvature of the data seen in figures 5.1a, 5.1b, 5.2a and 5.2b is consistent with the frequency dependence of A shown in equation (3.10), the extent of the variation in the data is larger than expected from the equation. The variation is therefore most likely due to the length of the tip.

In all the above cases above the wavelength is at least (in the case of the TEM λ/4 mode) 160 times greater than the length tip length (cavity length is 40mm and tip length is 1mm). Therefore, the assumption that the tip emits negligible far field components is upheld and it can be assumed this is not responsible for the effect discussed above. However, this has not previously been shown to be true and is a needed area of future work.

However, the addition of a non zero y-intercept into equation (3.8) would reduce the uncertainty in fitting to the model from 5% to 1.6% as shown in figure 5.3.

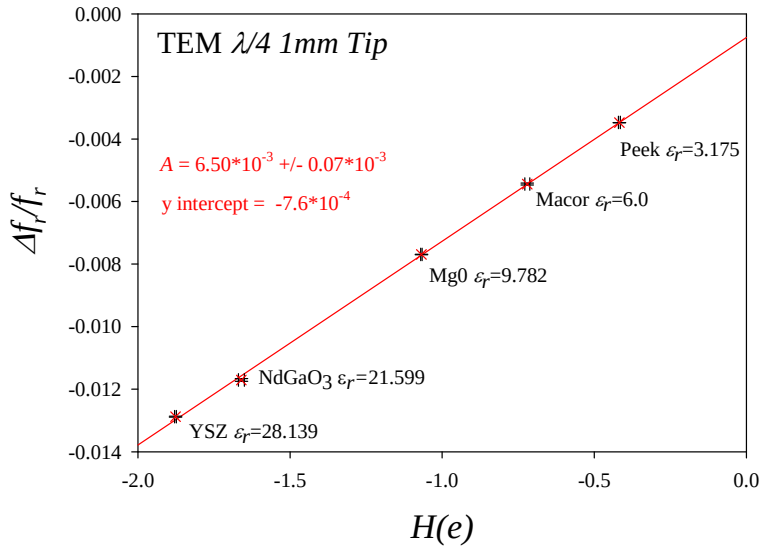

Fig. 5.3 Graph of $\Delta f_r/f_r$ vs $H(\varepsilon_r)+X$, where X is a constant, showing that the fit to the model for "long" tips can be improved by the addition of a non-zero y-intercept.

If the y-intercept of equation (3.8) was allowed to be non-zero, a decreasing tip length would result in a decreasing y-intercept. Therefore, from figures 5.1a to 5.2c it is clear to see that the shaft of the tip is producing an uncertainty in the fit to the model, and from figures 5.1a to 5.3 it is clear that the uncertainty is a constant proportional to tip length.

Measurements of $\Delta f_r/f_r$ and $H(\varepsilon_r)$, for the TEM 5/4λ mode are shown for a 2mm tip and 1 mm tip in figures 5.1c and 5.2c respectively. The TEM 5/4λ mode shows a smaller value of A than the TEM 1/4λ and TEM 3/4λ modes. When comparing the gradients of the graphs 5.2a to 5.2c it should be noted that the frequency shifts, Δf_r, of the TEM 3/4λ and 5/4λ modes are similar while the Δf_r measured from the TEM 1/4λ mode are the smallest. When the quantity, Δf_r, for each mode is divided by its unloaded resonant frequency, f_r, then it becomes similar for the TEM 1/4λ and TEM 3/4λ modes while the TEM 5λ/4 mode gives the smallest values of $\Delta f_r/f_r$. Therefore the real question to ask when considering the differences in A for each mode is, why do some modes give larger frequency shifts than others for the same material. More work needs to be done to answer this question and investigate this effect. However, it was shown in [6] that the near field of a short dipole antenna reduces with distance more quickly for higher frequencies. If this can

be applied to the tip of the SNMM it would mean that higher frequency modes give smaller frequency shifts. However the opposite of this is seen. Therefore this effect could be due to the non linear way in which the electric field standing wave in the resonator is deformed differently for each mode due to the tapered inner conductor and end plate (see section 4.5).

As described in section 4.3.2, it is possible for resonances to be excited in the YSZ and $NdGaO_3$ samples when probing with the TEM 3/4λ mode, and in the YSZ and MgO samples when using the TEM 5/4λ mode. However, it can be seen from the graphs that if these data points were taken out, the uncertainties would not change significantly and the effects mentioned above would still apply. It is difficult to see if these sample resonant modes were being excited from the measurements shown above. However, the similar uncertainty in the fit to the model for the TEM 1/4λ and 3/4λ modes suggests that they were not. Therefore, the smaller uncertainty in fitting to the model for the TEM 5/4λ mode, also suggests that no sample modes were excited during those measurements either. However, it may be that these modes cannot be excited within the sample as the near field is a non-propagating wave.

In conclusion, the uncertainty in the calibration constant, *A*, is reduced for a shorter tip indicating that it is simply caused by the deviation of the real world case away from the approximations of the image charge model.

The uncertainties in the calibration constants in figures 5.1a to 5.2c are small enough for the model to be used to characterise bulk samples confidently.

5.2.2. – Image Charge Model Calibration of Loss Measurements

During the measurements described in the preceding section the unloaded quality factor was calculated.

In order to calibrate the SNMM for loss measurements, equation (3.9) from the image charge model was considered.

$$\Delta\left(\frac{1}{Q_0}\right)=\Delta\left(\frac{1}{Q_0}-\frac{1}{Q_0'}\right)=-\frac{\Delta f_r}{f_r}\cdot\left[B+\tan\delta\right] \quad . \tag{3.9}$$

Equation (3.9) implies a linear dependence of $\Delta(1/Q_0)$ on $\Delta f_r/f_r$. However, it has been reported that the relationship is non linear [4]. Several other similar equations for $\Delta(1/Q_0)$ involving more constants have been proposed [5, 1], but all of these exhibit the same problem of the non linearity described above. In [2] it is stated clearly that the calibration constant, *B* exhibits strong frequency and permittivity dependence. Yet this statement is not reflected in the proposed equations of the paper. A further function was proposed to describe the system response to loss measurements [4] where a permittivity dependent *B* term was considered and extra quadratic frequency shift terms were added in an attempt to account for the observed quadratic response. However, this did not describe the response fully.

According to equation (3.9) when $(1/\Delta Q_0)/\Delta f_r/f_r$ is plotted vs $\tan\delta$ the resulting graph should show a straight line with a negative gradient of -1, and a *y* intercept of -*B*. $(1/\Delta Q_0)/\Delta f/f$ is plotted vs $\tan\delta$ in figure 5.4 for the TEM $\lambda/4$ mode.

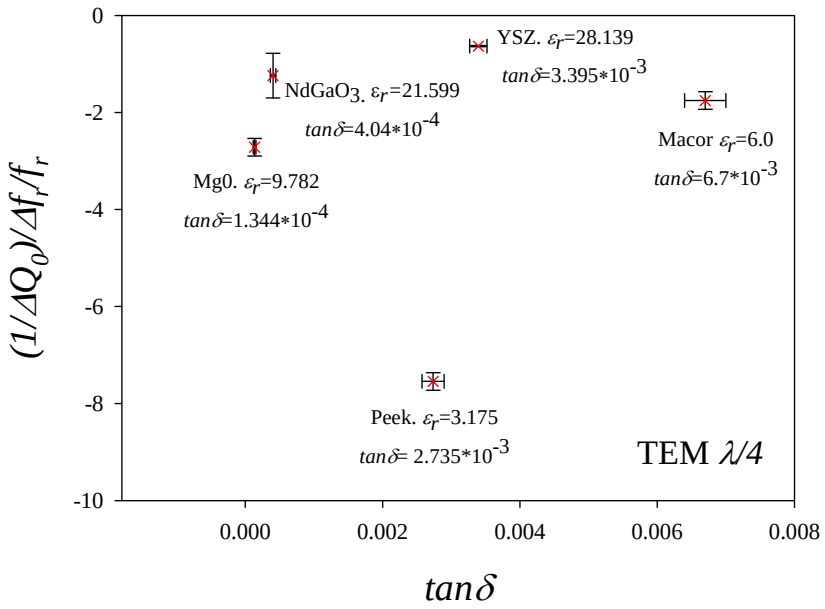

Fig. 5.4 Graph of $(1/\Delta Q_0)/(\Delta f_r/f_r)$ vs $\tan\delta$ for calibration of loss measurements from equation (3.9).

Figure 5.4 clearly does not indicate a straight line should be fitted. Therefore it is concluded that the relationship described in equation (3.9) does not apply to this system.

However, although measurements of loss cannot be calibrated with confidence, it is worth noting that if ΔQ_0 is plotted vs ln($tan\delta$), a straight line can be drawn through the data points of samples which were characterised using the same technique (the split-post resonator). In this case equation (5.1) was used.

$$\Delta Q_0 = D + D' \ln(\tan\delta) \tag{5.1}$$

where D and D' are constants. The measured values of ΔQ_0 are plotted vs ln($tan\delta$) in figure 5.5.

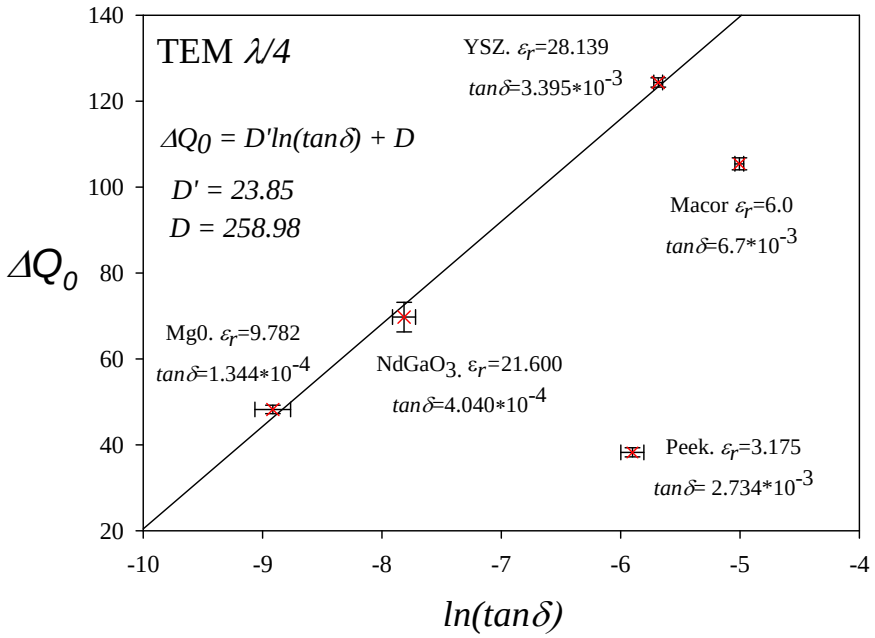

Fig. 5.5 Graph of ΔQ_0 vs *ln(tanδ)* with a straight line plotted the data points of samples measured previously using the split post resonator technique.

Figure 5.5 shows a good fit of the data to equation (5.1) for the samples characterised using the split-post resonator.

Figure 5.5 cannot be repeated for the TEM 3/4λ and 5/4λ modes. This lack of complete data, and of a theoretical underpinning for equation (5.1), leads to the conclusion that currently the SNMM cannot be calibrated for measurements of loss yet.

5.3. – Evaluation of Image Charge Model for Thin Films

The ever decreasing size and increasing flexibility demanded of microwave devices requires quicker, more reliable and more accurate deposition and characterisation techniques for thin films.

Thin films have different material properties than those of bulk samples made from the same materials. The differences may be due to thickness effects and/or differences in structure and composition arising from the deposition process. The study of these differences is an important area in materials research.
The advantages of the SNMM over the conventional waveguide characterisation methods for thin films were discussed in section 1.3. Analysis of the image charge model for thin films is important if these advantages are to be realised.

Although the image charge model predicts the response of the SNMM to a thin film on a substrate, no work in the literature has demonstrated its use. Nor has this aspect of the model been quantitatively analysed.

A previous study of ferroelectricity in $Ba_{0.5}Sr_{0.5}TiO_3$ thin films [7] showed that the SNMM was able to record changes in permittivity with bias voltage. However, the ability of the SNMM to yield quantitative measurements of permittivity was not explored.

Conventionally, the dielectric properties of thin films are often measured by a co-planar waveguide (CPW) technique [8,9] as discussed in section 1.3 The experiment chosen to analyse the SNMM for the measurement of thin films, was to compare measurements made with the microscope with the well established CPW technique.

To make this comparison SNMM and CPW measurements were performed on the same regions of the same thin film samples. Two $Ba_{0.5}Sr_{0.5}TiO_3$ (BST) thin films on MgO substrates were used for this experiment. The thickness of both films was 700nm to 800nm. BST thin films were chosen due to the popularity of the material in microwave devices. The characterisation of the

voltage-tunable ferroelectric properties of the films using the SNMM is a potential area for future work and will be discussed in the concluding chapter of the thesis. The BST films were grown by Dr P Bao.

To make this comparison, the experimental setup shown in figure 1.2 was used. The SNMM was calibrated for measurements of ε_r as described in the previous section.

Measurements of resonant frequency and quality factor shifts were performed on the thin film samples using the SNMM in the same way as for the calibration samples described in section 5.2.1 above. Each sample was measured at 27 points on the surface aligned with the intended positions of the CPWs. The measurement points are shown schematically in figure 5.6.Figure 5.6 shows the relative positions of the waveguides. The points at which measurements were taken with the SNMM are shown by the intersection of the dashed lines. The waveguides are numbered 1 to 3 on the drawing for reference.

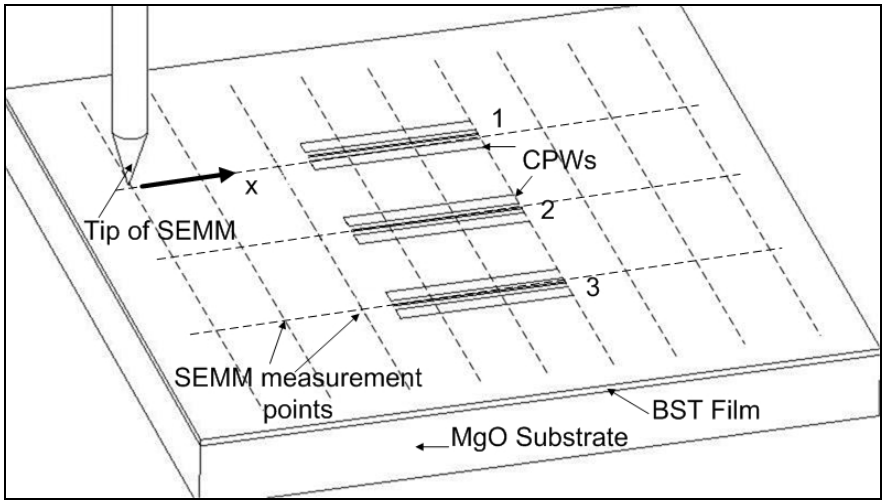

Figure 5.6 The BST film on the MgO substrate, tip of SNMM and position of CPWs.
The direction of increasing x for the SNMM measurements is indicated with an arrow.
The drawing is not to scale.

Once measurements with the SNMM were taken at the intended positions of the CPWs, they could be fabricated onto the film surface. The fabrication was performed by Ms D Holdom, the clean room technician. A 50 nm thick chromium adhesion layer was sputtered onto the BST film, followed by a gold film 750 nm thick . This thickness was chosen to keep conductor losses low

for the CPW measurements. The metal was patterned into ground-signal-ground CPWs aligned with the original SNMM measurements by standard photolithography and ion beam milling. The microwave impedance and propagation constant of the waveguides were measured using methods that have been described previously [8, 10]. The CPW measurement data points were taken three times and averages calculated in order to generate values of the random uncertainties, which were approximately 0.5%. These measurements (but not the analysis) were performed by Dr PM Suherman.

To convert the raw data for both the SNMM and CPW measurements to relative permittivity and loss tangent, knowledge of the film thickness was needed. To measure the film thickness the metal waveguides were removed by chemical etching and a spiral was patterned into the BST films by photolithography and ion-beam milling to enable measurements using a profileometer. Ten measurement scans were performed at each location using the profileometer.

The raw measurement data of $\Delta f_r/f_r$ for the SNMM were converted to relative permittivity using the calibration constant, A, (see section 5.2.1) and equations (3.15) and (3.16) from the image charge model for dielectric thin films.

The relative permittivity and loss tangent from the CPW data was found using the method described previously [8, 10].

To calculate the uncertainties in the final value of ε_r from the SNMM measurements, the contributions of uncertainties from the measured values of ε_1 (substrate permittivity), d (film thickness), R (radius of tip), $\Delta f_r/f_r$ and A were considered. To calculate the uncertainty the following equation was used,

$$\sigma(\varepsilon_r) = \sqrt{\begin{aligned}&\left(\frac{\partial \varepsilon_r}{\partial R}\right)^2 \sigma(R)^2 + \left(\frac{\partial \varepsilon_r}{\partial d}\right)^2 \sigma(d)^2 + \left(\frac{\partial \varepsilon_r}{\partial A}\right)^2 \sigma(A)^2 \\ &+ \left(\frac{\partial \varepsilon_r}{\partial \Delta f_r / f_r}\right)^2 \sigma(\Delta f_r / f_r)^2\end{aligned}} \quad . \tag{5.2}$$

where $\sigma(R)$, $\sigma(d)$, $\sigma(A)$ and $\sigma(\Delta f_r/f_r)$ are the random uncertainties associated with R, d, A and $\Delta f_r/f_r$ respectively. The differentials in equation (5.2) were determined using equation (3.15) by finding the change in the predicted permittivity for a given change in each variable in turn.

Figures 5.7a, 5.7 b and 5.7c show the measured relative permittivity of the film in the vicinities of waveguides 1, 2 and 3 respectively for the TEM 1/4λ mode. Shown on the same graphs are the results from the corresponding CPWs. The results from the CPWs are shown as a straight line indicating the single value over its length. The results from the SNMM are shown as crosses with uncertainty bars.

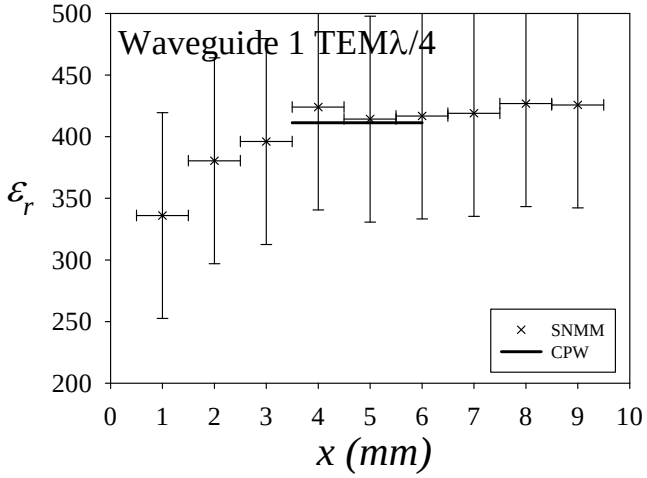

Fig. 5.7a Measured SNMM and CPW results for the TEM 1/4λ mode in the vicinity of waveguide 1.

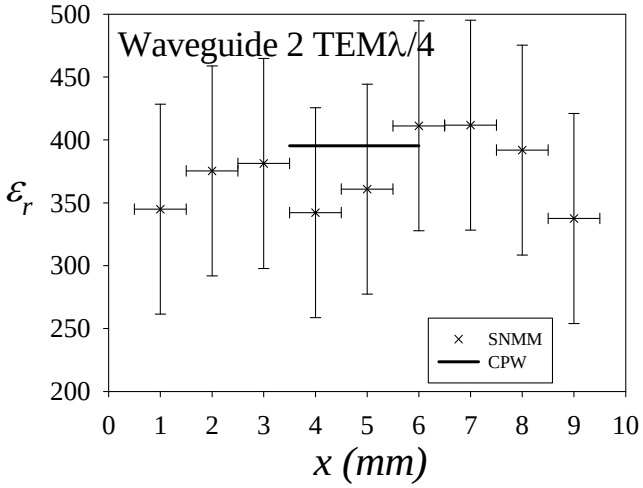

Fig. 5.7b Measured SNMM and CPW results for the TEM 1/4λ mode in the vicinity of waveguide 2.

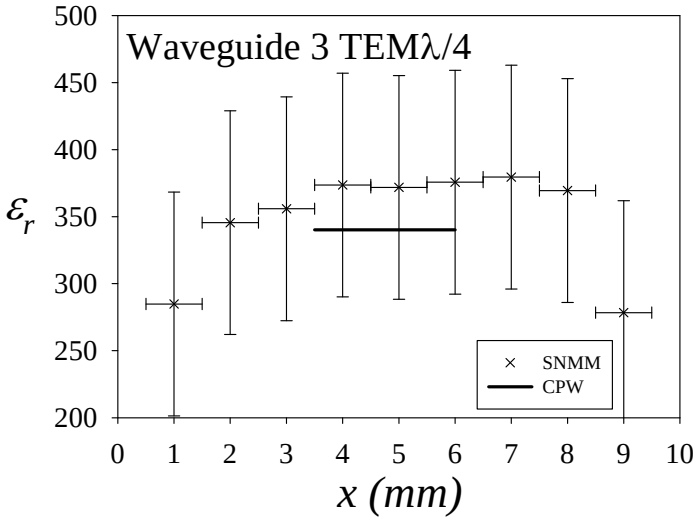

Fig. 5.7c Measured SNMM and CPW results for the TEM 1/4λ mode in the vicinity of waveguide 3

In the above figures, the uncertainty bars on the positions at which SNMM data were taken is +/- 0.5mm. In each case the values of ε_r from the CPWs lie within the uncertainty bars of the SNMM measurement showing general agreement. The vertical uncertainty bars for the extracted relative permittivity are of the order of 25% for all the SNMM thin film measurements. This total uncertainty in ε_r is due to relative contributions from the uncertainties in $\Delta f/f$, d, R and A of 3%, 6%, 8%, and 83% respectively, as computed from equation (5.2). Therefore, the uncertainty in the final result of ε_r is dominated by the uncertainty in the calibration constant, A. Even though figure 5.2a appears to show a good fit when measuring bulk samples, the uncertainty in A becomes significant when the image charge model is extended to thin films. This makes accurate measurements of thin films difficult.

Figures 5.8a, 5.8b and 5.8c show the measured relative permittivity of the film in the vicinities of waveguides 1, 2 and 3 respectively for the TEM 3/4λ mode.

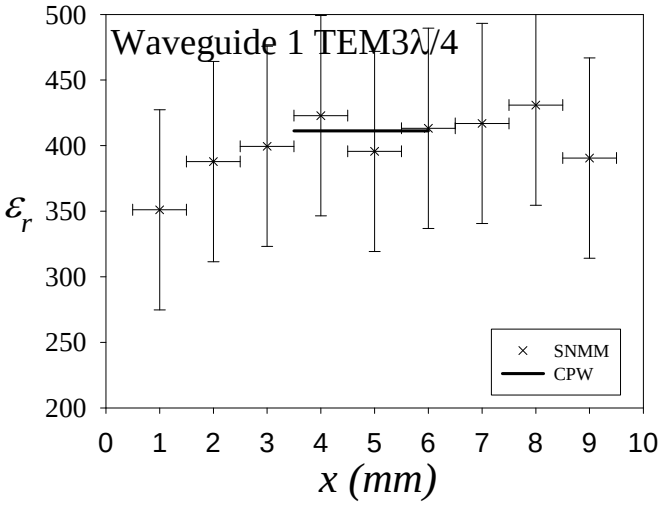

Fig. 5.8a Measured SNMM and CPW results for the TEM 3/4λ mode in the vicinity of waveguide 1

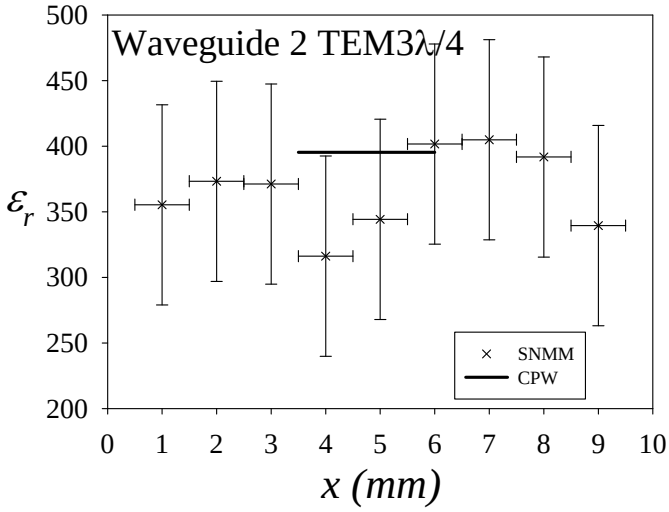

Fig. 5.8b Measured SNMM and CPW results for the TEM 3/4λ mode in the vicinity of waveguide

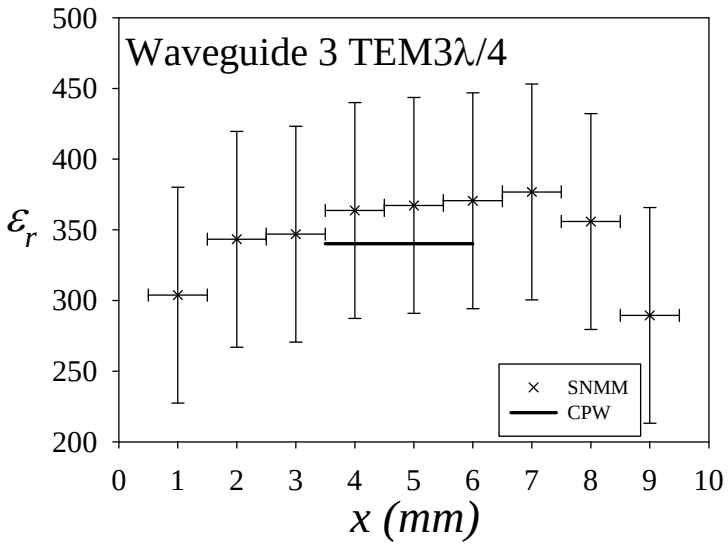

Fig. 5.8c Measured SNMM and CPW results for the TEM 3/4λ mode in the vicinity of waveguide 1

Results from the TEM 5/4λ were unusable as the losses in the thin films were too high, making it impossible to observe the resonance clearly.

Figures 5.8a to 5.8c show good agreement with data taken using the TEM λ/4 mode (shown in figures 5.7a to 5.7c) suggesting no significant dispersion of the dielectric properties of the BST between 1.8 and 4.4 GHz. The dominant contribution to the uncertainty bars in figure 6a, 6b and 6c remains the uncertainty in *A*.

When figures 5.7a to 5.7c are compared with 5.8a to 5.8c it can be seen that the same trends in the films are detected by both modes. For instance, figures 5.7a and 5.8a show a general rise in permittivity from left to right of the sample. Figures 5.7b and 5.8b show a dip in permittivity near the middle of the sample. Figures 5.7c and 5.8c show a constant permittivity in the middle of the sample with a relative drop at both edges of the sample. This shows that, even though the SNMM measurement uncertainty bar is large, it is detecting variations across the thin film. These can be seen more clearly within the raw data, where the uncertainty bars are smaller. The raw data for the TEM λ/4 mode is shown in figures 5.9a to 5.9c.

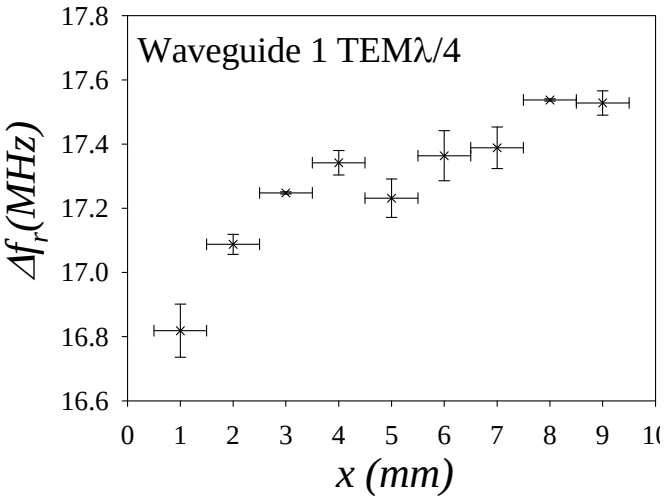

Fig. 5.9a Measured SNMM frequency shifts for the TEM λ/4 mode in the vicinity of waveguide 1.

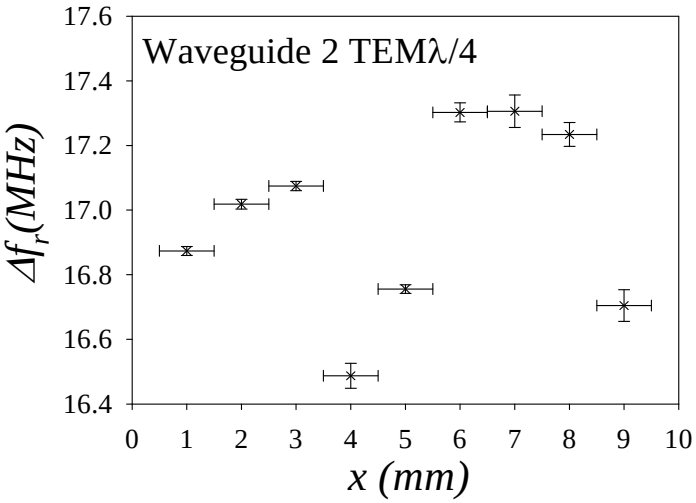

Fig. 5.9b Measured SNMM frequency shifts for the TEM λ/4 mode in the vicinity of waveguide

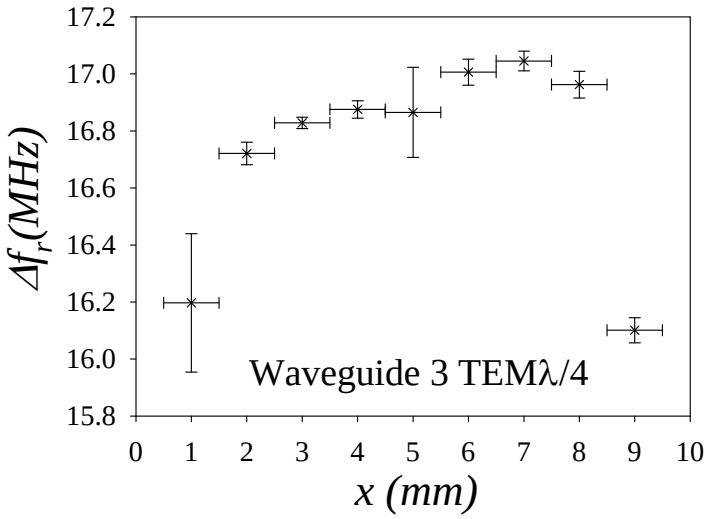

Fig. 5.9c Measured SNMM frequency shifts for the TEM λ/4 mode in the vicinity of waveguide 3.

Figures 5.10a, 5.10b and 5.10c show the measured relative permittivity of the film on the second sample in the vicinities of the respective waveguides for the TEM 1/4λ mode.

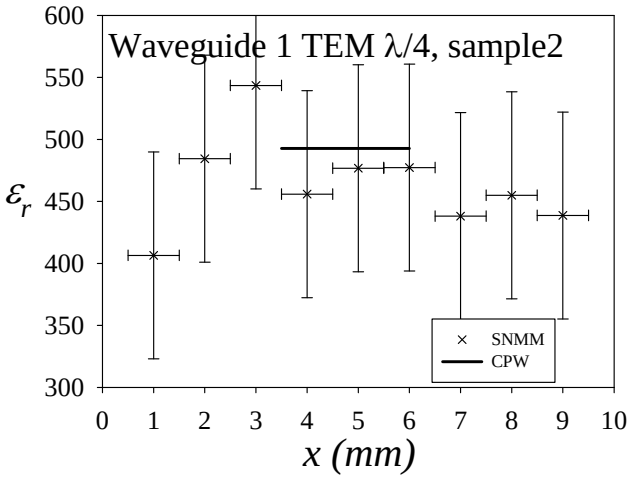

Fig. 5.10a Measured SNMM and CPW results for the TEM 1/4λ mode in the vicinity of waveguide 1 for sample2.

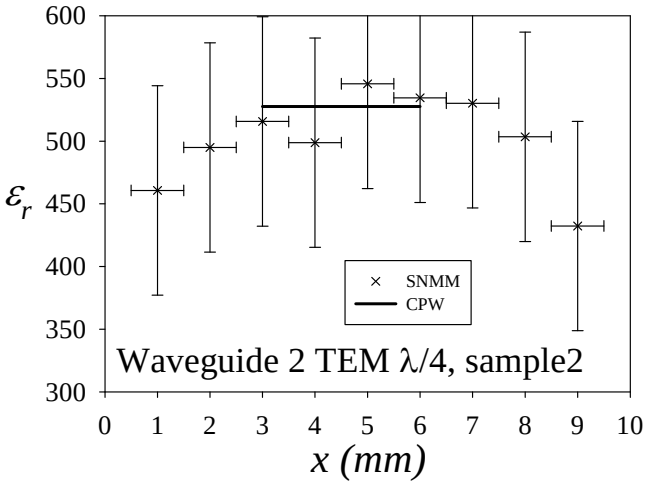

Fig. 5.10c Measured SNMM frequency shifts for the TEM 1/4λ mode in the vicinity of waveguide 2 for sample2.

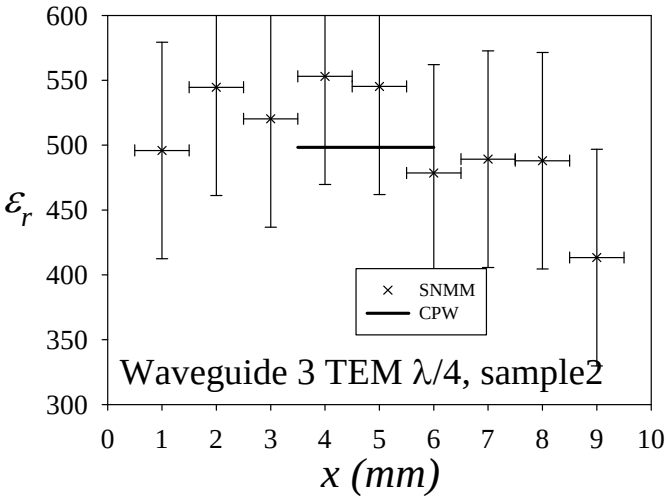

Fig. 5.10c Measured SNMM frequency shifts for the TEM 1/4λ mode in the vicinity of waveguide 3 for sample2.

As with the previous sample measurements, general agreement between the CPW and SNMM is shown along with variations in the thin film which again were clearer in the raw data and therefore may be regarded as real effects.

Although the SNMM was not calibrated for loss measurements, information can still obtained from the raw data. Figures 5.11a, 5.11b and 5.11c show the shift in unloaded quality factor for the measurements described above in the vicinity of the waveguides 1 to 3 measured using the TEM 1/4λ mode.

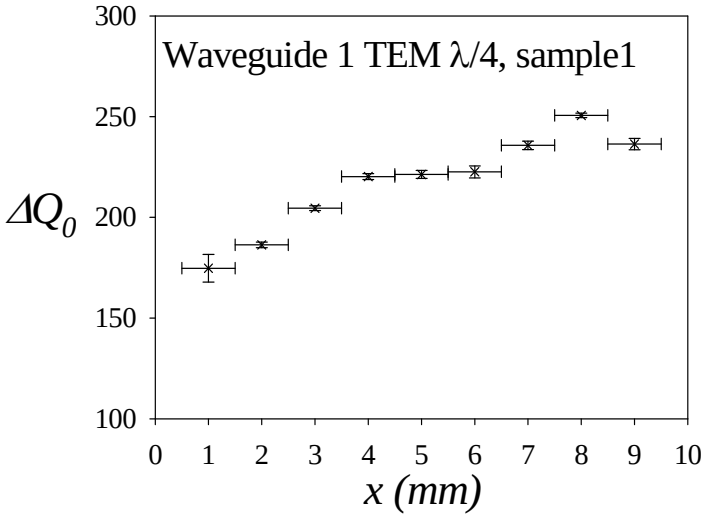

Fig. 5.11a Measured SNMM frequency shifts for the TEM 1/4λ mode in the vicinity of waveguide 1 for sample1.

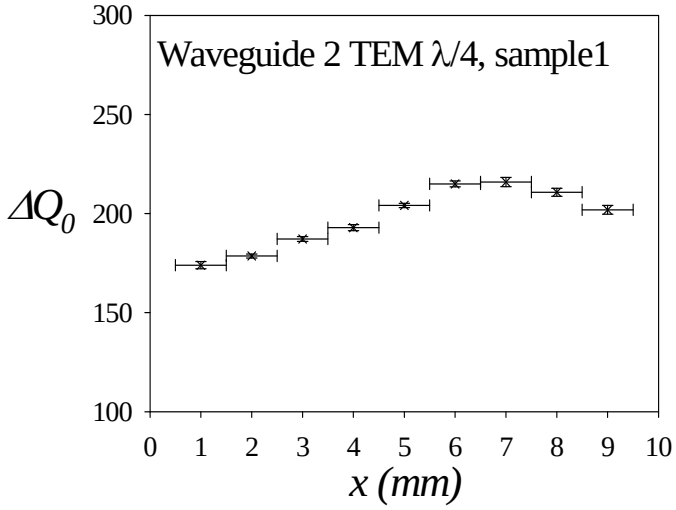

Fig. 5.11b Measured SNMM frequency shifts for the TEM 1/4λ mode in the vicinity of waveguide 2 for sample1.

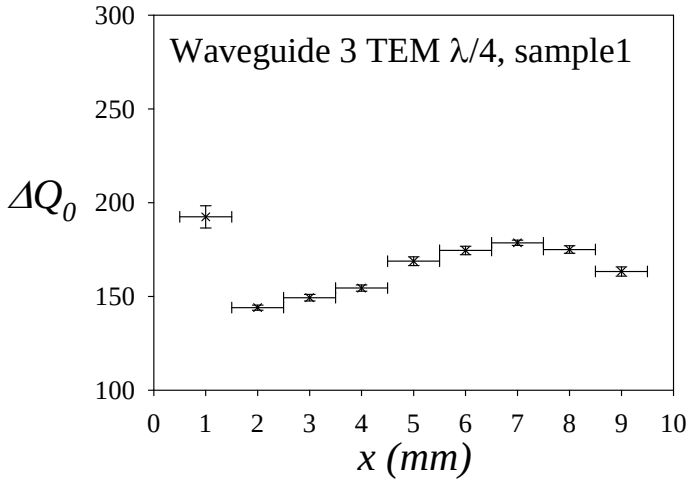

Fig. 5.11c Measured SNMM frequency shifts for the TEM 1/4λ mode in the vicinity of waveguide 3 for sample1.

Figures 5.10a, 5.10b and 5.10c show that there is a general rise in thin film loss from the left side of the sample to the right peaking at approximately x = 7mm.

If the straight line produced by equation (5.1) were to be used to determine the effective $tan\delta$ of the sample, then an unloaded quality factor shift of 200 would result in an effective $tan\delta$ = 0.102. This means the loss tangent of the actual film would be $tan\delta$ > 0.102. The measured and calculated values of $tan\delta$ using the CPW's are of the order of 0.06. This difference could be due

to the fact that the empirically derived loss calibration shown in figure 5.5 is not a straight line for large values of $tan\delta$.

If the loss could be calibrated confidently, the size of the uncertainties would be similar to those of ε_r measurements as the calibration constant, A, is also contained within equation (3.17), which gives the quality factor shift due to a thin film on a substrate. However, it is impossible to say whether the CPW loss measurements would fall within the uncertainty bar of the SNMM measurement.

All that can gathered from the quality factor shift data is that the measured loss tangent of the film is $tan\delta > 0.102$, and that the SNMM is capable of measuring differences in thin film losses across the surface.

In conclusion, the largest source of uncertainty for both relative permittivity and loss measurements of bulk and thin film samples is the uncertainty in the calibration constant, A. While this uncertainty is small for bulk sample measurements it is too large for thin film measurements. The SNMM's ability to detect non-uniformities in dielectric thin films has been demonstrated. Uncertainty arises when converting the raw data to relative permittivity and loss tangent. This highlights the need for a set of standard samples with as wide a range of ε_r and $tan\delta$ values as possible which have all been previously measured using the same techniques over the range of frequencies. Samples with the same permittivity but different loss tangents would be useful for calibrating the loss tangent.

Chapter 5 – Bibliography

[1] H. F. Cheng, Y.-C. Chen, and I.-N. Lin, "Evanescent microwave probe study on dielectric properties of materials," *J. Eur. Ceram. Soc.*, vol. 26, pp. 1801, 2006.

[2] C. Gao, B. Hu, I. Takeuchi, and K.-S. Chang, "Quantitative scanning evanescent microwave microscopy and its applications in the characterization of functional materials libraries," *Meas. Sci. Technol.* vol. 16, pp. 248, 2004.

[3] A. Imtiaz, T. Baldwin, H. T. Nembach, T. M. Wallis, and P. Kabos, "Near-field microwave microscope measurements to characteize bulk material properties," *Appl. Phys Lett.*, vol. 90, 243105, 2007.

[4] D. P. Kimber, R. C. Pullar, and N. McN. Alford, "The effects of dielectric loss and tip resistance on resonator Q of the scanning evanescent microwave microscopy (SNMM) probe", *Meas. Sci. Technol.*, vol. 19, 115502, September 2008.

[5] C. Gao, and X.-D. Xiang, "Quantitative microwave near-field microscopy of dielectric properties", *Rev. Sci. Instrum.*, vol. 69, pp. 3841, 1998.

[6] S. Ramo, J. R. Whinery, T. V. Duzer. *Fields and Waves in Communication Electronics*. John Wiley and Sons. 1st Edition. New-York, 1965.

[7] S. Hyun, J. H. Lee, S. S. Kim, and K. Char, "Anisotropic tunning behaviour in epitaxial $Ba_{0.5}Sr_{0.5}TiO_3$ thin films", *Appl. Phys. Lett.* vol 77, pp.3084, 2000.

[8] P. M. Suherman, T. J. Jackson, and M. J. Lancaster, "Comparison of techniques for microwave characterization of BST thin films," *IEEE. Trans. Micro. Theory Tech*,. vol. 55, pp. 397, 2007.

[9] S. S. Gevorgian, "Basic characteristics of two layered substrate coplanar waveguides," *Electron. Lett.* vol. 30, pp. 1236, 1994.

[10] P. M. Suherman, T. J. Jackson, Y. Y. Tse, I. P. Jones, R. I. Chakalova, and M. J. Lancaster, "Microwave properties of $Ba_{0.5}Sr_{0.5}TiO_3$ thin film coplanar phase shifters," *J. Appl. Phys.*, vol. 99, 104101, 2006.

Chapter 6 Conclusions and Future Work

6.1 – Conclusions

This chapter summarises the conclusions made throughout the thesis and discusses necessary further work for the SNMM.

The operation of the SNMM has been detailed in chapter 4 in terms of cavity design, dielectric sample measurement procedure, the coupling coefficient and sources of noise.

The calculated quality factor of the cavity was calculated to be approximately 3.3 times larger than the measured value highlighting the need for a more accurate model of the system.

The simulations of the dielectric samples as resonators showed that many possible resonant modes exist within the samples between the frequencies used for measurements. This check for SNMM measurments has previously not been reported. Although it was difficult to determine with certainty if the resonant modes in the samples were being excited from the measurement results shown in chapter 5, the adequate fit to the model, and the fact that the near field is a non-propagating wave, suggest that the modes within the samples were not excited.

The issues surrounding the strength of coupling to the cavity for the SNMM have been explored and presented for the first time including the optimal coupling value and the limit of sensitivity due to thermal noise. It was concluded that a small coupling strength will increase the sensitivity to quality factor shifts while it has little effect on the sensitivity to frequency shifts (due to sample ε_r). However, it was shown that the coupling strength does make the frequency shift more or less sensitive to samples losses. Although this is a common result, it has not previously been shown for the SNMM. Through the derivation it was shown that a universal optimum coupling strength does not exist, but is dependent on the sample to be measured. The derivations of section 4.4 can be applied to any resonant measurement system. This showed that by utilising

small coupling, the frequency shift of the resonator could be made due to the sample ε_r only, helping to separate the effects of sample ε_r and loss tangent.

The derivation of the smallest measurable frequency and quality factor shifts due to thermal noise as a function of the coupling coefficient showed the effect of coupling both signal and noise power into the SNMM for the first time. This derivation showed that the thermal noise in the system was smaller than the vibrational noise and hence negligible until the system is improved.

It was shown in section 4.4.3 how the smallest measurable changes in frequency and Q could be affected by altering the coupling coefficient. The calculated smallest measurable changes in frequency and Q for a coupling of β = 0.08 were 14kHz and $33.5 \cdot 10^{-3}$ respectively. As the vibrations in the measurement system limit the smallest measurable changes in frequency and Q to ~50kHz and ≈5 respectively, this highlighted the need for the SNMM to be in a vibrationally isolated environment.

The modes of the resonator used were calculated, simulated, measured and hence identified. This provided an efficient method of identifying modes for resonators and showed flaws in the design of the resonator in that too many modes are supported at higher frequencies increasing the chance of degenerate modes and limiting the number of useable modes with confidence to the first 2 TEM modes.

From measurements of the resonant frequency with room temperature it was shown that if a frequency shift resolution of 10kHz or less than is desired, a room temperature stability of 1 degrees Celsius or less is required. Although trivial, this study has previously not been reported for the SNMM.

The effect of tip bending (due to tip-sample contact force) on measurements and the ability of the results to fit to the image charge model was investigated and presented for the first time. It was shown that samples of similar permittivity such as MgO and Al_2O_3 can still be distinguished between. This work also showed that permanent bending of the tungsten tip does occur, and its effect on the calibration constant was quantified for the first time.

For the first time, the image charge model was quantitatively analysed via an uncertainty between measured data and the predicted response for bulk dielectric samples. The model was found to adequately predict the frequency shift of the resonator for bulk samples between ε_r values of 1 and approximately 30. For the first time it was shown that there was a 5% uncertainty in fitting to the model for the TEM 1/4λ and 3/4λ modes and that the tip length of 1mm is responsible for this uncertainty. It was also shown that this uncertainty increases with tip length. Therefore, the assumption of the image charge model that the tip can be modelled as a charged sphere was analysed for the first time and quantitatively shown that it depends on the tip length.

The response of the SNMM to measurements of sample loss was not calibrated confidently. The measurement data was unable to be fitted to the image charge model. Although the proposed equation, (5.1), for a calibration of the loss response was suggested, not enough data was available to confirm it.

For the first time, the ability of the image charge model to characterise thin films was quantitatively analysed. It was shown in section 5.3 that a 5% uncertainty in the calibration constant contributes significantly to a 25% uncertainty when measuring the ε_r of thin films. If this uncertainty could be made negligible, the total uncertainty in the final result would reduce to 5%. The next significant uncertainties to be reduced in the measurements of thin films would be the film thickness and the tip radius. The later one could be reduced by using electron microscopy to image and measure the tip. However, the uncertainty in the measurements of the thickness of thin films remains a barrier to reducing the overall uncertainty.

For the first time, SNMM measurements of thin films were compared against the tried and tested co-planar waveguide method showing general agreement and demonstrating the potential ability of the SNMM as a worth while dielectric thin film characterisation technique. This also demonstrated for the first time the ability of the SNMM to detect differences in thin film properties along the length of the film and the co-planar waveguide itself demonstrating its effectiveness over the technique.

In conclusion, it was quantitatively demonstrated for the first time that the widely used image charge model only produces an uncertainty of 5% when measuring bulk dielectrics, but this uncertainty leads to a 25% uncertainty when measuring dielectric thin films.

6.2 – Future Work and Recommendations

To achieve more accurate and convenient measurements the SNMM needs to be placed in an environmentally controlled place. This environment would require a temperature stability outlined above. The largest acceptable vibrational noise level (from whatever source) cannot be quantified however, as it depends on the sample and the tip.

Non-contact mode must be implemented to irradicate the unquantifiable error posed from contact mode permanent tip deformation. Non-contact mode may have problems due to different sized water layers on samples which are functions of environmental humidity. However, this can be quantified by measuring frequency shifts of given samples for different humidities. Although water layers pose a problem to contact mode also, they cannot be accounted for in this way as tip bending will always have occurred between consecutive measurements.

Once these recommendations have been made, the SNMM in question can be improved further by redesigning it to accommodate higher *Q*'s and less degenerate modes at higher frequencies.

More standard samples, all characterised using the same measurement method are required over a large a range of ε_r as possible to give confidence in measurements, particularly measurements of loss.

A study of the increasing spatial resolution with decreasing tip size (and hence decreasing signal) should be done to ascertain at what tip radius the signal power falls below measurable levels. This would need to be quantified in terms of a given change in sample permittivity.

Material libraries samples present interesting samples for measurement using the SNMM. However, they often contain conducting layers between the film and the substrate to allow

capacitance measurements using patterned electrodes on the film surface. This however would be very difficult to measure with the SNMM as the image charge model does not allow for a conducting layer under a dielectric layer. This problem could be fixed with the use of electromagnetic modelling in order to calibrate the SNMM. Also, the close proximity of the conducting layer would cause extra losses in the measurement and reducing the signal output, this is confounded by the fact that thin films are often lossy themselves.

Measurements of ferroelectric tunebility of thin films using the SNMM could be done by placing the tip of the SNMM in between two electrodes (such as the ground and signal lines of a CPW) and using them to apply a bias field and hence alter the permittivity of the film. However, close proximity of the electrodes is needed so that safe voltages can be used. This could create a problem for the SNMM as the presence of the conducting electrodes cannot be accounted for in order to obtain quantitative measurements. However, qualitative measurements may be achievable. The electric field created by the bias voltage on the electrodes may interfere with the field from the tip within the dielectric interfering with measurements. Applying the bias voltage vertically through the resonator itself would require an electrode under the thin film which would alter the frequency shift in an unpredictable way. However, an accurate simulation model would be attractive as it would be able to be used to calibrate the SNMM for any situation imaginable.

When considering further work on simulations the effect of the radius of the tip on the system response cannot be underestimated. If CST is used, the shape of the tip at the very end will have large effects on the systems response even if the mesh in that area is larger than the tip radius. In general, a denser mesh must used wherever there is relatively large electric or magnetic fields in the system. Of course this would include the tip and sample.

Appendix A – Publications

- D. J. Barker, P. M. Suherman, T. J. Jackson and M. J. Lancaster. “Comparison of Scanning Evanescent Microwave Microscopy with Co-Planar Waveguide Methods of Characterization of $Ba_{0.5}Sr_{0.5}TiO_3$ Thin Films”. *ISAF 2009 — Proceedings of the 18th IEEE International Symposium on Applications of Ferroelectrics.*

Comparison of Scanning Evanescent Microwave Microscopy with Co-Planar Waveguide Methods of Characterization of $Ba_{0.5}Sr_{0.5}TiO_3$ Thin Films

D. J. Barker[1], P. M. Suherman, T. J. Jackson and M. J. Lancaster
School of Electrical, Electronic and Computer Engineering, University of Birmingham, Edgbaston, Birmingham, B15 2TT, United Kingdom
[1]. Email: DJB263@bham.ac.uk

Abstract — The permittivity of a barium strontium titanate thin film was measured at 1.8 GHz and 4.4 GHz with a scanning evanescent microwave microscope (SEMM) and co-planer waveguides (CPW). The raw data suggests the SEMM has sufficient sensitivity to detect significant variations in permittivity across the film that the CPWs could not. The average value of permittivity extracted from the data is consistent with that extracted from the co-planar waveguide measurements but the error bars associated with the extraction are large, of the order of 25 %. The significant contribution to the error in the final result from the SEMM is due to the analytical model used.

INTRODUCTION

The development of dielectric materials, including thin films, is important for enhanced functionality in microwave and radio communications. Therefore, the improvement of dielectric characterization techniques is also important.

Scanning evanescent microwave microscopy (see review article [1]) is a technique with high through put efficiency for determining the local dielectric properties of materials. The scanning evanescent microwave microscope (SEMM) consists of an open ended coaxial resonator where the central conductor is terminated in a small tip. The tip concentrates the microwave field energy into a small volume allowing localized, measurements of complex permittivity with spatial resolution of the order of 5-10 microns [2]. This is done through measuring the changes in resonant frequency and quality factor (Q) of the cavity. Figure 1 shows the configuration of the resonator, tip, network analyzer and computer used in the experiments.

Higher order modes of the SEMM allow for measurements to be made at several different frequencies. This capability has been utilized in to study frequency dispersion in the dielectric properties of barium strontium titanate (BST) thin films [3].

Conventionally, the dielectric properties of thin films are often measured by a co-planar waveguide (CPW) technique [4, 5]. The potential advantage of the SEMM over the CPW technique is that the localized measurements allow the variation in permittivity across a thin film to be measured. This allows for the improvement of deposition techniques to create more uniform films.

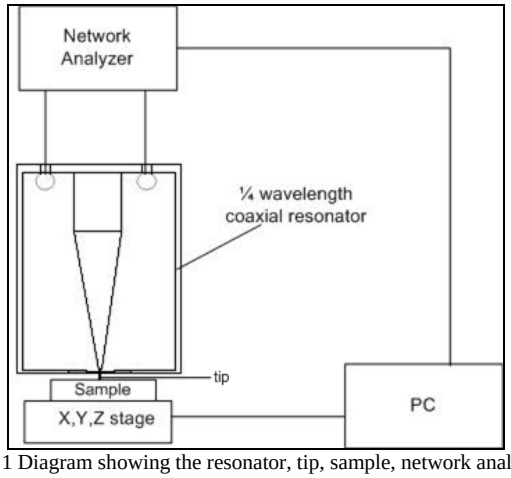

Fig. 1 Diagram showing the resonator, tip, sample, network analyzer and PC for motion control and data acquisition.

Because it is well established, the CPW technique is a good benchmark for evaluation of new methods such as the SEMM. Comparison of methods over the same frequency ranges is important because of the possibility of dispersion; such a comparison has

not been previously reported. A significant earlier study of ferroelectric $Ba_{0.5}Sr_{0.5}TiO_3$ thin films [6] showed that the SEMM was able to record changes in permittivity with bias voltage. However, the ability of the SEMM to yield quantitative measurements of permittivity was not explored. The quantitative analysis requires a theoretical model of the SEMM.

Analytical models have been produced to describe the SEMM. These include lumped element models [7] and the image charge model [8]. Numerical finite element methods have also been applied to the SEMM in order to predict the response to both bulk and thin film samples [9, 10]. Modeling has been applied to both the full (resonator and tip) [11] and simplified (tip only) [9, 10] cases. The image charge model remains the most widely used analytical model, as it not only describes the response to bulk samples (when the dimensions of the sample are much bigger than all the dimensions of the tip) but also the response to thin films on a substrate and experimental parameters such as the tip to sample distance [8].

The first and most important step for any measurement technique is calibration. Calibration of measurements of the real part of permittivity using the image charge model has been independently verified numerically [12]. Problems with the calibration of measurements of loss tangent using the image charge model have been highlighted by various researchers [1, 12, 13, 14]. In each reference the inability to fit loss measurements to the response predicted by the image charge model [8] is attributed to resonator conductor losses. These become dominant for large permittivity samples, which require extra charge redistributed to the tip to maintain its equipotential surface.

The present work seeks for the first time to quantify errors imposed from the calibration and image charge model particularly when applied to thin films. This is done by comparison of the complex permittivity of a $Ba_{0.5}Sr_{0.5}TiO_3$ thin film obtained by SEMM with data from the CPW technique. In order to make the comparison, SEMM and CPW measurements must be performed on the same regions of the same samples and the thickness of the films must be determined at those positions. The calibration of the SEMM is, in itself, a source of error as will be described. The comparison also highlights the advantages and disadvantages of both techniques.

Quantitative analysis of calibration of the SEMM is necessary in order for it to be validated as a thin film characterization tool. Sources of error must be identified before improvements can be made to the technique.

METHOD

As a first step, the SEMM was calibrated using bulk samples and the image charge model for bulk dielectrics [8]. The samples used for the calibration were a combination of MgO, $NdGaO_3$ and YSZ substrates and standard samples of Peek and Macor obtained from the UK National Physical Laboratory (NPL). The complex permittivity of the substrates was measured using a split post resonator technique [15] at 12 GHz at the NPL.

The real and imaginary parts of the transmission coefficient (S_{21}) of the resonator were recorded with a vector network analyzer before and after the tip was brought into contact with each sample. The force between the tip and the sample was measured using a load cell and kept constant. This was required because the frequency and *Q* shift are dependent on contact force to an extent which depends on the permittivity of the sample [12, 16]. Also, a large tip-sample force may lead to permanent bending of the tip creating a larger effective tip radius, in turn giving a larger frequency shift and invalidating the calibration. A tip to sample force of 2mN +/-0.5mN was applied in each measurement. Each measurement was taken three times and the average and standard deviation were computed. In between each of the three measurements on the same point the resonator was taken out of contact with the sample and then brought back into contact again.

The TEM $\lambda/4$ and TEM $3\lambda/4$ modes of the resonator were measured simultaneously at

each measurement point. Without a sample, these modes occurred at approximately 1.8 GHz and 4.4 GHz.

Measurements of the imaginary part of the transmission parameter S_{21} were plotted against the real part of S_{21}. To account for the effect of leakage between coupling ports, the real and imaginary parts of S_{21} were fitted to the equation for the complex transmission coefficient, *T*,

$$T = L + \frac{d\exp[-2j\delta]}{1 + jQ_L t}. \quad (1)$$

In Equation (1), $t = 2(f-f_r)/f$, f_r is the resonant frequency, Q_L is the loaded quality factor, *d* is S_{21} at the resonant frequency, δ is an arbitrary phase, *L* is the complex leakage vector. This was done because errors in the measurement of f_r, and especially Q_L, can be significant when using the frequency of maximum transmitted power for f_r and the -3dB points for the Q_L when the resonance curve is asymmetric. In the present work the Q_L of both modes used was approximately 1000. For these quality factors and the particular resonator setup, the use of equation (1) provided a factor of 10 reduction of the random error in the quality factor value while improvement in the resonant frequency was negligible.

Values of $\Delta f_r/f_r$ and $\Delta(1/Q_0)$ (where Q_0 is the unloaded quality factor) were then computed and used, along with the known values of ε_r (relative permittivity) and $\tan\delta$, (loss tangent) in equations (2) and (3) in order to calculate the calibration constants *A* and *B* from the image charge model:

$$\frac{\Delta f_r}{f_r} = \frac{f_r - f'}{f_r} = A\cdot\left[\frac{\ln(1-b(\varepsilon))}{b(\varepsilon)} + 1\right] = A\cdot H(\varepsilon) \quad (2)$$

and

$$\Delta\left(\frac{1}{Q_0}\right) = \Delta\left(\frac{1}{Q_0} - \frac{1}{Q_0'}\right) = -\frac{\Delta f_r}{f_r}\cdot[B + \tan\delta]\cdot \quad (3)$$

where

$$b = \frac{\varepsilon_r - 1}{\varepsilon_r + 1}, \quad (4)$$

Here, f' and Q_0' are the resonant frequency and unloaded quality factors when no sample is present. Equation 2 implies a linear relationship between $\Delta f_r/f_r$ and $H(\varepsilon_r)$ where *A* is the gradient of a straight line. Therefore measurements of $\Delta f_r/f_r$ were plotted against $H(\varepsilon) = \ln\left[{(1-b)}/{b} + 1\right]$, and a straight line was fitted. A similar process was used for equation (3) to calculate the constant *B*. This process was completed for the TEM $\lambda/4$ and TEM $3\lambda/4$ modes. The thin film of $Ba_{0.5}Sr_{0.5}TiO_3$ (BST) on MgO substrate was then measured with the SEMM at 27 different locations, as indicated in Figure 1.

In order to form the CPWs, a gold film 750 nm thick on top of a 50 nm thick chromium adhesion layer was sputtered onto the BST film. The metal was patterned into ground-signal-ground CPWs aligned with the original SEMM measurements. The microwave impedance and propagation constant of the waveguides were measured using methods that have been described previously [4, 17]. Finally, the metal waveguides were removed by chemical etching and a spiral was patterned into the BST films by photolithography and ion-beam milling to enable measurements of the thickness of the BST using a profileometer. 10 measurement scans were performed at each location. The BST film was approximately 750 nm thick on average.

Figure 2 shows schematic drawing of the BST film on MgO substrate, illustrating the relative positions of the waveguides and points measured by the SEMM as the intersection of dashed lines. The waveguides are numbered 1 to 3.

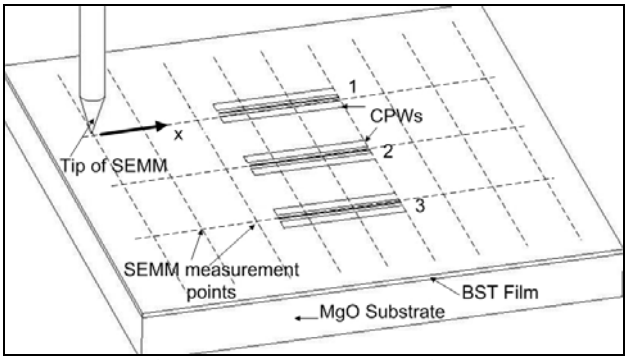

Fig. 2 The BST film on the MgO substrate, tip of SEMM and position of CPWs. The direction of increasing x for the SEMM measurements is indicated with an arrow. The drawing is not to scale.

For the CPW measurements, data points were taken three times and averages calculated in order to generate values of the random errors, which were approximately 0.5%.

To convert from $\Delta f_r/f_r$ to ε_r for the SEMM, the following equation from the image charge model [8] was used,

$$\frac{\Delta f_r}{f_r} = -A\sum_{n=1}^{\infty}\sum_{m=0}^{\infty} b_{eff}^{n-1} b_{20}^{m} b_{21}^{m} \times \left[\frac{b_{20}}{n+1+2mna} - \frac{b_{21}}{n+1+2(m+1)na}\right] \quad (5)$$

where

$$b_{eff} = b_{20} + (b_{10} - b_{20})\exp\left[-0.18\frac{a}{(1-b_{20})}\right] \quad (6)$$

In equations (5) and (6), $b_{20} = (\varepsilon_r\text{-}1)/(\varepsilon_r+1)$, $b_{10} = (\varepsilon_1\text{-}1)/(\varepsilon_1+1)$, $b_{21} = (\varepsilon_r - \varepsilon_1)/(\varepsilon_r + \varepsilon_1)$, ε_r and ε_1 are the relative permittivity of the film and substrate respectively, $a = d/R$ where d is the thickness of the thin film and R is the radius of the tip of the SEMM.

To calculate the error in the final value of ε_r imposed by contributions from errors in the values of ε_1, d, R and $\Delta f_r/f_r$ and A the following equation was used,

$$\sigma(\varepsilon_r) = \sqrt{\left(\frac{\partial\varepsilon_r}{\partial R}\right)^2\sigma(R)^2 + \left(\frac{\partial\varepsilon_r}{\partial d}\right)^2\sigma(d)^2 + \left(\frac{\partial\varepsilon_r}{\partial A}\right)^2\sigma(A)^2 + \left(\frac{\partial\varepsilon_r}{\partial \Delta f_r/f_r}\right)^2\sigma(\Delta f_r/f_r)} \quad . \quad (7)$$

where $\sigma(R)$, $\sigma(d)$, $\sigma(A)$ and $\sigma(\Delta f_r/f_r)$ are the random errors associated with R, d, A and $\Delta f_r/f_r$ respectively. The differentials in equation 7 were determined using equation (5).

RESULTS AND DISCUSSION

Calibration of the SEMM

Figures 3a and 3b show the bulk sample results of $\Delta f_r/f_r$ vs $H(\varepsilon) = \ln\left[(1-b)/b + 1\right]$ with a straight line plotted through the data according to equation (2). The value of the gradient, A, and associated error is shown in each case.

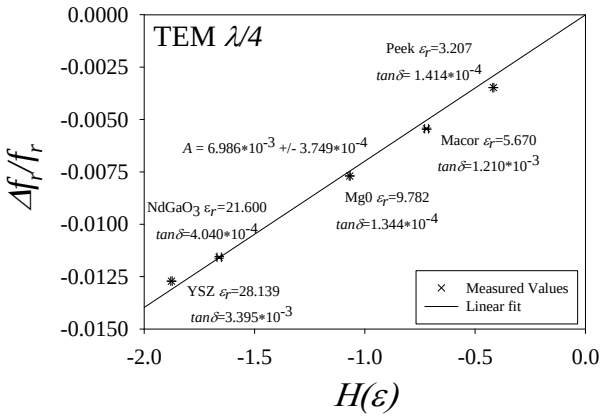

Fig. 3a Graph of frequency shift of the SEMM plotted using equation 2 for TEM λ/4 mode.

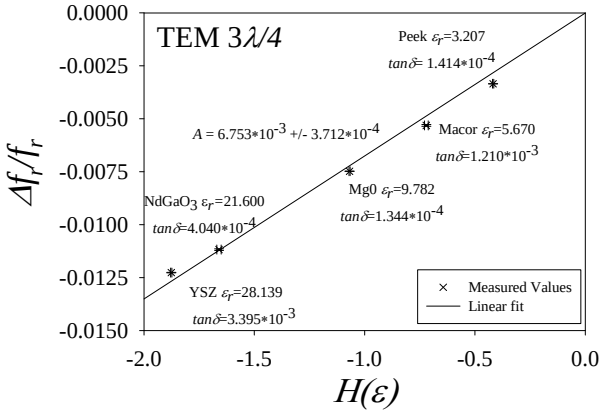

Fig. 3b Graph of frequency shift of SEMM plotted using equation 2 for the TEM3λ/4 mode.

The errors in the straight-line fits are approximately 5% for both the TEM λ/4 and TEM 3λ/4 modes.

Equation 2 assumes a frequency independent value of A. Figures 2a and 2b show a systematic variation of A with permittivity, for both the

TEM λ/4 and TEM 3λ/4 modes, whereby the value of A is underestimated for low permittivity samples and overestimated for high permittivity samples. The original definition of A, $A \approx 16R_0 \ln(R_2/R_1)/\lambda$, appearing in [8], shows a frequency dependence, although a constant value was used for calibrations, as done here. When measured values of $\Delta f_r/f_r$ for the Peek and YSZ samples were used to calculate values of A individually for each one using equation (2), the difference in the two values of A was 20%. In turn, putting the various values into the definition of A above, for Peek and YSZ, creates two values of A which differ by only 3%.

Therefore, although, the curvature of the data seen in figures 2a and 2b is consistent with the frequency dependence of A shown in the definition [8], the extent of the variation in the data is larger than expected from the definition.

Although the calibration constant for each of the modes shown are similar, individual calibrations for each mode must be done due to the different coupling and responses of each mode.

In order to calibrate the SEMM for the loss, Equation (3) was considered. Equation (3) implies a linear function of $\Delta(1/Q_0)/\Delta f/f$ with $\tan\delta$. However, the data does not show this, meaning the calibration constant B, proposed in these equations is not permittivity/frequency independent.

Several other similar equations for $\Delta(1/Q_0)$ involving more constants have been proposed [1, 12], but all of these exhibit the same problem of the non linearity described above. In [1] it is stated clearly that the calibration constant, B exhibits strong frequency and permittivity dependence. A further function was been proposed [14] where a permittivity dependent B term was considered and extra quadratic frequency shift terms were added in an attempt to account for the observed quadratic response. However, this did not describe the response fully.

Figure 3 shows a graph of the measured values of $\Delta(1/Q)$ vs $\tan\delta$ which indicates a logarithmic response. Therefore an equation of the form

$$\Delta\left(\frac{1}{Q_0}\right) = \Delta\left(\frac{1}{Q_0} - \frac{1}{Q_0'}\right) = D + D' \ln(\tan\delta) \qquad (5)$$

is proposed. The function $\Delta(1/Q_0)$ is plotted vs $\ln(\tan\delta)$ in the insert of figure 3.

Although a good fit is shown to the proposed function and can be used for the measurement of bulk samples it cannot however be used for thin films as the equations of the image charge model describing the response for thin films are based on equations (2) and (3) [8].

Because of the large deviation of $\Delta(1/Q_0)$ from equation 3 and the fact that the proposed equation (5) is not a part of the image charge model, the SEMM was not calibrated for loss, meaning sensible values of $\tan\delta$ of the BST film could not be obtained.

The order of increasing Q_0 factor shifts is consistent with the order of increasing sample $\tan\delta$, meaning that the measured Q_0 factor shifts are dominated by sample loss.

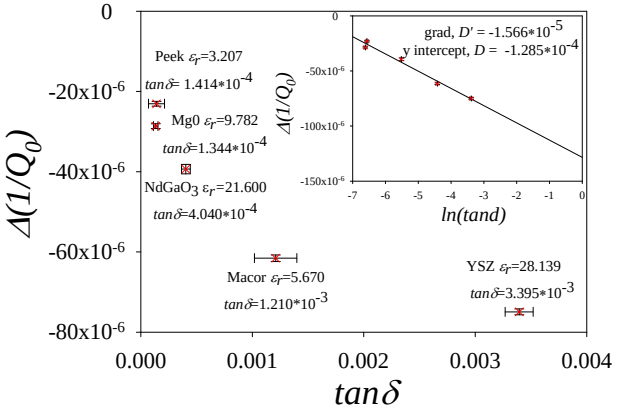

Fig. 3 Results of $\Delta(1/Q_0)$ vs $\tan\delta$ and vs $\ln(\tan\delta)$ in the insert. $\Delta(1/Q_0)$ vs $\tan\delta$ indicates a logarithmic relationship which is confirmed by the plotting of a straight line through $\Delta(1/Q_0)$ vs $\ln(\tan\delta)$ in the insert.

BST Thin Film Results

Figures 4a, 4b and 4c show the measured relative permittivity of the film in the vicinities of waveguides 1, 2 and 3 respectively for the TEM λ/4 mode. Shown on the same graphs are the results from the corresponding CPWs. The results from the CPWs are shown as a straight line indicating the single value over

its length. The results from the SEMM are shown as crosses with error bars.

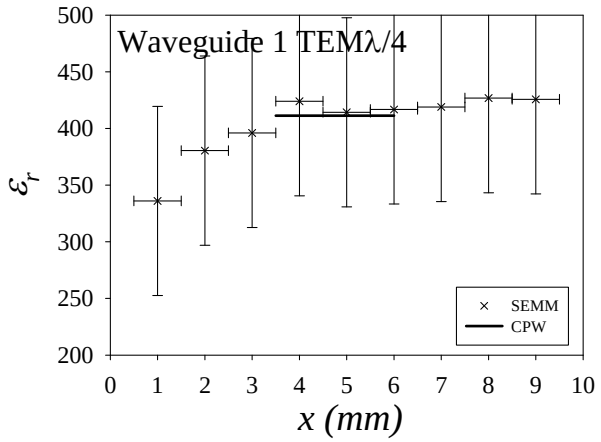

Fig. 4a Measured SEMM and CPW results for TEMλ/4 in the vicinity of waveguide 1

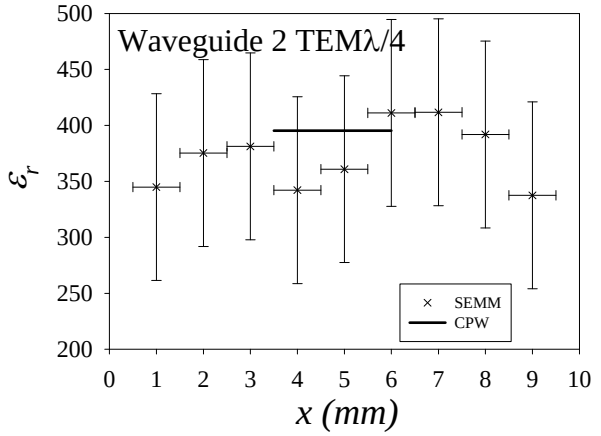

Fig. 4b Measured SEMM and CPW results for TEMλ/4 in the vicinity of waveguide 2

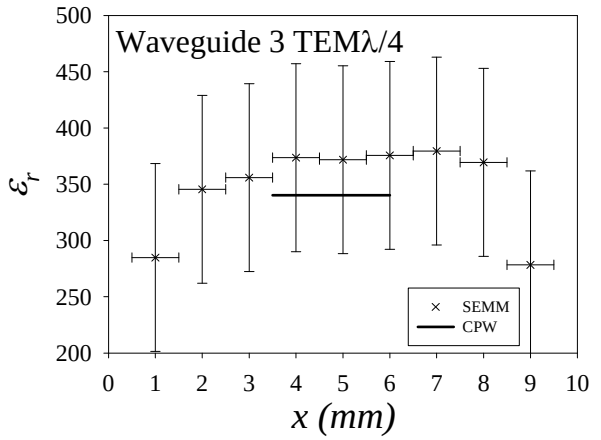

Fig. 4c Measured SEMM and CPW results for TEMλ/4 in the vicinity of waveguide 3

The error bars on the SEMM data in the x axis are +/-0.5mm.

In each case the values of ε_r from the CPWs lie within the error bars of the SEMM measurement showing general agreement.

The errors in $\Delta f/f$, d, R and A contribute 3%, 6%, 8%, and 83% respectively to the overall error bars in the values of ε_r as computed from equation (7). The overall error bars for the extracted relative permittivity are of the order of 25%. The large uncertainty is dominated by product in the third term in equation (7). This contains the differential of the permittivity with respect to the calibration constant A and the error in that calibration constant from the bulk image charge model. Even though figure 3a appears to show a good a fit when measuring bulk samples the error in A becomes significant when the image charge model is extended to thin films and prevents accurate measurements. The raw data shown in figure 5 shows considerably smaller error bars illustrating that it is not a measurement error which is responsible for the error in the final result.

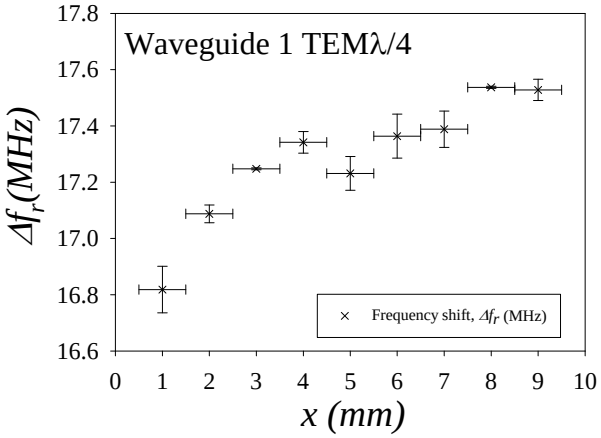

Fig. 5 Measured frequency shifts for the TEM λ/4 mode in the vicinity of waveguide 1.

Figures 5a, 5b and 5c show the permittivity extracted from the frequency shift of the TEM 3λ/4 mode. The data from both modes are in good agreement, suggesting no significant dispersion of the dielectric properties of the BST between 1.8 and 4.4 GHz. The dominant contribution to the error bars in figure 6a, 6b and 6c remains the uncertainty in A.

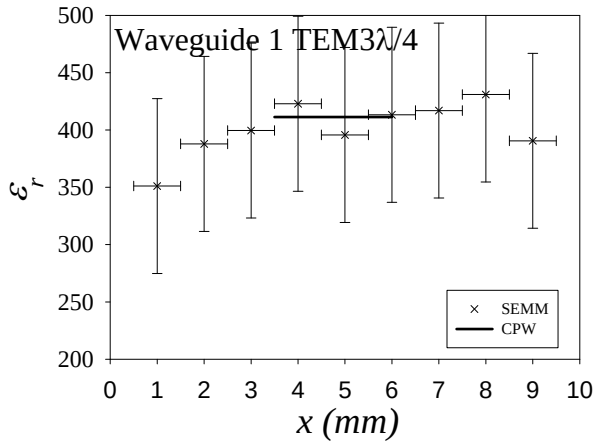

Fig. 6a Measured SEMM and CPW results for the TEM 3λ/4mode in the vicinity of waveguide 1

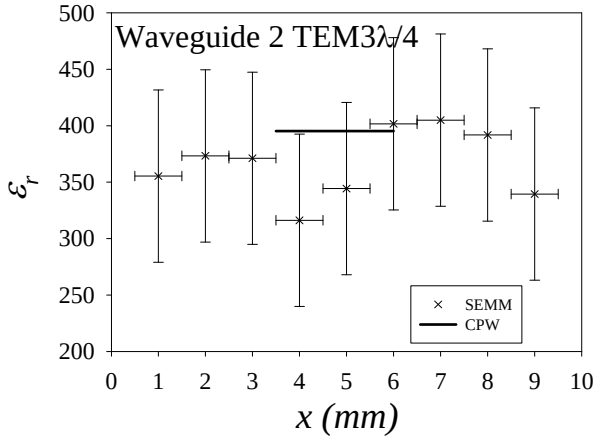

Fig. 6b Measured SEMM and CPW results for the TEM 3λ/4 mode in the vicinity of waveguide 2

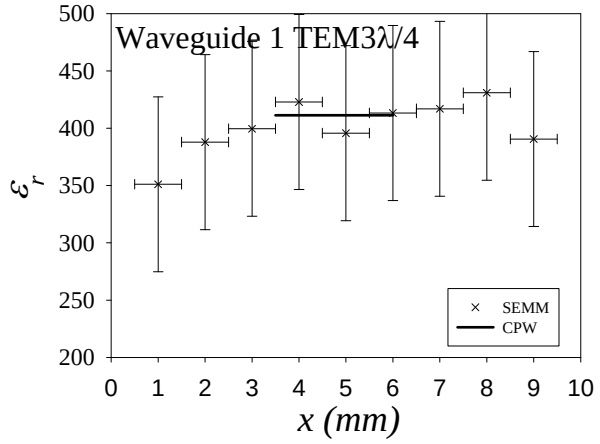

Fig. 6b Measured SEMM and CPW results for the TEM 3λ/4 mode in the vicinity of waveguide 3

CONCLUSION

|The limitations of the image charge model extended to thin films has been demonstrated. The sources of error have been documented and reasons for the error discussed. The raw data illustrates the potential of the SEMM to reveal variations in ε_r across a thin film. The values of relative permittivity extracted via the model show error bars of the order of 25%. A set of thin film standards, comprising of films of fixed thickness and different relative permittivity and different loss tangent would help to provide a much more accurate calibration.

ACKNOWLEDGEMENTS

We would like to thank K. Lees and A. Gregory at NPL for the split post resonator measurements and for discussions, D. Holdom for film patterning and C. Ansell and W. Hay for resonator construction. This work was supported by the UK Engineering and Physical Sciences Research Council.

REFERENCES

[1] C. Gao, B. Hu, I. Takeuchi, and K.-S. Chang, "Quantitative scanning evanecsent microwave microscopy and its applications in the characterization of functional materials libraries," *Meas. Sci. Technol.* vol. 16, pp. 248-260, December 2004.

[2] T. Wei, X.-D Xiang, "Scanning tip microwave near-field microscope," *Appl. Phys. Lett.* vol 68, pp.3506-3508, June 1996.

[3] K. S. Chang, M. Aronova, O. Famodu, and I. Takeuchi, "Multimode quantitative scanning microwave microscopy of in situ grown epitaxial $Ba_{1-x}Sr_xTiO_3$ compostion spreads," *Appl. Phys. Lett.* vol 79, pp.4411-4413, December 2001.

[4] P. M. Suherman, T. J. Jackson, and M. J. Lancaster, "Comparison of techniques for microwave characterization of BST thin films," *IEEE. Trans. microw. Theory tech,.* vol 55, pp. 397, Febuary 2007.

[5] S. S. Gevorgian, "Basic characteristics of two layered substrate coplanar waveguides," *Electron. Lett.* vol 30, pp. 1236, July 1994.

[6] S. Hyun, J. H. Lee, S. S. Kim, and K. Char, "Anisotropic tunning behavior in epitaxial $Ba_{0.5}Sr_{0.5}TiO_3$ thin films," *Appl. Phys. Lett.* vol 77, pp.3084-3086, November 2000.

[7] R. A. Kleismit, M. K. Kazimierczuk, and G. Kozlowski, "Sensitivity and resolution of

evanescent microwave microscope," *IEEE. Trans. microw. Theory tech*, vol 54, pp. 639, February 2006.

[8] C. Gao, and X.-D. Xiang, "Quantitative microwave near-field microscopy of dielectric properties," *Rev. Sci. Instrum.*, vol. 69, pp. 3846-3851, November 1998.

[9] J. H. Lee, S. Hyun, and K. Char, "Quantitative analysis of scanning microwave microscopy on dielectric thin film by finite element calculation, *Rev. Sci. Instrum.*, vol. 72, pp. 1425-1434, February 2001.

[10] D. E. Steinhauer, C. P. Vlahacos, F. C. Wellstood, and S. M. Anlage, "Quantitative imaging of dielelctric permittivity and tunability with a near filed scanning microwave microscope," *Rev. Sci. Instrum.*, vol. 71, pp. 2751-2758, April (2000).

[11] Y. C. Chen, Y.-S. Hsieh, H.-F. Cheng, and I.-N. Lin, "Study of microwave dielectric properties of perovskite thin films by near-field microscopy," *J. Electro. Ceram.* , vol. 13, pp. 261-265, February 2004.

[12] H. F. Cheng, Y.-C. Chen, and I.-N. Lin, "Evanescent microwave probe study on dielectric properties of materials," *J. Eur. Ceram. Soc.*, vol. 26, pp. 1801-1805, October 2006.

[13] A. Imtiaz, T. Baldwin, H. T. Nembach, T. M. Wallis, and P. Kabos, "Near-field microwave microscope measurements to characteize bulk material properties," *Appl. Phys Lett.*, vol. 90, p. 243105, June 2007.

[14] D. P. Kimber, R. C. Pullar, and N. McN. Alford, "The effects of dielectric loss and tip resistance on resonaotr Q of the scanning evanescent microwave microscopy (SEMM) probe, *Meas. Sci. Technol.*, vol. 19, p. 115502, September 2008.

[15] T. Nishikawa, K. Wakino, H. Tanaka, and Y. Ishikawa, "Precise measurment method for complex permitiviity of microwave substrate," *CPEM '88 Digest.*, pp. 155-156. June 1988.

[16] Q. Zhang and P. J. McGinn, "Imaging of oxide dielectrics by near-field microwave microscopy," *J. Eur. Ceram. Soc.*, vol. 25, pp. 407-416, February 2004.

[17] P. M. Suherman, T. J. Jackson, Y. Y. Tse, I. P. Jones, R. I. Chakalova, and M. J. Lancaster, "Microwave properties of $Ba_{0.5}Sr_{0.5}TiO_3$ thin film coplanar phase shifters," *J. Appl. Phys.*, vol. 99, p. 104101, May 2006.